UNIVERSITY OF NOVA GORICA
GRADUATE SCHOOL

AB-INITIO CALCULATIONS ON THE MODULATION OF ELECTRONIC BAND GAP OF PHOTOCATALYTIC SEMICONDUCTORS

DISSERTATION

M. Sc. Praveen Chandramathy Surendran

Mentor: Prof. Dr. Matjaž Valant

Nova Gorica, 2012

UNIVERZA V NOVI GORICI
FAKULTETA ZA PODIPLOMSKI ŠTUDIJ

AB-INITIO IZRAČUNI MODULACIJE ELEKTRONSKIH PASOV FOTOKATALITIČNIH POLPREVODNIKOV

DISERTACIJA

M. Sc. Praveen Chandramathy Surendran

Mentor: Prof. Dr. Matjaž Valant

Nova Gorica, 2012

ACKNOWLEDGEMENTS

The research presented in this thesis was carried out in partial fulfillment of my Ph. D. studies at the Materials Research Laboratory, University of Nova Gorica, Slovenia, supervised by Dr. Matjaž Valant.

Foremost, I owe my deepest gratitude to my supervisor, *Matjaž Valant*, who has been a faithful source of encouragement, wisdom and support throughout my research work. His aid and supervision have always led me back on track whenever I have been lost or confused. His inexhaustible enthusiasm has been a true source of inspiration for me; not only in work but also for life in general. I also thank him for giving a lot of freedom in my research work. You have been an excellent supervisor; thank you!

It is an honor for me to thank *Dr. M. T. Sebastian*, for his invaluable effort in sending me to Slovenia for doing my Ph. D.

I am grateful to my first quantum mechanics professor *Dr. Sam Solomon*; without him I would never understand quantum mechanics. I also take this opportunity to thank *Dr. Sam* for introducing me to *Dr. Sebastian.*

I am indebted to *Dr. Anton Kokalj*, for his great help in doing some calculations and for some fruitful discussions. I am sure *Anton's* confident appearance and passion towards science has inspired me a lot to be prepared for whatever next step that I take in my life. Thank you so much!

I am grateful to *Dr. Vicente Timon* for helping me to obtain some computational power. I also thank him for his valuable advices throughout my work. I had fantastic time with him and his family throughout my 13 weeks of stay in Spain; thank you all!!

I would like to show my gratitude to *Prof. Dr. Gvido Bratina* for his help and for being a part of my committee. To assist his teaching in course on solid state physics was a great educational experience for me. I also would like to thank him for a fair share of discussion on interesting topics.

It is a pleasure for me to thank *Prof. Dr. Michel Rerat* for his invaluable help throughout my work. I was always enthusiastic whenever we had a Skype conversation. He has helped me a lot in understanding many hard core computational topics. I also thank him for accepting our invitation to be the external committee member for my thesis.

I would like to thank *Prof. Dr. Zdravko Kutnjak* for being a member of my committee and also for his lectures on solid state physics.

A special “thank you” goes to *Dr. Michael Pitcher* and *Dr. Layla Martin-Samos Colomer* for their invaluable help in improving the quality of the thesis. I also thank the rest of the members of our group, *Iulia, Metka, Mojca, Saim, Daniel, Miro, Mattia* and *Sandra*. I would like to specially thank my office mate *Mirela*. Thanks for the time that we have spent in discussing so many things and indeed for your care when I was having some severe migraine.

I specially would like to thank the colleagues *Egon*, *Polona*, *Primož* and *Andraž* for their help. I specially would like to thank all our secretaries in the department. All of them have been very helpful in arranging the things on time. A special “thank you” go to *Tea*, she has been very helpful in making my arrival and stay in Slovenia possible. I am also grateful *Prof. Dr. Samo Stanič* and *Prof. Dr. Božidar Šarler* for their excellent advices throughout my coursework.

I am grateful to my previous colleagues, *Urša*, *Santosh* and *Padma*. They were supporting me in all the ups and downs in my life in Slovenia.

I also would like to thank *Prof. Dr. Andrej Filipčič* for providing me access to SIGNET cluster and HPC-EUROPA2 for providing me supercomputing facilities. It is a great pleasure for me to express my sincere gratitude to the Slovenian research agency for funding.

Now it is a pleasure for me to thank few of my friends. First, I would like to express my gratitude and love towards my friend *Peter* and his wife *Jasmina*. Thank you so much for considering me as a family member. Now very special thanks go to my flat mate *Vesna* and my dearest friend *Sebastijan*. We had wonderful times, whenever we were cooking together and travelling.

The last but not the least, my heartiest gratitude goes to my family especially my mother and my father. I would never be reaching at this point without their prayers and support. I also take this opportunity to thank my sister, brother-in-law and all other family members. They were all supporting me for my studies not only for my Ph. D. but also for all my studies till to date.

With all the proud of being the first Ph. D. student at the Materials Research Laboratory, once again, thanks to all who have helped making this thesis a reality!

Thank you Slovenia!!

ABSTRACT

The research described in this dissertation summarizes a series of density functional calculations on the modulation of the electronic band gap of photocatalytic semiconductors.

First we have considered hematite and studied the modulation of its structural and electronic properties by creating a solid solution with Cr_2O_3 and Al_2O_3. Our calculations indicate that several electronic properties of hematite have been modified by incorporating Cr and Al cations into the Fe sublattice. Modifications include a general trend of decrease in the band gap value with an increase in Cr content. In addition, an alternation of the nature of valence band as well as an increase in the valence band width is also observed with the increase in the percentage of Cr_2O_3. These factors are expected to speed up the charge transfer kinetics of holes as well as an improvement in harvesting the photons in the visible region of the solar spectrum. The presence of Al_2O_3 reduces the volume of the unit cell, thereby increasing the hopping probability and thus facilitating the majority carrier conduction. Although the Fe-Cr-Al mixed oxide seems to be very promising for photocatalytic applications, Fe_2O_3 content should not be below 50%, as it might result in increased recombination.

In addition, to improve the photocatalytic activity of an existing semiconductor, we have applied an external static electric field as a parameter to tune the electronic band gap. We formulated the model by applying a static electric field to prototype alkali halide crystals. Later we have extended the same model to study the effect of external electric field on AgCl and AgBr crystals as they represent typical UV-active semiconductors. From the study we have observed that, a red shift in the light absorption and band widening are the principal effect of the electric field. Both of these effects are very useful in promoting photocatalytic activity of wide band gap semiconductors (most of the oxide semiconductors). We also carried out a computational calculation of the dielectric strength of wideband gap materials using a general method proposed by Callen.

Finally, we modeled a novel Bi-based perovskite, $BiVO_3$, the ferromagnetic *Pnma* structure of which is found to be far more stable than the cubic structure. Full characterization of the structural, electronic, and magnetic properties of *Pnma*-$BiVO_3$ is presented. A direct band gap of 1.96 eV is calculated and this falls, in the visible region of the solar spectrum. Both the valence and conductions bands are well dispersed; hence high carrier mobility is expected. Dynamical stability of the material is confirmed by calculating the phonons at the Γ point, and the IR and Raman modes are presented. Overall, results show that $BiVO_3$ could be a very promising candidate for photocatalytic applications.

POVZETEK

Raziskovalno delo, predstavljeno v tej doktorski disertaciji, je skupek rezultatov računskih simulacij na osnovi teorije gostotnega funkcionala o modulaciji energijske špranje fotokatalitskih polprevodnikov.

Najprej smo proučevali lastnosti hematita, pri čemer smo glavni poudarek namenili modulaciji strukturnih in elektronskih lastnosti hematita pri tvorbi trdnih raztopin z vključevanjem Cr_2O_3 in Al_2O_3. Rezultati simulacij pokažejo, da se z vključevanjem Cr in Al kationov v kristalno podmrežo Fe spremenijo nekatere elektronske lastnosti hematita. Opazili smo, da se širina energijske špranje zmanjšuje s povečevanjem deleža Cr, obenem pa se spremeni vrstni red in narava energijskih stanj v valenčnem pasu ter poveča širina samega valenčnega pasa. Ti prispevki naj bi pospešili kinetiko prenosa naboja v vrzelih in izboljšali izkoristek absorpcije fotonov v vidnem delu spektra sončne svetlobe. Po drugi strani povečanje vsebnosti Al_2O_3 zmanjšuje volumen osnovne celice, s čimer se olajša prenos večinskih nosilcev naboja zaradi povečanja verjetnosti preskakovanja med stanji. Čeprav so mešani Fe-Cr-Al oksidi zelo obetavni za različne fotokatalitske aplikacije, vsebnost Fe_2O_3 naj ne bi bila manjša od 50 %, saj bi manjše vsebnosti pospešile rekombinacijo nosilcev naboja.

V nadaljevanju smo z namenom, da bi izboljšali fotokatalitsko učinkovitost polprevodnika, proučevali vpliv zunanjega električnega polja kot parametra pri prilagajanju širine energijske špranje. V ta namen smo kot modelni sistem uporabili kristalne strukture alkalijskih halidov, pod vplivom zunanjega električnega polja. Sistem smo dodatno razširili s proučevanjem vpliva zunanjega električnega polja na elektronske lastnosti AgCl in AgBr, ki predstavljata tipična polprevodnika, aktivna v UV delu svetlobnega spektra. Glavni vpliv zunanjega električnega polja je premik adsorpcije proti rdeči svetlobi in razširitev energijske špranje. Oba učinka ugodno vplivata na povečanje fotokatalitske aktivnosti polprevodnikov s široko energijsko špranjo, kamor se uvršča večina oksidnih polprevodnikov. Izpeljali smo tudi računsko simulacijo dielektrične trdnosti polprevodnika s široko energijsko špranjo na osnovi splošne Callenove metode.

V zadnjem delu disertacije smo modelirali novo perovskitno spojino $BiVO_3$. Ugotovili smo, da je *Pnma* struktura bistveno stabilnejša kot kubična struktura, zato je predstavljena celovita karakterizacija strukturnih, elektronskih in magnetnih lastnosti *Pnma*-$BiVO_3$. Izračunali smo, da je $BiVO_3$ polprevodnik z neposredno energijsko špranjo širine 1.96 eV, kar pomeni, da material adsorbira svetlobo v vidnem delu spektra. Tako valenčni kot prevodni pasovi so dobro razpršeni, zaradi česar so prenašalci naboja zelo mobilni. Dinamično stabilnost materiala smo potrdili z izračunom fononskih vibracij v gamma-točki, predstavljene so IR in Ramanske vibracijske vrednosti. Rezultati kažejo, da je $BiVO_3$ obetaven material za uporabo v fotokatalitskih aplikacijah.

Keywords:

DFT; photocatalysis; band structure; hematite; rock-salt; perovskite

TABLE OF CONTENTS

List of Figures

List of Tables

1 INTRODUCTION

Fossil fuels in the form of coal, oil, and natural gas have powered human society for few centuries now. Continuing to power the world from such nonrenewable sources threatens our energy supply and puts enormous strain on the environment. Additionally, the forecasted future energy demands are not so encouraging, due to the population growth rate and increasing energy consumption; a new renewable energy system must be developed. An efficient utilization of solar energy would solve all our energy needs. The energy from sunlight, which strikes the Earth in one hour, is more than the total energy consumed by human beings in one year (14 TW) [1, 2]. However, efficient and full utilization of solar energy to meet the global energy demands needs to achieve certain goals. First of all, due to the increasing attention towards carbon free energy production, the means for solar energy conversion, storage, and distribution should be environmental friendly. The next, rather important, goal is to provide a constant and stable energy flux. Several devices are already developed that can capture and convert electromagnetic energy. The most popular is the photovoltaic cell [3], which produces electricity upon solar irradiation. It has attracted a lot of attention as a potentially wide spread approach for capturing a sustainable energy source. In order to compete with the fossil based energy supply, and to provide a truly widespread primary energy source, solar energy has to be captured, and handled in a cost effective way. The variability of solar light with atmospheric and seasonal changes and the lack of light during the night hours is a challenge to the intensive use of solar to energy conversion devices. Hence, energy harvested from sun needs to be efficiently converted into a chemical energy, which can be stored, transported and used upon demand. A highly desirable approach is to convert the electromagnetic energy in the form of chemical bonds through a process which mimics natural photosynthesis, where plants store solar energy in the form of carbohydrates by effectively rearranging the electrons in CO_2 and H_2O. By this mechanism solar energy can be converted and stored in the form of the simplest chemical bond, H_2, by splitting water through a process called *photocatalysis*[1]. By analyzing the thermodynamics (losses) of solar energy to chemical conversion, Bolton *et al.* [4, 5] concluded that it is possible to store about ~16% and ~10% of solar energy in the form of H_2 for double and single photosystem schemes, respectively, at 1 Sun irradiance (1 Sun=1000 Wm^{-2}).

Applications of photocatalysis are generally classified into two categories:

i. in improving the environment in which we live such as anti-stain, self-cleaning, remediation of hazardous waste, treatment of contaminated water, control of toxic air, etc.
ii. conversion of light energy into chemical bonds via photocatalytic water splitting.

Owing to the high energy capacity and environmental friendliness, hydrogen is expected to become the main energy carrier of the future. In addition, hydrogen is a basic raw material in many chemical industries. On a large scale, hydrogen is mainly produced from steam reforming using hydrocarbons such as methane. To have an environmentally benign and cost effective production of the gas, hydrogen has to be produced from renewable energy sources such as solar energy. Photocatalytic water splitting as a part of the hydrogen economy is a promising technology whose only waste product upon burning is water! If successfully developed, this could be a new artificial means of photosynthesis [6] that would provide a clean fuel; *the hydrogen*-“fuel of the future” [7].

In 1972, Fujishima and Honda [8] demonstrated the evolution of H_2 gas at the platinum-counter electrode when a TiO_2 electrode in an aqueous solution is exposed to strong light. What happened on the surface of TiO_2 was the decomposition of water through photoelectrolysis and the evolution of H_2 at the Pt electrode, called thereafter as *Honda-Fujishima Effect* (HFE) [9, 10]. Later it was shown that the particulate TiO_2 with a small amount of platinum deposition on the surface behaves like a short circuit photoelectrochemical cell and can be used to split water [7]. Ever since this pioneering discovery of Fujishima and Honda

---

[1] If a semiconductor immersed into water (in general a solvent), when illuminated with photons exceeding its band gap energy, is able to catalyze a reaction at it surface, then is called a *photocatalyst.*

countless efforts have been made in developing cost-effective photocatalytic water splitting systems for storing solar energy in the form of hydrogen.

1.1 Photocatalytic water splitting

1.1.1 General principles

Over the past 40 years, artificial routes to photosynthesis, including photoelectrochemical and photocatalytic solar energy conversion, have been studied intensively. A most appealing and elegant pathway for the artificial photosynthesis is to split water using solar energy, i.e., solar water splitting. This would provide a route to human's dreams on a hydrogen fuel based future. In solar water splitting, the oxidation process produces oxygen, while the reduction end takes different forms; the most elemental, perhaps, the most demanding form is the evolution of hydrogen.

$$\mathrm{H_2O} \rightarrow \frac{1}{2}\mathrm{O_2(g)} + \mathrm{H_2(g)};\ \Delta G = +237\ \mathrm{kJ/mol} \qquad 1.1$$

Since the water splitting reaction represented by Eq. (1.1) involves a large positive Gibbs energy change of 273 kJ/mol, (according to Nernst equation this corresponds to 1.23 eV) energy must be supplied to initiate the reaction [4]. In principle, photons in the visible region of the solar energy spectra could be used to assist Eq. (1.1). Since water is transparent, the absorption in visible range is poor. Hence, a semiconductor with band gap energy equal to or greater than 1.23 eV must be used to harvest photons from the visible region of the solar spectra. To accomplish this artificial photosynthesis in an economically viable way, a water splitting cell, composed of stable semiconductors, engineered to split water directly at the semiconductor surface, has to be developed. Two extensively investigated methods exist for this purpose, a particulate photocatalytic (PC) [11] and a photoelectrochemical (PEC) water splitting cell [12]. PC water splitting systems use a photoactive semiconductor, dispersed in pure water, for the homogenous and simultaneous production of H_2 and O_2. A series of inorganic colloidal materials and molecular complexes are already developed for this method [13, 14]. In contrast, the PEC water splitting systems use a photoactive semiconductor as an electrode.

Recently, numerous PEC systems have been developed [1], yet their complexity still remains as disadvantageous [11]. Although the structure of the PC and PEC water splitting systems is different the basic requirements for the materials are essentially same.

The solar water splitting process is initiated when the semiconductor absorbs energy greater than or equal to the band gap energy. This absorption excites an electron from the valence band of the semiconductor to the conduction band and creates an electron-hole pair (exciton) as shown in Fig. 1-1. The photoelectrons and holes reduce and oxidize water to produce a mixture of H_2 and O_2 in stoichiometric ratio of 2:1 [1, 4, 8, 15]. The hydrogen evolution reaction (HER) and the oxygen evolution reaction (OER), associated with Eq. (1.1), are as follows [1, 10]:

$$\begin{aligned} &H_2O+2h^+ \rightarrow \frac{1}{2}O_2+2H^+ \ \text{(HER)} \\ &2H^++2e^- \rightarrow H_2 \qquad \text{(OER)} \\ &H_2O \rightarrow H_2+O_2 \quad \text{(Overall Reaction)} \end{aligned} \tag{1.2}$$

The overall reaction represented in Eqs. (1.2) is a four electron transfer reaction (O_2 evolution).

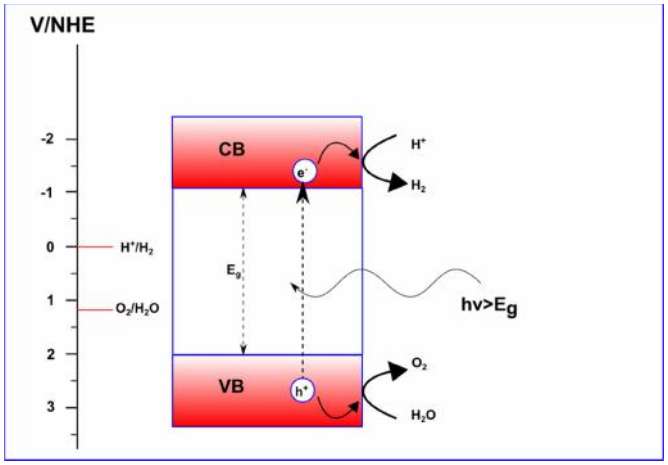

Figure 1-1: Schematic representation of the photocatalytic water splitting reaction. Oxidation and reduction potential of the reaction is indicated on an energy scale with respect to the normal hydrogen electrode at pH 0.

As a thermodynamic requirement, not only the band gap value but also the relative positions of the valence and conduction band edges are also important [1, 7]. The conduction band minima (E_{cb}) of the semiconductor must be located at a potential more negative than the proton reduction potential $(H^+/H_2=0\text{ V})$ *vs.* the normal hydrogen electrode (NHE) at pH 0 (-0.41 V, at pH 7) and the valence band maximum (E_{vb}) must exceed the oxidation potential of water (OH^-/O_2) i.e., 1.23 V *vs.* NHE at pH 0 (0.82 V, at pH 7). Hence according to these values, a semiconductor with band gap energy greater than 1.23 eV and having E_{cb} and E_{vb} straddled by the conduction and valence band edges would, in principle, initiate the HER and OER mechanisms using the exciton pair generated under illumination. However, in order to pursue either or both of the reactions the photogenerated exciton pairs must travel towards the semiconductor liquid junction and must react only with the reaction species at the surface of the semiconductor.

In principle, the charge transfer at the semiconductor–liquid interface suffer losses [16] due to the difference in the concentration, the over potentials needed to drive the HER and OER, unabsorbed low energy photons, heat loss associated with the excess energy of the high energy photons, and the entropy losses associated with the chemical bond formation. Therefore, for the sake of these inevitable fundamental photophysical problems, the energy required for the photoelectrolysis at a semiconductor is often reported as 1.6-2.2 eV [1, 17-20]. The properties and the physics involved at the semiconductor-liquid interface are summarized below [1, 16, 21].

1.1.2 Physics of semiconductor-liquid contacts

Consider a semiconductor, immersed into a solution containing a donor (A^-) and an acceptor (A), alternatively a redox couple, having electrochemical potential $-qE^0(A/A^-)$, where E^0 is the Nernst potential of the redox pair (A/A^-). In order for the two phases to be in equilibrium, their electrochemical potential must be same. The redox potential of the semiconductor is determined by its Fermi level. As shown in Fig. 1-2a, if the redox potential of the solution and the Fermi level do not lie at the same energy, an effective charge transfer between the two species is necessary to equilibrate the two phases. The excess charge, now located at the semiconductor, will extend into the electrode for a significant distance (10^2-10^4Å), called the space charge region and is associated with an electric field.

For a photoelectrochemical water splitting reaction, the redox couple of interests are H^+/H_2 couple for a p-type photoanode and O_2/H_2O couple for an n-type photocathode. We shall consider a typical n-type semiconductor electrode in equilibrium with redox species in solution (e.g., O_2/H_2O). For an n-type semiconductor electrode, the Fermi level is higher than the electrochemical potential of the solution and hence majority carriers (electrons) will be transferred from the semiconductor to the solution. This will results in accumulation of ionized dopant atoms in the material, as a consequence, the semiconductor will have an excess positive charge and the solution will have an excess negative charge. The excess positive charge will be accumulated in the space charge region in the semiconductor species, close to the solution, called the depletion region (whose width is represented by *w*). This will result in an upward bending of the bands as shown in Fig. 1-2b.

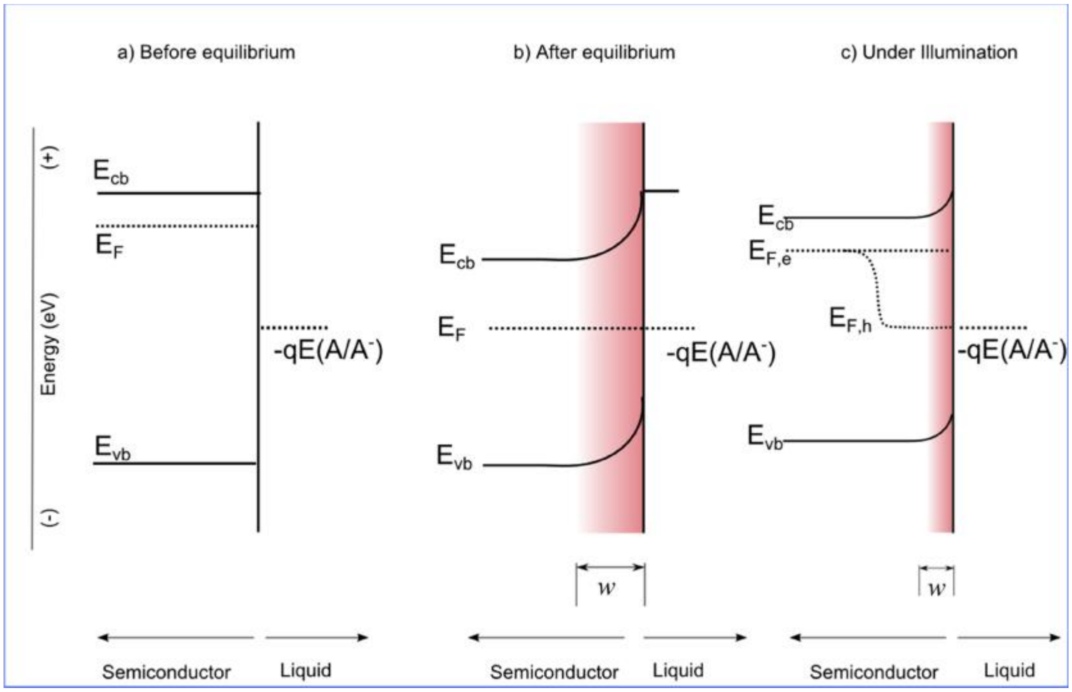

Figure 1-2: Properties of a semiconductor liquid interface a) before equilibrium b) after equilibrium and c) under illumination is shown schematically. See text for the notation.

The initial difference in the chemical potential of the two species will be balanced by an interfacial electric field generated as an after effect of the charge flow. The strength of the electric field, and hence the potential energy barrier (Schottky barrier) inside the semiconductor depends on the initial difference between the chemical potentials of the two species. Since this initial difference is in the order of 1 eV and the width of the depletion region is in the order of hundreds of nanometers, the electric field inside the crystal can be as large as 10^5 Vcm^{-1}. At the same time, in the solution the negative charges will form a narrow layer (the Helmholtz layer), close to the semiconductor electrode. Alternatively, for a p-type semiconductor, the charge transfer results in accumulation of the negative charges in the space charge region and will eventually result in downward bending of the bands.

The Fermi levels, as well as the band edge positions are shifted by the application of an external potential. At a certain potential, the Fermi energy lies at the same energy as the chemical potential of the solution and hence there will be no band bending. This potential is called flat band potential, E_{fb}. Since the depletion region contains only minority charge carriers, the electron transfer reaction occurs slowly, if at all. When the depletion region is illuminated with a light of sufficient energy to excite electrons from valence band to conduction band, large number of charge carriers (electron-hole pairs) will be produced. In crystalline inorganic semiconductors, these electron-hole pairs will be separated effectively, in the presence of the high electric field at the depletion region, due to the high mobility of the charge carriers. Semiconductors are therefore astonishingly effective in the key process of photocatalysis, such as harvesting light energy and charge separation. Particularly because of the downward band bending, n-type semiconductors show rectifying properties as a photoanode. This can be explained as due to the Schottky barrier. The n-type semiconductor inhibits the electron flow from the solution to the electrode both under dark and irradiation conditions producing zero anodic current. While, under irradiation and anodic potentials, the positive holes (h^+) can oxidize the redox species in the electrolyte and the electrons contributes to the anodic current.

The theoretical efficiency of such a system is generally determined by the energy that can be extracted from the electron-hole pair [5]. For instance, the maximum free energy available for the photogenerated electron is often governed by the difference between the E_{cb} and $E(A/A^-)$. This energy difference has to be as high as possible to optimize the performance of the system. In principle, this can be achieved by varying the electrochemical potential of the solution. However, the actual free energy obtained from the system considerably differs from the theoretical one due to the non-equilibrium induced by the photo illumination. The actual energy depends on the stationary state kinetics of the charge carriers as a result of the illumination. Under non equilibrium conditions such as irradiation, the electrochemical potentials of the charge carriers are represented by so called quasi-Fermi levels [22] (see Figure 1-2c) and their population is described by the Fermi-Dirac statistics. The free energy generated by the semiconductor is then given by the difference between the quasi-Fermi levels of the electrons ($E_{F,e}$) and holes ($E_{F,h}$) respectively.

1.1.3 Photoelectrochemical water splitting

PEC water splitting on a single crystal photoanode is illustrated in Fig. 1-3. As shown in Fig. 1-3 an n-type semiconductor and a counter electrode are immersed in water.

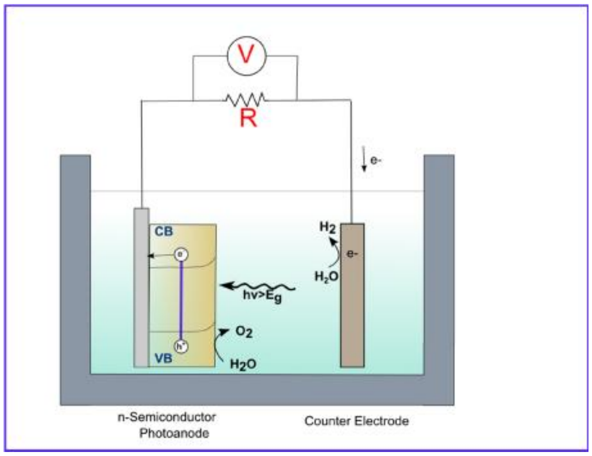

Figure 1-3: Schematic of a photoelectrochemical water splitting cell. Semiconductor photoanode as well as the counter electrode are indicated.

The electrodes are connected together via an external bias. When light of sufficient energy strikes on the photoanode surface, electron-hole pairs are generated. The photogenerated electrons migrate through the bulk and reach the counter electrode via the external circuit. At the counter electrode, the electrons reduce the protons to give H_2. At the same time the holes left behind at the photoanode; oxidize the water at the surface to evolve O_2.

1.1.4 Photocatalysis on a semiconductor particle

The photocatalytic water splitting reaction on the surface of a semiconductor particle is essentially the same as in the case of photoelectrochemical system. The water splitting reaction proceeds on the surface of the semiconductor particulate system in three steps [11, 23-25]. In the first step, the photocatalyst absorbs energy greater than its band gap. As a result one electron-hole pair per absorbed photon is generated in the bulk of the semiconductor. In the second step, the photoexcited charge carriers migrate to the surface of the semiconductor, where the redox species are located, without recombination. In the final step, the photogenerated electrons and holes reduce and oxidize, respectively, the adsorbed water species on the surface of the semiconductor to produce H_2 and O_2. All the steps of the photocatalysis on the surface of a particulate photocatalytic system are illustrated in Fig. 1-4.

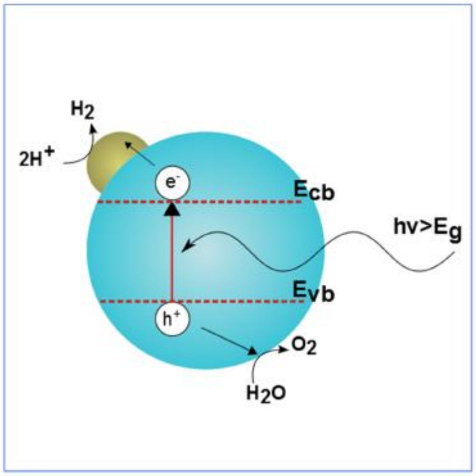

Figure 1-4: Schematic of a particulate photocatalytic system. Blue large sphere represent the semiconductor particle and the small golden sphere represent a cocatalyst loaded onto the surface of the semiconductor.

The first two steps in the process depend on the structural and electronic properties of the semiconductor. The first step, i.e., the photon absorption step is strongly connected to the band structure of the material and is directly linked, in particular, to the nature of the valence and conduction bands as well as the energy gap between them. The semiconductor absorbs light with energy greater than or equal to the band gap. For visible light photocatalysis, this corresponds to a wavelength, λ, $400 < \lambda < 800$ nm. With regard to the structural properties, the crystallinity of a given crystal has a key role in controlling the recombination rate. High crystallinity indicates low defect concentration (recombination centers) so, by increasing the crystallinity, the recombination can be inhibited to a certain level. Another important factor is that, by reducing the crystal size the diffusion length of the photogenerated electron-hole pair can be shortened. The third step in photocatalysis, i.e., the evolution of H_2 and O_2 is triggered by the presence of a solid cocatalyst, loaded onto the surface of the semiconductor as a dispersion nanoparticle (<50 nm). The idea behind loading a cocatalyst is to produce active sites and thus to reduce the activation energy for the evolution of H_2 and O_2. A noble metal (e.g., Pt, Rh) or a transition metal oxide (e.g., NiO, RuO_2) is generally used as a cocatalyst [11, 23, 26, 27]. Since most photocatalysts are unable to initiate the hydrogen evolution at the surface, in most cases this is achieved by loading a cocatalyst. The photocatalytic activity of a semiconductor is often tested by conducting half reactions using sacrificial reagents; i.e., reducing (e.g., EDTA, alcohol, sulphites, sulphides) or oxidizing reagents (e.g., Ag^+, Fe^{3+}, persulphate) are used to facilitate either the water reduction or oxidation reactions [28].

1.1.5 Requirements for a good photocatalyst

The selection of a suitable semiconducting electrode for the development of an efficient photocatalytic water splitting cell is critical due to certain stringent requirements. In most cases these requirements seem to be mutually exclusive. There are five main criteria that one has to consider in developing a visible light sensitive, stable and environmentally friendly photocatalyst.

i. Good visible light absorption capability

The light harvesting capability of a semiconductor is controlled by the electronic band gap of the material. The minimum requirement for the band gap value is given by the positive Gibbs energy change of the water splitting reaction (1.23 eV) together with unavoidable thermodynamic losses of ca. 0.2-0.4 eV. In addition, overpotential of ca. 0.4-0.6 eV is necessary at different points of the reaction to ensure fast reaction kinetics. As a result the minimum band gap required for the water splitting reaction is nearly 1.9 eV and this corresponds to a wavelength of 600 nm. Conversely, the intensity of the sun light falls rapidly beyond 400 nm (see Fig. 1.5); this imposes an upper boundary limit of 3.1 eV to the required band gap. Hence for efficient visible light driven photocatalysis the band gap of the corresponding semiconductor should be in between 1.9 and 3.1 eV [2, 10].

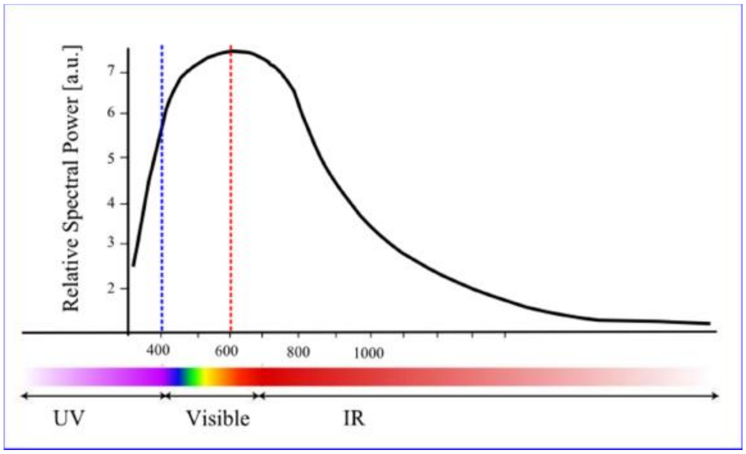

Figure 1-5: The intensity of the solar radiation spectra (in atomic units) with respect to the wavelength is plotted. Blue and red lines indicate the required upper and lower bound of the electronic band gap for the semiconductor for efficient water splitting.

ii. Suitable band edge positions

The second criteria require that the valence and conduction band edges of the semiconductor should straddle the water oxidation and proton reduction potentials. This demands that the conduction band edge should be more negative than the proton reduction potential and the valence band edge should be more positive than the water oxidation potential. Even though a large number of semiconductors have an adequate band gap for visible light harvesting, due to the stringent requirement for the band edge positions, a large number of them are actually inadequate for overall water splitting.

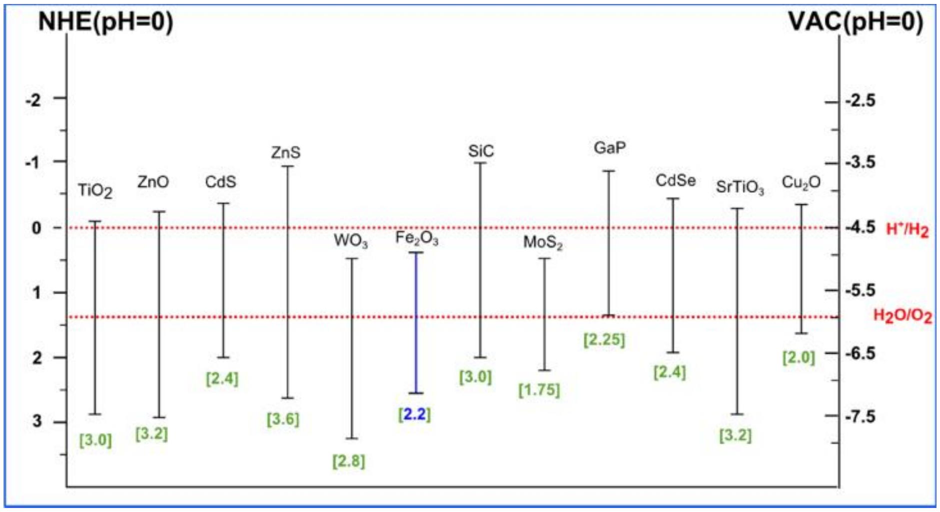

Figure 1-6: Valence and conduction band positions of common photocatalytic semiconductors with respect to the normal hydrogen electrode (NHE) as well as the vacuum level (VAC).

As shown in Fig. 1-6, only few semiconductors fulfill the requirement concerning the positions of the valence and conduction bad edges. The semiconductors with the ideal band edge positions do either have too wide band gap (c.f. Fig. 1-6) ($SrTiO_3$, SiC, ZnS) [29] or are unstable (Cu_2O, CdS) in aqueous solution [19, 21].

iii. Efficient charge separation and charge transport

For an efficient charge transport within the semiconductor and towards the semiconductor liquid interface the recombination of the photogenerated electron-hole pairs should be suppressed. The grain boundaries and shallow donor/ acceptor levels originating from the defects in the crystal often serves as recombination centers [22]. However, by increasing the crystallinity of the particles, the density of these recombination centers can be decreased [30]. An efficient charge transport necessarily requires either minority carrier diffusion length (L_D) longer than the particle size or high carrier life time [16], especially in the case of indirect band gap semiconductors. By decreasing the particle size, the possibility of the charge carriers in reaching the surface can be increased. In indirect band gap semiconductors the absorption coefficient is small because of the necessity of momentum transfer associated with the excitation of the electrons [1, 16]. Hence a large diffusion length is necessary for higher carrier intensity. In general, if the electron-hole generation occurs in the depletion region (w), the carriers will be separated due to the inbuilt electric field. In addition, if the charge carriers are produced within a distance equal to the diffusion length, the carriers will be able to reach the surface through diffusion before they recombine. Some semiconductors are known for their excellent effective charge transport properties, e.g., TiO_2 [31, 32] and WO_3 [33], whereas some others, like Fe_2O_3 [34], are notable exceptions due to their poor charge transport properties. In fact, the extremely small hole-diffusion length is one of the major reasons [22, 34] of the poor overall conversion efficiency of Fe_2O_3.

iv. High chemical stability

Resistance to photo and electrochemical corrosion and dissolution processes are severe requirements that limit the use of many photoactive materials for overall water splitting reaction. Most of the non-oxide semiconductors [22] either dissolve in water or form a thin oxide layer that precludes charge transfer across the semiconductor liquid interface. Generally, as the band gap value increases the stability against photo corrosion also increases. Oxide semiconductors are more stable but they are likely to undergo anodic or cathodic decomposition [13, 14, 22].

v. Low overpotentials for water reduction and oxidation

This requirement implies that the minority carrier transfer across the interface has to compete with the decomposition of the electrodes due to accumulation of charge carriers. For instance, in the case of an n-type semiconductor the hole-transfer across the semiconductor/liquid interface has to be fast enough to avoid the anodic decomposition due to the accumulation of charge carriers. The accumulation of charge carriers on the surface would cause a reduction of electric field at the interface and this will, in principle, result in the recombination of charge carriers. In such cases, in order to improve the charge transfer kinetics, catalytically active surface species [21, 22, 30] (Pt, Rh, Cr-Rh, RuO_2, etc., for hydrogen evolution and RuO_2, IrO_x, etc., for oxygen evolution) have to be loaded on the semiconductor surface.

1.2 Strategies to develop visible light sensitive photocatalysts

1.2.1 Challenges and new routes towards cost effective hydrogen production

Even though the essential properties, which a semiconductor should possess for the water splitting reaction, have been identified, to date no single material has been found to satisfy all these requirements. When solar hydrogen production is considered, the efficiency of the solar to hydrogen conversion (STH) system is evaluated as [27];

$$\text{STH efficiency (\%)} = \left(\frac{\text{Output energy as H}_2}{\text{Energy of incident solar light}}\right)\times 100. \qquad 1.3$$

To date, the maximum reported quantum efficiency for overall water splitting by the visible light driven photocatalysis (single step) is only about 5.9% [23]. So the value achieved is still far from the theoretically predicted (economically viable starting point for commercial purposes) value of 10% [35]. Hence, the development of a new photocatalyst material still remains as a crucial issue and is regarded as one of the most important challenging scientific issues in the 21st century. The metal oxide semiconductors are often a good starting point as photocatalysts since they have wide band gap and are stable against photocorrosion. In general the conduction band of a semiconductor is formed by the empty *d* orbitals of a transition metal or *s*/*p* orbitals of a typical metal. On the other hand the valence band is formed by the highly positive oxygen 2*p* orbitals (at ca. +3 V *vs*. NHE). Thus, as Scaife [15] noticed, it is difficult to develop a semiconductor having a conduction band edge suitable for the proton reduction and band gap in the visible region (<3eV). Hence most of the visible light active semiconductors have poor H_2 evolution properties due to an inappropriate conduction band edge, e.g., $BiVO_4$ [36] and WO_3 [33]. In fact, there are several non-oxide semiconductor materials that exhibit the appropriate band levels (see Fig. 1-6) in the visible region of the solar spectrum. But they are generally unstable and become deactivated through photocorrosion or self-oxidation. For instance, CdS has appropriate band positions for overall water splitting under visible light. In the presence of a sacrificial electron donor like Na_2SO_3, CdS has shown an excellent H_2 evolution capability. However, in the absence of a sacrificial electron donor, the S^{2-} anions in CdS are preferentially oxidized by the photogenerated holes, instead of H_2O molecules [37].

As an alternative strategy for utilizing wide band gap semiconductors, heterogeneous sensitizer molecules such as organic dyes and metal complexes are often used for achieving visible light harvesting. The H_2 evolution capabilities of such systems in the presence of sacrificial electron donors are widely studied. The adsorption of sensitizer molecules such as $Ru(bpy)_3^{2+}$ or Eosin Y on platinized TiO_2 has showed efficient H_2 production. Since the evolution of O_2 from H_2O is a four electron process, most of the sensitizer molecules themselves are incapable of oxidizing H_2O to O_2, additionally they undergo photo degradation in the absence of sacrificial electron donors.

Another major challenge is the size quantization effects when nanocrystalline semiconductor particles are used in the particulate photocatalytic systems. Nano-sized particles with the size from 1 to 10 nm show properties that lie in the transition between molecular and bulk phases. Unlike in bulk phases, the size of a nanoparticle can be same or smaller than the first excited state. In such case the electron or hole, excited upon illumination, has to assign a state of higher kinetic energy in order to fit into such a particle size. This spatial confinement of the particle within a potential well, just like the "*particle in a box*", causes them to behave quantum mechanically. This means that the energy bands split into discrete energy levels. The size quantization effects occur when the particle size falls below a critical radius and is often reported in the literature that this happens when the particle size is comparable to the de-Broglie wavelength of the charge carriers. Nano particles showing size quantized effects are called Q-particles or quantum dots. This size quantization has a serious impact on the electronic properties such as, the band gap increases with decrease in the particle size and the valence band levels slightly shifts toward the lower energies, while the conduction band levels strongly shifts towards the higher energies. Considering these effects of particle size in controlling the light absorption and carrier dynamics much efforts have been paid in controlling the particle size, crystallinity and morphology of particulate photocatalysts. Such controlled syntheses of nanoparticles of several oxide and non-oxide semiconductors have been reported e.g., TiO_2, Fe_2O_3, CdS, CdSe [38, 39]. Unfortunately, the light conversion efficiency of such nanoparticle systems never exceeds 2%.

A further advance in this nanochemical route to photocatalytic water splitting includes the use of nanotubes and nanowires and it has been demonstrated that nanotubes and nanowires enhance the charge separation and photocurrent. As examples, Shaban *et al*. [40], have reported that TiO_2 nanowires are almost twice as efficient as its spherical nanoparticle counterparts and Mahajan *et al.* [41], have shown that nanotube arrays are highly stable and can yield H_2 without any noticeable decrease in rate for at least a month. The doping of nanotubes has also become a common practice to capture a part of the visible spectrum. Such modified (doped) tubular arrays have been shown to produce photocurrents eight times higher than the unmodified arrays and twenty times greater than nanoparticle particulate systems. Recently, Wan *et al.* [42], have reported a red shift of 0.4 eV for Cd doped ZnO. The most recent development in nano-based catalytic system is the decoration of nanorodes or wires with nanoparticles or thin layers. However, none of these single step photocatalytic systems have shown to increase the overall hydrogen production efficiency.

Inspired by natural photosynthesis, a two-step photo excitation mechanism, called the z-scheme (tandem cell) is also popular. In the z-scheme the H_2 evolution and O_2 evolution are divided into two separate steps and are combined by a shuttle redox couple (oxidant/reductant) in the solution. A separate hydrogen evolution catalyst and an oxygen evolution catalyst are used for initiating both the reactions. The photoexcited electrons in the H_2 evolution catalyst reduce the water to H_2 and the photoexcited holes oxidize the reductant into the oxidant. At the oxygen evolution catalyst, the photoexcited electrons reduce the oxidant back to reductant, while the photoexcited holes oxidize the water to O_2. The z-scheme system has the following advantages. First of all, it enables the use of a semiconductor that has either O_2 evolution or H_2 evolution capability. Another advantage of the z-scheme system is the ease of separating H_2 and O_2. This can be achieved simply by applying a separator, such as a porous glass, allowing the migration of only the shuttle redox species. The z-scheme system, however, does have some serious disadvantages like being incapable of the simultaneous production of H_2 and O_2 due to the difference in concentration needed at the electrodes, needing twice the amount photons than the conventional systems, and the termination of gas evolution during the reaction due to more favorable oxidation and reduction of the shuttle redox species. Although a record solar to hydrogen efficiency of 12 % has been reported using this approach, their high cost and stability still remains the major drawback. One step photosystems are still preferred, not only because the two step systems are complex and high in cost, but also the one step system is capable of the simultaneous evolution of H_2 and O_2.

1.3 State of the art

1.3.1 Band structure calculations

So far we have addressed the stringent requirements that a semiconductor should meet in order to work as a good photocatalyst. It is clear that precise design of the bulk and surface properties of the semiconductor is necessary in controlling the interrelated electronic, (micro) structural and surface properties. As discussed in section (1.1.5), the key requirements for a photo electrode are the efficient absorption of light and charge transport properties. However, it is not easy to characterize these parameters experimentally. It becomes impractical if one wants to screen an entire composition spectrum for optimal properties. A more efficient approach is to characterize the base material through electronic structure calculations and to predict the optimal composition by analyzing the trend. Nowadays, electronic structure calculations have become a routine task even for experimentally oriented groups. The required computational power and the software are readily available and so the number of literature reports on the electronic structures is increasing dramatically. A large number of open source as well as commercial software with different levels of theory are readily available for the scientific community to perform the high quality band structure calculations and to visualize the data for a wide range of materials.

In solid-state physics, the electronic band structure of a solid describes ranges of energy in which an electron is "forbidden" or "allowed". At infinite separation, atoms are independent and they have atomic energy levels. When they are brought together to form a molecular solid, the electrons responds to the influence of other nuclei and electrons, and the electrons will gradually change their energy levels as the atoms are brought closer. Each atomic level will split into multiple molecular levels to accommodate all the electrons, based on Pauli’s exclusion principle, which formerly were in similar single atomic levels. As a result, the single levels of the isolated atoms will broaden out into a large number of closely spaced levels having finite energy width, called energy bands. To gain more insight into the energy bands, a quantum mechanical treatment is necessary. By considering the periodic nature of the crystals, and the elements of group theory, Bloch theorem defines the form of the one electron wave functions in their respective Bravais lattices by considering the crystal momentum $(\hbar\mathbf{k})$. The Bloch theorem rewrites the eigenstate, ψ, of the one electron Hamiltonian for all lattice vectors **R**, in a Bravais lattice in the form of a plane wave multiplied by a function with the periodicity of the lattice:

$$\cdot\ {}_{n\mathbf{k}}(\mathbf{r}) = e^{i\mathbf{k}.\mathbf{r}} u_{n\mathbf{k}}(\mathbf{r}) \text{ with } u_{n\mathbf{k}}(\mathbf{r}+\mathbf{R}) = u_{n\mathbf{k}}(\mathbf{r}). \qquad 1.4$$

The new wave vector, **k** introduced by the Bloch function can always be confined to the first Brillouin zone. Due to the periodicity of reciprocal space, each of the energy levels for a given **k** varies continuously as **k** varies. By solving the eigenvalue problem, we arrive at a description of the energy levels of an electron in a periodic potential in terms of a family of continuous functions $E_n(\mathbf{k})$:

$$H_{\mathbf{k}}u_{\mathbf{k}}(\mathbf{r}) = E_n(\mathbf{k})u_{\mathbf{k}}(\mathbf{r}). \tag{1.5}$$

This $E\,vs.\mathbf{k}$, relation is called the dispersion or band structure of a solid and for each *n*, the set of electronic levels specified by $E_n(\mathbf{k})$ is called the energy band.

Electronic band structure calculations generally bring a crucial insight into the critical optoelectronic properties of a photo electrode material. First of all, by plotting the energy dispersion along the high symmetry direction of a bulk crystal, one can understand the nature of the optical transition in the material. If the highest point of the valence band and the lowest point of the conduction band lie at the same **k**-point in the *E*-**k** diagram, the optical transition is considered to be direct, since it does not require any change in the crystal momentum. While if the maximum of the valence band and the minimum of conduction band lies at the different **k** points, a change in the crystal momentum is necessary to accompany the optical transition; in that case the transition is said to be indirect. Thus, for the indirect transition to occur a lattice vibration is vital. Because of this, the absorption coefficient of an indirect band gap semiconductor is much smaller than that of the direct band gap semiconductor, in fact, the difference in absorption coefficients can be two orders of magnitude. The main advantage of a direct band gap semiconductor is that, for most of them, all the incident light is absorbed in the first few micrometers of thickness, whereas an indirect band gap semiconductor would need several hundred micrometers of thickness to absorb all the incident light. Metal oxides, however, often have horizontally running bands due to their strong ionic bonding, which sometimes brings ambiguity in the real description of the nature of the transition.

The second important information that can be extracted from the electronic band structure is the carrier mobility. A large band width in the valence and conduction bands is a direct indication of high carrier mobility for holes and electrons, respectively. For better transport of the charge carriers through the material, a wider band width is often required. Extensive mixing of the orbitals with the neighboring atoms is, however, necessary for spanning a wider band. The more the overlap (hybridization), the higher the band width will be and so increasing transport of the charge carriers across the material. This can be further explained in terms of the curvature of the individual bands, $\left(\frac{\partial^2 E}{\partial \mathbf{k}^2}\right)$, which is directly related to the effective mass and mobility of the charge carriers as:

$$m^* = \hbar^2 \Big/ \left(\frac{\partial^2 E}{\partial \mathbf{k}^2}\right) \text{and}\, \mu = \frac{q\tau}{m^*}. \qquad 1.6$$

Highly parabolic curves indicate a smaller effective mass (*m**) for the charge carriers and hence high mobility for the charge carriers. For an indirect band gap semiconductor, high mobility is required for the charge carriers since they have to travel a long distance to reach the surface before they recombine. The susceptibility to recombination is often expressed in terms of either the carrier lifetime, τ_{R}, or the minority carrier diffusion length, $L_{\mathrm{D}} (L_{\mathrm{D}} = \sqrt{D\tau_{\mathrm{R}}})$. Where diffusivity of the charge carriers, *D*, is related to the mobility μ through the Nernst equation:

$$D = \frac{kT«}{e}. \qquad 1.7$$

In the case of transition metal oxides, the outer lying *d* orbitals are substantially contracted and they show poor overlap between the neighboring atoms. This makes their band width narrow and dispersion less; as a result they exhibit weak carrier transport. From an electrostatic point of view, a well localized electron in a narrow band often causes a lattice distortion due to its interaction with the surrounding cations (or holes in the valence band with the neighboring anion). Such distortions accompany the electron (or hole) when it moves through the lattice, and is called a polaron. If this interaction is very strong, the polaron can be even trapped on a particular site. The electron can then move only by a thermally activated hopping mechanism and its mobility will be very low. To a certain extent this drawback can be addressed by an extensive mixing of orbitals (increased band width).

More information can be extracted from the band structure calculations by plotting the density of states (DOS). DOS is the number of electronic states per unit energy interval. A careful analysis on the DOS plots gives information on different key parameters like electronic band gaps, nature of the bonding, contributions of different orbitals to a given band, and the width of the bands. The electron transition probability is directly proportional to the DOS. A high DOS at the conduction band states indicates a strong transition probability upon irradiation. The band structure calculations continue to focus on developing new semiconductor photocatalysts and have contributed substantially to the present photocatalytic literature.

1.3.2 Band gap engineering

Since only a few stable semiconductors can absorb visible light and have the required band levels for water splitting, efficient band engineering is necessary to develop new semiconductors which would perform as a photoelectrode and a photocatalyst. Several approaches have been proposed for the modulation of the electronic band structure and the band gap. We shall divide these approaches into two categories,

(i) Modulation of the electronic band structure of existing semiconductors

Doping: The replacement of a cation or an anion in a wideband gap semiconductor is often employed as a technique to improve the visible light sensitivity of the UV active photocatalysts. TiO_2 and $SrTiO_3$ have been studied extensively as a host semiconductor for doping. Transition metals with partially filled *d* orbitals or anions such as C^{4-}, N^{3-}, or S^{2-} are often employed as a dopant for creating donor or acceptor levels (sub-bands) in the band gap of the host semiconductor. These sub-bands often serve as a center for absorption of visible light. The dopant often provides a discrete level rather than a band in the band gap; these discrete levels hinder the effective charge transport inside the semiconductor. In addition, it is very difficult to maintain the charge balance when a dopant is introduced into the semiconductor. This charge imbalance results in vacancies and they act as a recombination center for the photogenerated electron-hole pair. However, co-doping with another suitable atom can be used for partially addressing these issues. For instance, Kudo *et al.*, [27] has demonstrated that co-doping of rutile TiO_2 with Cr^{3+} and Sb^{5+} shows improved photocatalytic activity under visible light irradiation compared to only Cr^{3+} doped TiO_2. Among doped metal oxides, to date the highest H_2 evolution activity has been shown by Rh doped $SrTiO_3$ [43] with an apparent quantum yield of 5.6%. Despite TiO_2 and $SrTiO_3$, there are other reports on the evolution of H_2 from aqueous methanol under visible light irradiation using Cr or Fe doped $La_2Ti_2O_7$ and H_2 or O_2

evolution from Sr, Ba or La doped (co-doped with Ir) tantalates and niobates in the presence of sacrificial reagents.

The creation of impurity levels suppresses the effective migration of holes and the presence of recombination centers such as oxygen defects, so doping is often considered as non-advantageous. Anions such as N, S or C, when substituted in the oxygen sub lattice, also show visible-light photocatalytic activity due to alternation of the nature of the valence band from pure O 2*p* character to a mixing of the *p* states of both oxygen and the dopant. This eventually results in a shift in the valence band edge as well as a reduction of band gap value.

Modification of continuous valance bands: Another method is to form a continuous valence band using certain cations. Kudo *et al*. [27], demonstrated that the presence of certain cations such as Bi^{3+}, Ag^{+}, and Sn^{2+} is beneficial for harvesting visible light. Since then there are reports on several semiconductors capable of harvesting visible light based on these cations, e.g., $PbBi_2Nb_2O_9$, $SnNb_2O_6$, $AgNbO_3$, and $BiVO_4$ [27]. The efficient H_2/O_2 evolution of these materials is attributed to the hybridized states evolved from the valence *s* states of the constituent elements (e.g., Bi-6s, Pb-6s). Even though none of these materials has shown effective overall water splitting under visible light, they have been successfully used in systems with two step photoexcitation such as a tandem cell.

Formation of solid solutions: The third strategy to band gap engineering is to form semiconductor alloys (solid solutions). In this approach the visible light sensitivity of a semiconductor is improved by forming a solid solution between a wide band gap and a narrow band gap semiconductor with a similar lattice structure. This approach is very beneficial that one can tune the band gap and the position of the bands by varying the composition. Reports have been published with a comparatively high quantum yield of 7% (with monochromatic light of 440, 480 and 580 nm) for Ru-loaded $ZnS\text{-}CuIS_2\text{-}AgInS_2$ [43] solid solutions and a moderate activity for Pt-loaded $ZnS\text{-}CuIS_2\text{-}AgInS_2$ [43].

External perturbations: Another efficient approach in tuning the band structure of a semiconductor material is to apply an external perturbation such as static electric fields. Several density functional studies have been employed in the past few years on the effect of electric field on the electronic properties of low dimensional materials especially on different nano-structures and graphene. Surprisingly, there are no reports on the effect of electric field in the photocatalytic properties of a semiconductor. It is, however, reported that the external electric field is extremely important in hydrogen storage systems due to the additional dipole moments created as a result of the charge redistribution under the external electric field. For instance, Li-doped carbon nano-tubes, single and bilayer graphenes, and mesoporous nickel and magnesium oxides [44, 45] have shown effective hydrogen storage capabilities in the presence of electric field.

(ii) Developing new semiconductors with predefined properties.

Using this approach we are aiming to develop new materials with pre-defined band structure properties. Developing a single phase metal oxide semiconductor that will serve as good photocatalyst still remains as a challenge. In order to design a new material one has to consider both structural and electronic properties such as the band structure requirements. Recently, ABO_3 perovskite structures have been the focus of wide spread interest, due to their ability to incorporate a wide range of metallic ions with a significant number of different anions. The ideal perovskite structure has a cubic symmetry with ABO_3 stoichiometry. The A site cation is often an alkaline or alkaline-earth metal or a rare-earth metal, while the B site cation is usually a transition metal atom. The structure is composed of a three dimensional framework of corner shared BO_6 octahedra. The B site cation locates in the octahedral vacancy and the A site cation fills the 12- fold vacancies formed by the octahedral. The B-O-B bond angle is 180^0 which is beneficial for the effective separation of the charge carriers. However, most perovskite structures are distorted and do not have cubic symmetry. The common distortions in the perovskites are displacement of cations within the octahedral and tilting of the octahedral. The main factors contributing to such distortions are the radius size effects and the Jahn-Teller effects. The tilting of the octahedra generally happens when the A site cation is too small to fit into the 12-fold site within the BO_6 polyhedral framework. To accommodate such cations, the octahedra generally tilt about the pseudo cubic axes. The first order Jahn-Teller distortions (FJTD) occur for compounds containing odd number of *d* electrons (i.e. Mn^{3+}, Cr^{2+}, Fe^{4+}, Ni^{3+}, and

Cu^{2+}) in the e_g orbitals. As a result of FJTD a regular octahedron undergoes distortion along the tetrad axis resulting in the formation of two long or shorter bonds on opposite sides of the octahedron. Another kind of structural distortions occur when symmetry allowed distortion is permissible. This symmetry allowed distortions allow mixing of orbitals (orbital mixing due to lone pair effect in Bi^{3+} and Pb^{2+}). This is called a second order Jahn-Teller effect. Weak covalent bonding also results in certain distortions such as displacement of the B site cation from the center of the octahedra leading to ferroelectricity.

Alkali tantalates $ATaO_3$ (A = Li, Na, and K – active under UV light), are one of the most widely studied ABO_3 perovskites [46]. Bismuth based ABO_3 perovskites also gained much attention not only due to their photocatalytic applications but also due to their advanced functional properties such as multiferroicity, e.g. $BiFeO_3$ and $BiMnO_3$. Interestingly, $BiFeO_3$ is the most studied multiferroics. Due to its small band gap (~2.2 eV) $BiFeO_3$ can be regarded as a visible light active photocatalyst. Recently it was reported that $SrTiO_3$ coated $BiFeO_3$ core shell nano-particles can produce H_2 under visible light irradiation. It is also reported that Gd doped $BiFeO_3$ shows improved photocatalytic activity.

Bismuth is an interesting cation from both photocatalytic and technological point of view. Thus for the modeling of a perovskite structured photocatalyst, Bi is a good choice for the A site cation. Among the first row transition metals, V is considered as good choice for the B site cation since many of the V containing compounds show a good photocatalytic activity; $BiVO_4$ is one of the widely studied oxygen evolution catalysts. In addition, recently Liu *et al.*, [47] has reported a series of vanadium based solid solutions showing effective overall water splitting under UV light. Hence, Bi and V based perovskites represent an attractive possibility for developing a new visible light active photocatalysts. Following the trend of Bi-based semiconductors with low band gap, formed by the first row transition elements ($BiFeO_3$ and $BiMnO_3$), $BiVO_3$ can be anticipated as another potential photocatalyst. Surprisingly, $BiVO_3$ has not yet been synthesized. It is not known whether it is stable and so cannot be experimentally investigated. Before undertaking experimental work on its synthesis, it would be beneficial to know about its thermodynamic stability and band structure to be able to estimate its potential as a photocatalyst.

1.4 Aim of the work and structure of the thesis

Ab-initio calculations, especially density functional theory (DFT) based calculations, play a significant role in a wide area of science. In the field of photocatalysis, band structure calculations are often employed within the framework of DFT and seem to be an inevitable part in certain extremely time consuming laboratory tasks. The aim of the present dissertation is to investigate several different approaches for modification and improvement of existing semiconductor photocatalysts and development of new compounds that can serve as a good photocatalyst under visible light irradiation. Following this goal we have analyzed the modulation of Fe_2O_3 electron structure by compositional modification and rock-salt structures by external electric field. In the second part, inspired by Bi based photocatalysts, we have analyzed the stability, structural and electronic properties, and vibrational properties of a novel Bi based system; $BiVO_3$ from the perspective of photocatalytic water splitting. The detailed explanation of these three segments of the work follows below.

a) Improving the photocatalytic properties of Fe_2O_3 by creating a ternary solid solution with Cr_2O_3 and Al_2O_3. (Chapter 3)

TiO_2 is the most studied semiconductor, due to its capability to split water when irradiated with UV light. Due to its extremely wide band gap, modulating the visible light sensitivity of TiO_2 is challenging. Fe_2O_3 has evolved as an alternative to TiO_2 due to its low band gap, abundance and low cost. As shown in Fig. 1-6, the conduction band minima of Fe_2O_3 is too low to produce H_2, but this can be partially addressed in an inexpensive way by an external bias using dye sensitized solar cells as Grätzel and coworkers have shown. The key problem lies in the charge transfer kinetics of Fe_2O_3 due to its extremely small hole-diffusion length and low minority carrier life time. This issue, however, has to be addressed in detail in order to use Fe_2O_3 for overall water splitting. One way to handle this issue is to increase the width of the valence band. This can be achieved by incorporating a smaller ion into the Fe lattice and or a cation with partially filled *d* orbitals. Fe_2O_3 has corundum structure, making solid solutions with corundum structured Cr_2O_3 and Al_2O_3. In the present work we aim to investigate a series of ternary solid solutions made from Fe_2O_3, Cr_2O_3, and Al_2O_3. First we will address the stability of twelve different compositions from Fe_2O_3-Cr_2O_3-Al_2O_3 system within the corundum solubility limit. Then we present an analysis on the electronic structure of the both end members as well as the ternary oxides. Further, we investigate the structure as well as the electronic band structure related properties that would possibly increase the photocatalytic activity of hematite.

b) Modulation of the electronic band structure of wide band gap semiconductors by an external static electric field. (Chapter 4)

Through this approach we aim to study the effect of electric field on the electronic properties of a series of wide band gap materials with rock-salt crystal structure. First we begin with a series of six simple cubic structures namely LiF, LiCl, NaF, NaCl, KF, and KCl from the alkali halide family. The effect of electric field on electronic properties such as band gap and band width will be analyzed. Later, the dielectric strength of these materials will be calculated by computational means by using a general equation proposed by Callen. Afterwards the method will be extended to highly photoactive compounds from the same structural family, namely AgCl and AgBr. We will investigate the possibility of tuning the electronic properties of AgCl and AgBr with the method that we have formulated for the NaCl crystal family. Finally, the dielectric breakdown strength of AgCl and AgBr will be calculated and the key parameters controlling the accurate prediction of the breakdown strength will be addressed.

c) Modeling of a novel $BiVO_3$ perovskite. (Chapter 5)

First we will evaluate the tolerance factor, a parameter indicating the stability of a perovskite structure. Then, in order to begin the computational study, we will predict the crystal structure of $BiVO_3$ in cubic and other polymorphs using the *SPuDs* crystallographic structure predicting software by minimizing the global stability index. The relative stability of the structure with minimum global stability index will be analyzed with respect to the cubic. A spin polarized calculation will be performed to obtain the right magnetic structure. There after a full structural characterization will be performed by running a geometry optimization. Later the electronic properties controlling the photocatalytic properties will be analyzed with respect to the most stable structure. Finally, the dynamical stability of the material will be analyzed by running the vibrational frequency calculation at the zone center and the IR and Raman modes will be calculated.

Before presenting the results, in the next chapter (Chapter 2) a general introduction to the theoretical methods and the structure of the software program that we have used for the present study, will be provided.

2 THEORETICAL BACKGROUND

2.1 Introduction

In the last thirty years atomistic simulations have undergone rapid expansion, thanks to the increase in available computational power. Several approaches are traditionally followed for electronic structure calculations. These approaches are basically grouped into two categories, namely *ab initio* methods and *empirical* (*semi-empirical*) methods. Hartree-Fock and density functional theory based methods are the widely used *ab initio* methods. In general, these methods utilize a variational approach to calculate the ground state energy of a many-body system, where the system is defined at the atomic level. In contrast to *ab initio* approaches, the *empirical* methods include approaches such as the Orthogonalized Plane Wave (OPW), tight-binding (also known as the Linear Combination of Atomic Orbitals (LCAO) method), the $\mathbf{k} \cdot \mathbf{p}$ method, and the local, or the non-local empirical pseudopotential method (EPM). These methods involve empirical parameters to fit experimental data such as the band-to-band transitions at specific high-symmetry points derived from optical absorption experiments.

Even though great computer power is required, *ab initio* methods are convenient, especially for smaller systems, for electronic structure calculations as they do not require any empirical data. First principle approaches, based on a parameter free implementation of basic theorems in physics and chemistry, that were first restricted to the study of model systems, are nowadays commonly used for predicting the electronic properties of complex systems. Hartree-Fock is the simplest type of *ab initio* method, in which the correlation effects are neglected. To date several post-Hartree-Fock methods (Møller–Plesset perturbation theory, coupled cluster approach, configuration interaction, etc.) which include the correlation effects have been formulated for a more accurate description of the electronic structure. In this chapter, we provide an overview of the basic ideas behind one of the most popular and well developed first principle approaches, Density Functional Theory (DFT), and its practical implementation in CRYSTAL code.

2.2 The many body problem

Our starting point is the solution of the time independent non relativistic Schrödinger equation describing a system of matter consisting of M nuclei and N electrons. This represents the eigenvalue equation for the total energy operator, the Hamiltonian $\hat{H}$, and defines all states Ψ and their related energies E,

$$\hat{H}\Psi = E\Psi. \qquad 2.1$$

In the general representation of matter, with electrons in the presence of positively charged heavy nucleus, it is straight forward to assume that the Schrödinger equation can be separated into the independent electronic and nucleonic parts. This is the Born-Oppenheimer approximation (BOA) [26], which is valid when the electrons reach equilibrium on a time scale that is much shorter compared to the time scale on which the nuclei move. The approximation separates the states into independent states for nuclei Ψ_n and electrons Ψ_e, with energies E_n and E_e. Consequently the Hamiltonian is split into corresponding terms, $\hat{H}_n$ and $\hat{H}_e$. The interaction energy between the nuclei and electrons, however, is placed in the electronic part. Hence one would write, $\Psi = \Psi_n + \Psi_e$ and $\hat{H} = \hat{H}_n + \hat{H}_e$. For a many electron system the Hamiltonian operator can be written as:

$$\hat{H} = -\frac{\hbar^2}{2m_e}\sum_{i=1}^{N}\nabla_{\mathbf{r}_i}^2 - \frac{\hbar^2}{2}\sum_{j=1}^{M}\frac{1}{M_j}\nabla_{R_i}^2 - \sum_{i=1}^{N}\sum_{j=1}^{M}\frac{e^2 Z_j}{\left|\mathbf{r}_i - \mathbf{R}_j\right|}\nabla_{\mathbf{R}_i}^2 + \sum_{i<j}\frac{e^2}{\left|\mathbf{r}_i - \mathbf{r}_j\right|} + \sum_{i<j}\frac{e^2 Z_i Z_j}{\left|\mathbf{R}_i - \mathbf{R}_j\right|}, \qquad 2.2$$

where m_e and M_j are the masses of the electron and the nuclei respectively, whereas e and eZ_j are the electronic and nuclear charges respectively, and $\mathbf{r}_i (i = 1, 2, ..., N)$, and $\mathbf{R}_j (j = 1, 2, ..., M)$ are the coordinates of the electrons and nuclei. The first two terms on the right hand side of the Eq. (2.2), represents the electronic and nuclear kinetic energies, whereas the remaining terms represents the electrostatic interaction between electrons-nuclei, electron-electron, and nuclei-nuclei, respectively.

Recalling the assumptions of BOA, i.e., since the mass of electrons are much smaller than that of the nuclei ($m_e / M_j \leq 10^{-3}$), the nuclei moves much slower than electrons. Hence, to a first approximation, one could simply assume that the electrons are moving in a fixed potential experienced from the clamped nuclei. With this approximation the second term (kinetic energy of the nuclei) in Eq. (2.2) are set to zero and the fifth term (the repulsion between the nuclei) is set to a constant. The BOA therefore allows disentangling the nuclear and electronic degrees of freedom, and the motion of electrons is then described by the electronic wave function:

$$\hat{H}_{\mathrm{el}}(\{\mathbf{r}_i\};\{\mathbf{R}_j\})\Psi_n(\{\mathbf{r}_i\};\{\mathbf{R}_j\}) = E_n(\{\mathbf{R}_j\})\Psi_n(\{\mathbf{r}_i\});\{\mathbf{R}_j\}). \qquad 2.3$$

Wherein Ψ_n represents the eigenstates of the many-electron problem, whereas the subscript n denotes the electronic quantum number. The electronic Hamiltonian in Eq. (2.3) becomes:

$$\hat{H}_{\mathrm{el}} = -\frac{\hbar^2}{2m_e}\sum_{i=1}^{N}\nabla_{\mathbf{r}_i}^2 - \sum_{i=1}^{N}\sum_{j=1}^{M}\frac{e^2 Z_j}{\left|\mathbf{r}_i - \mathbf{R}_j\right|}\nabla_{\mathbf{R}_i}^2 + \sum_{i<j}\frac{e^2}{\left|\mathbf{r}_i - \mathbf{r}_j\right|}. \qquad 2.4$$

Hence our concern in the Hamiltonian is reduced only to the electronic part, which describes the interacting electrons that move in a static external potential created by the charged nuclei. The solution of Eq. (2.3) gives the so called adiabatic potential energy surfaces $E_n(\{\mathbf{R}_j\})$ of which the most relevant is the ground state energy surface $E_0(\{\mathbf{R}_j\})$. The electronic energy E_{el} can then be obtained as the expectation value of the electronic Hamiltonian in Eq. (2.4), i.e.,

$$E_{\mathrm{el}} = \left\langle \Psi_e \middle| \hat{H}_{\mathrm{el}} \middle| \Psi_e \right\rangle$$

$$E_{\mathrm{el}} = \int\int\ldots\int\left(-\frac{\hbar^2}{2m_e}\sum_{i=1}^{N}\Psi_e^*\nabla_{\mathbf{r}_i}^2\Psi_e - \sum_{i=1}^{N}\sum_{j=1}^{M}\frac{e^2 Z_j}{\left|\mathbf{r}_i - \mathbf{R}_j\right|}\left|\Psi_e\right|^2 + \sum_{i<j}\frac{e^2}{\left|\mathbf{r}_i - \mathbf{r}_j\right|}\left|\Psi_e\right|^2\right)d\mathrm{x}_1 d\mathrm{x}_2 \ldots d\mathrm{x}_{\mathrm{N}}. \qquad 2.5$$

The *Rayleigh-Ritz* variational principle can be used to find the many electron wave function, Ψ_0, that minimizes the energy expectation value yielding E_0.

$$E_0 = \min_{\Psi} \langle \Psi | \hat{H}_{\mathrm{el}} | \Psi \rangle, \text{ has minimum for } \Psi = \Psi_0 \qquad 2.6$$

The solution of the electronic problem can be further simplified within the framework of DFT.

2.3 Density functional theory – an overview

Contrary to Hartree-Fock and post Hartree-Fock approaches, DFT is computationally less demanding. During the past decades, it has been successfully used for studying ground state properties of many different systems. For a review on DFT see for instance Gross *et al*. [48]

2.3.1 Hohenberg-Kohn theorem

The basic idea of DFT is the proof of Hohenberg and Kohn [49] that the ground state electronic energy is determined completely by the electron density °. In other words there exist a one-to-one correspondence between the electron density of a systems and the energy and hence all properties of the system can be considered to be unique functionals of ground state density. The relation between $°(\mathbf{r})$ and the many electron wavefunction Ψ_e is:

$$°(\mathbf{r}) = N \iint \ldots \int \left| \Psi_e(\mathbf{r} \pm 1, \mathrm{x}_2, \ldots, \mathrm{x}_{\mathrm{N}}) \right|^2 d\pm_1 d\mathrm{x}_2 \ldots d\mathrm{x}_{\mathrm{N}}. \qquad 2.7$$

The expression on the right hand side is similar to the wavefunction normalization integration but without one of the spatial integrals, and thus one coordinate is left free. Here we have arbitrarily removed the integration over the first coordinate r_1, in fact, due to the antisymmetric property of the wavefunction; any of the special integrals can be replaced. In Eq. (2.5), on the right hand side, the first and last terms can be written down easily if we know how many electrons are present, but the middle term depends on $\sum_{j=1}^{M} \frac{-Z_j}{\left|\mathbf{r}_i - \mathbf{R}_j\right|}$, which is a function of nuclear charges and locations. This quantity is called the *external potential*, symbolized $³_{ext}(\mathbf{r}_i)$. However, Hohenberg and Kohn were able to prove that there is a unique relation between the electron density $°(\mathbf{r})$ and the external potential. Now, if one looks at the three terms in the right hand side of Eq. (2.5), one sees that the term for the external potential $\text{³}_{ext}(\mathbf{r})$ can easily be rewritten in terms of the electron density,

$$\begin{aligned} V_{\text{ext}} &= \iint \ldots \int \sum_{i=1}^{N} \left|\Psi_e\right|^2 \text{³}(\mathbf{r}_i)\, d\text{x}_1 d\text{x}_2 \ldots d\text{x}_{\text{N}} = \\ &= \frac{1}{N}\sum_{i=1}^{N} \int \text{°}(\mathbf{r}_i)\text{³}(\mathbf{r}_i)\, d\mathbf{r}_i = \int \text{°}(\mathbf{r})\text{³}(\mathbf{r})\, d\mathbf{r}. \end{aligned} \qquad 2.8$$

The other two terms of the electronic energy in Eq. (2.5) are not in explicit density functional form, but can at least be written as functionals of the many-electron wave function.

$$E_{\text{el}} = T\left[\Psi_{\text{e}}\right] + U\left[\Psi_{\text{e}}\right] + V_{\text{ext}}\left[\text{³},\text{°}\right] = F\left[\Psi_{\text{e}}\right] + V_{\text{ext}}\left[\text{³},\text{°}\right]. \qquad 2.9$$

At this point there arises a question central to DFT: “is it possible also to write $F[\Psi_{\text{e}}]$ as a density functional $F[\text{°}]$?” If such a functional exists, it will be a universal functional independent of the external potential. An early attempt to construct such an approximation from basic physics principles were done by Thomas and Fermi [50, 51]. They used the electrostatic energy of a classic repulsive gas $J[\text{°}]$ as a simplest approximation for the U term and Thomas-Fermi functional $T_{TF}[\text{°}]$ for the total kinetic energy term T in F. The Thomas-Fermi approximation for the internal energy thus is:

$$F[\text{°}] \approx T_{TF}[\text{°}] + J[\text{°}], \qquad 2.10$$

where,

$$\begin{aligned} J[\text{°}] &= \frac{1}{2}\left(\frac{e_c^2}{4\text{®£}_0}\right) \iint \frac{\text{°}(\mathbf{r}_1)\text{°}(\mathbf{r}_2)}{\left|\mathbf{r}_1 - \mathbf{r}_2\right|} d\mathbf{r}_1 d\mathbf{r}_2. \\ T_{TF}[\text{°}] &= \frac{3}{5}(3\text{®}^2)^{2/3}\left(\frac{\hbar^2}{2m_e}\right)\int \text{°}^{5/3}(\mathbf{r})\, d\mathbf{r}. \end{aligned} \qquad 2.11$$

The early efforts of Thomas and Fermi to find the exact form of the electronic energy functionals, and the further extension along same ideas were all based on reasonable approximations. Later on a more rigorous theoretical framework was formulated after two famous theorems proved in the work of Hohenberg and Kohn [49]. The first Hohenberg and Kohn theorem states that the ground state electron density $\text{°}(\mathbf{r})$ determines the potential of a system $\text{³}(\mathbf{r})$ within an additive constant.

Alternatively, "*the electron density determines all ground state properties of a system*". The ground state wavefunction is also a ground state property of the system and can therefore be considered to be functional of the ground state density $\Psi_0[\circ]$. Thus the existence of total energy functional $E_{\mathrm{el}}[\circ]$ and an internal energy functional $F[\circ]$ directly follows as:

$$E_{\mathrm{el}}[\circ] = \left\langle \cdot_0[\circ] \middle| \hat{H} \middle| \cdot_0[\circ] \right\rangle, \qquad 2.12$$

and

$$F[\circ] = f[\cdot_0[\circ]]. \qquad 2.13$$

The second Hohenberg-Kohn theorem reworks the *Rayleigh-Ritz variational principle* into a DFT variational principle [52] for the total energy combination $F[\circ] + V[{}^3, \circ]$. Equation (2.6) becomes,

$$\begin{aligned} E_0 = \min_{\Psi} \left\langle \Psi \middle| \hat{H}_{\mathrm{el}} \middle| \Psi \right\rangle = \min_{\circ} \min_{\Psi \to \circ} \left\langle \Psi \middle| \hat{T} + \hat{U} + \hat{V}_{ext} \middle| \Psi \right\rangle = \\ = \min_{\circ} \left\langle \Psi \middle| F[\circ] + V[{}^3, \circ] \middle| \Psi \right\rangle. \end{aligned} \qquad 2.14$$

Thus the many electron problem has thus been rewritten into what looks like a straight forward minimization in a three dimensional quantity $\circ[\mathbf{r}]$. So once the functional $F[\circ]$ and the expression for the external potential are known, the exact ground state energy and the potential can be found. Unfortunately, the exact expression of $F[\circ]$ is not known, so eventually approximations are needed.

2.3.2 Kohn-Sham equations

Soon after the work of Hohenberg and Kohn, Kohn and Sham [53] proposed a method for calculating the main contribution to the kinetic energy functional with good accuracy and is known as the Kohn-Sham (KS) method. The core idea was to rewrite the system of many interacting electrons as a system of non-interacting Kohn-Sham particles. The particles behave as non-interacting electrons. They divided the internal electronic energy functional $F[\circ]$ into three parts,

$$F[\circ] = T_s[\circ] + J[\circ] + E_{xc}[\circ]. \qquad 2.15$$

Here $T_s[\rho]$ is the kinetic energy of a system of non-interacting Kohn-Sham particles with particle density ρ; $J[\rho]$ is the electrostatic repulsive energy of a classical repulsive gas (c.f. Eq. (2.11)) and $E_{xc}[\rho]$ is the exchange-correlation (XC) energy, which is the unknown part of $F[\rho]$. The DFT variational principle for the ground state electronic energy presented in Eq. (2.14) can be expressed in the new quantities,

$$E_0 = \min_{\rho} \left\langle \Psi \middle| T_s[\rho] + J[\rho] + E_{xc}[\rho] + V[\upsilon, \rho] \middle| \Psi \right\rangle. \qquad 2.16$$

In the language of variational calculus, this energy minimization can be rewritten as stationary condition for the electron density:

$$\frac{\delta T_s[\rho]}{\delta \rho} + \frac{\delta J[\rho]}{\delta \rho} + \frac{\delta E_{xc}[\rho]}{\delta \rho} + \frac{\delta V[\upsilon, \rho]}{\delta \rho} = 0. \qquad 2.17$$

Now if we apply DFT to a system of non-interacting Kohn-Sham particles, the DFT variational principle become:

$$E_s = \min_{\rho}(T_s[\rho] + V[\upsilon_{eff}, \rho]). \qquad 2.18$$

Here we use E_s as the ground state energy of the Kohn-Sham particles and $v_{eff}(\mathbf{r})$ is the potential in which they move. The stationary condition becomes:

$$\frac{\delta T_s[\rho]}{\delta \rho} + \frac{\delta V[\upsilon_{eff}, \rho]}{\delta \rho} = 0. \qquad 2.19$$

From Eqs. (2.17 and 2.19),

$$\frac{\delta V[\upsilon_{eff}, \rho]}{\delta \rho} = \frac{\delta J[\rho]}{\delta \rho} + \frac{\delta E_{xc}[\rho]}{\delta \rho} + \frac{\delta V[\upsilon, \rho]}{\delta \rho}. \qquad 2.20$$

The functional derivatives are evaluated on both sides to give:

$$\upsilon_{eff}(\mathbf{r}) = \upsilon_{xc}(\mathbf{r}) + e^2 \int \frac{\rho(\mathbf{r}')}{|\mathbf{r} - \mathbf{r}'|} d\mathbf{r}' + \upsilon(\mathbf{r}), \qquad 2.21$$

where the exchange correlation potential $\upsilon_{xc}(\mathbf{r})$ is defined as:

$$\upsilon_{xc}(\mathbf{r}) = \frac{\delta E_{xc}[\rho]}{\delta \rho}. \qquad 2.22$$

The total energy of the non-interacting Kohn-Sham particle system with effective potential ν_{eff}, has the same ground state density as the system of fully interacting system. The energies of two systems are closely related by the following equation,

$$E_0 = E_s - J[\rho] + E_{xc}[\rho] - V[\nu_{xc}, \rho]. \qquad 2.23$$

Now, one can perform a minimization of the energy of an auxiliary problem of Kohn-Sham particles, Eq. (2.18), instead of a many electron energy minimization as in Eq. (2.16). The non-interacting particle problem can be treated explicitly by solving the separable Schrödinger equation. The separation procedure leads to the Kohn-Sham orbital equation, which determines the one particle Kohn-Sham orbitals $\phi_i(\mathbf{r})$ and the Kohn-Sham orbital energies ε_i,

$$-\left(\frac{\hbar^2}{2m_e}\right)\nabla^2\phi_i(\mathbf{r}) + \nu_{eff}(\mathbf{r})\phi_i(\mathbf{r}) = \varepsilon_i\phi_i(\mathbf{r}). \qquad 2.24$$

Actual one particle equations are constructed as a combination of position dependent part and spin functions, $\Psi_i(\mathbf{r},\sigma) = \phi_i(\mathbf{r})\,\chi_i(\mathbf{r}).$ The particle density can be obtained by inserting the many particle wave function into the usual expression for the electron density Eq. (2.7) as,

$$\rho(\mathbf{r}) = \sum_i \left|\phi_i(\mathbf{r})\right|^2, \qquad 2.25$$

where the sum is taken over all the occupied states *i*. The total energy of the system is

$$E_s = \sum_i \varepsilon_i. \qquad 2.26$$

Equations (2.21 to 2.26) are the Kohn-Sham equations and are at the heart of any Kohn-Sham DFT based computer algorithm. Due to the need of electron density, these equations cannot be solved directly from top down; alternatively, an iterative scheme which works towards self-consistency (SCF) is used.

2.3.3 Approximations to the exchange correlation functional

The form of the E_{xc} functional discussed in the previous section is pretty complex. However, it has been made clear that the most difficult parts have been condensed into accurately describing the $E_{xc}[\rho]$ functional. The exchange component $E_x[\rho]$ of the XC functional describes the energy lowering due to the tendency of the electrons of same spin to exclude each other; on the other hand the correlation component $E_c[\rho]$ accounts for the additional energy lowering arise due to the mutual exclusion of electrons with opposite spin. The practical advantage of representing $E[\rho]$ in the form of Eq. (2.16) is that the unknown $E_{xc}[\rho]$ is smaller than the known terms $T_s[\rho]$, $J[\rho]$, and $V[\rho]$. One thus expect that even a simple reasonable approximation for $E_{xc}[\rho]$ would provide reasonable values for $E[\rho]$. Unfortunately, the form of the universal XC energy functional to be used is unknown. Hence, in practice, approximations are needed. Some successful practical approximations for the exchange-correlation functional are presented here.

The local density approximation (LDA) [54, 55] is the most straight forward rather simple approximation for the XC energy. The main ideas behind LDA are (i) the XC energy per particle at point $\mathbf{r}$, $\varepsilon_{xc}(\mathbf{r})$, depends only on the density at $\mathbf{r}$ and (ii) $\varepsilon_{xc}(\mathbf{r})$ is equal to the XC energy per particle of a homogeneous electron gas of density $\rho(\mathbf{r})$.

$$E_{xc}[\rho] = \int \rho(\mathbf{r})\varepsilon_{xc}^{LDA}(\mathbf{r})\, d\mathbf{r}, \qquad 2.27$$

with,

$$\varepsilon_{xc}^{LDA}(\mathbf{r}) = \varepsilon_{xc}^{hom}[\rho(\mathbf{r})]. \qquad 2.28$$

The exchange energy per particle of a homogeneous electron liquid is known; the exchange part of Eq. (2.27) can be obtained analytically and has a form,

$$\varepsilon_{x}^{hom}[\rho] = -\frac{3}{4\pi}(3\pi^2)^{1/3}\rho^{1/3}. \qquad 2.29$$

For the correlation part in Eq. (2.27), the situation is more complicated as the form of $E_c^{hom}[\rho]$ is not known exactly. Hence one must rely on the accurate values obtained by Caperley-Alder [56] from the quantum Monte-Carlo simulations. LDA owes its success to its simplicity and the success stories include the accurate description of structural and dynamical properties with fairly good accuracy, however the poor reproduction of cohesive energy and dielectric susceptibility still need to be solved.

In the LDA regime one exploits only the knowledge about the local value of electron density. Since any real system is spatially inhomogeneous, it would be useful if one could include the information about the rate of variation of the functional. A first step at doing this, a step ahead LDA, is the semi local functionals, collectively called Generalized Gradient Approximations (GGA) [26, 57-59]. In GGA, one tries to systematically calculate gradient corrections of the form $|\nabla\rho(\mathbf{r})|, |\nabla\rho(\mathbf{r})|^2, \nabla^2\rho(\mathbf{r})$, etc., to the LDA. In GGA the XC energy functional takes the form,

$$E_{xc}^{GGA}[\rho] = \int \rho(\mathbf{r}).\varepsilon_{xc}^{GGA}[|\nabla\rho(\mathbf{r})|; |\nabla\rho(\mathbf{r})|^2; \nabla^2\rho(\mathbf{r})]\, d\mathbf{r}. \qquad 2.30$$

GGA generally improves the cohesive energy values, bond lengths and lattice parameters. However it has a rather limited effect on the dielectric properties. Nowadays the most popular GGAs are PBE [60] (proposed by Perdrew, Burke and Ernzerhof in 1996) and BLYP (combination of Becke's exchange functional [61] with the correlation functional of Lee Yang and Par [62]). Despite these advances, all GGA's and LDA's suffers from what is called self-interaction problem. Literally, traditional exchange correlation functionals cancel only a part of the Hartree self-interaction contribution since they decay too fast in the long wavelength limit.

2.3.4 Hybrid functionals

Hybrid functionals represent an interesting class of functionals with greatly improved predictive power compared to traditional functionals as they include a fraction of Fock-exchange to overcome the self-interaction problem. Through hybrids Becke derived [63-65] a new coupling between HF and DFT by retaining their simplicity and computational efficiency. The logic behind the construction of the hybrid functional was from the expression for the XC energy, E_{xc}, called the adiabatic connection formula, from KS-density functional theory. One among the several representation of E_{xc}, has the following convenient form:

$$E_{xc} = \int_0^1 U_{xc}^{\lambda}\, d\lambda. \qquad 2.31$$

Where, λ represents an inter-electronic coupling strength which literally connects the non-interacting KS reference system $(\lambda = 0)$ to a fully interacting real system

$(ª = 1)$ through a continuum of partially interacting systems $(0 \le ª \le 1)$, of which all of them have the same density °. A straight forward first approximation for the ª dependence of the integrand in Eq. (2.31) is a linear interpolation resulting in the following form for the XC energy:

$$E_{xc} \simeq \frac{1}{2}U_{xc}^{ª=0} + \frac{1}{2}U_{xc}^{ª=1}. \qquad 2.32$$

Here, $U_{xc}^{ª=0}$ is the XC potential of the non-interacting reference system and $U_{xc}^{ª=1}$ is the XC potential energy of the fully interacting system. The $U_{xc}^{ª=0}$ term could well be described using the HF theory, whilst a local type density functional treatment is necessary for the $U_{xc}^{ª=1}$ term as it represents the most local part of the electron interaction due to the correlation. Within the above formalism Becke proposed the so called "half-and-half" theory [64, 65] by clumping together the exact-exchange KS theory and the local density approximation as a semi-empirical model,

$$E_{xc} \simeq c_0 E_x + c_1 U_{xc}^{LDA}. \qquad 2.33$$

Where c_0, and c_1 represents the mixing parameters to be determined by approximate fits to firm experimental data. Through Eq. (2.33) Becke argues that $U_{xc}^{ª=0}$ is nothing but E_x. The quantity $U_{xc}^{ª=1}$ is the XC potential energy of the fully interacting system. Becke's hybrid "half-and-half theory" can be viewed not only as a correlation correction to the HF scheme but also as a method for incorporating exact exchange into the DFT formalism.

After the "half-and-half theory", Becke formulated the three parameter hybrid formula, which is arguably less connected to formal theory, but was more successful. This was the basis for the construction of the presently available hybrids functionals. B3LYP [63, 66] is one such, perhaps the most popular, hybrid functional and has the following form:

$$E_{xc} = E_{xc}^{LDA} + a_0(E_x - E_x^{LDA}) + a_x \Delta E_x^{B88} + a_c \Delta E_c^{PW91}. \qquad 2.34$$

Here $a_0 = 0.20$, $a_x = 0.72$, and $a_c = 0.81$ are the three empirical parameters determined by fitting the predicted values to a set of atomization energies. The last two terms of Eq. (2.34), ΔE_x^{B88} and ΔE_c^{PW91}, represents the widely used GGA correction to LDA exchange and correlation energies respectively. Different hybrid functionals can be constructed in the same way by varying the component functionals and by adjusting the values of the three empirical parameters. The recently implemented B1 [67] simplification also gained much attention from the scientific community due to its excellent predicting capability for ferroelectric crystals. The B1 parameterization can be obtained, by setting $a_x = 1 - a_0$ and $a_c = 1$ in Eq. (2.34), as:

$$E_{xc} = E_{xc}^{GGA} + a_0 (E_x - E_{xc}^{GGA}). \qquad 2.35$$

Where according to a fit by Becke, the remaining exchange mixing parameter, depending on the choice of the GGA functional, is equal to 0.16 or 0.28. Unlike the DFT+U methods, the value of the exact mixing parameter should only be dependent on the GGA functional that used and is not a semi empirical parameter. Thus the mixing parameter obtained with B1 formalism is transferrable. A suggested value of 0.25 by a pure theoretical study is often used for this parameter. In our study the B1 hybrid functional was parameterized according to Goffinet *et al.* [68] with the WC nonlocal exchange part and PBE nonlocal correlation part together with the optimized mixing parameter of 0.16. However, in order to implement the hybrid functional formalism in computer codes, it is quite common to use HF exchange to approximate the KS exchange used in the development of hybrid functionals.

2.3.5 Spin density functional theory

Up to this point we have omitted the spin coordinate from the wave function. The extension of DFT to spin polarized systems is quite necessary in order to investigate magnetic systems. In the spin polarized case one must define an electron density for both the alpha (up) and the beta (down) spin state: $\rho_\uparrow$ and $\rho_\downarrow$ or equivalently a total density of $\rho = \rho_\uparrow + \rho_\downarrow$, and a spin density $m = \rho_\uparrow - \rho_\downarrow$. All functional, for instance $E_{xc}(\rho)$ will depend on both densities: $E_{xc} \equiv E_{xc}(\mathbf{r};[\rho, m])$.

2.3.6 k - point sampling

In a periodic crystal, the fundamental unit cell is repeated to form an infinite system. Even though the periodicity can be in one, two or three dimensions, the later one is far more common and is characterized by three vectors $\mathbf{a_1}$, $\mathbf{a_2}$, and $\mathbf{a_3}$ spanning a vector space. Any single point in this direct lattice space is characterized by a vector $\mathbf{r}$ (i.e., a linear combination of $\mathbf{a}_1$, $\mathbf{a}_2$, and $\mathbf{a}_3$). In the same manner there exists a unique reciprocal space, corresponding to each direct cell, defined by the reciprocal vectors $\mathbf{b}_1, \mathbf{b}_2,$ and $\mathbf{b}_3$ derived from $\mathbf{a}_1, \mathbf{a}_2,$ and $\mathbf{a}_3$ obeying the orthonormality relation $\mathbf{a}_i\mathbf{b}_j = 2®¢_{ij}$. In reciprocal space the fundamental building block is called the first Brillouin zone. As in the case of direct lattice space, each point in the reciprocal space is uniquely represented by a vector $\mathbf{k}$ (usually designated as the wave vector). Since the lattice is periodic in nature, the potential energy of the crystal must also be periodic in nature, such that for a translation by any direct lattice vector $\mathbf{g}$ the potential energy does not change,

$$V(\mathbf{r}-\mathbf{g}) = V(\mathbf{r}). \qquad 2.36$$

Because of the symmetry constraints, the Schrödinger equation given in Eq. (2.1) should also be translation invariant; indicating that for a translation of the whole crystal by a lattice vector $\mathbf{g}$, the solution of the equation,

$$\hat{H}(\mathbf{r}+\mathbf{g})\Psi(\mathbf{r}+\mathbf{g}) = E\Psi(\mathbf{r}+\mathbf{g}), \qquad 2.37$$

agree with those of Eq. (2.1). According to *Bloch theorem*, the eigenfunctions with the correct symmetry relative to a potential of the form in Eq. (2.36) has the form of a plane wave times function with the periodicity of the lattice,

$$\Phi(\mathbf{r}+\mathbf{g};\mathbf{k}) = e^{i\mathbf{k}\bullet\mathbf{g}}\,\Phi(\mathbf{r};\mathbf{k}). \qquad 2.38$$

Here Φ is called the *Bloch function* (BF) and they span an infinite crystal. The wave vector $\mathbf{k}$ labels the different solutions to the Schrödinger equation given in Eq. (2.1). The BF has the following form,

$$\Phi(\mathbf{r};\mathbf{k}) = e^{i\mathbf{k}.\mathbf{r}}u(\mathbf{r},\mathbf{k}), \qquad 2.39$$

wherein $u(\mathbf{r},\mathbf{k})$ has the same periodicity of the lattice. Alternatively, *Bloch theorem* indicates that a crystalline orbital (CO) $\cdot\ _{n,k}(\mathbf{r})$ corresponding to the n^{th} band in the unit cell can be written as a wave like part and a cell periodic part $¨_n(\mathbf{r})$ called the *"Bloch orbital":*

$$\cdot\ _{n,k}(\mathbf{r}) = e^{i\mathbf{k}.\mathbf{r}\,¨}{}_n(\mathbf{r}). \qquad 2.40$$

The beauty of BFs is that they have interesting translational properties in reciprocal space. Consider a point $\mathbf{k'}$ in the reciprocal lattice obtained by the translation of $\mathbf{k}$ by any reciprocal lattice vector $\mathbf{K}$. If we apply *Bloch theorem* to the corresponding BF, $\Phi(\mathbf{r};\mathbf{k'})$, it is evident that $\Phi(\mathbf{r};\mathbf{k'})$ exhibits the same translational properties as $\Phi(\mathbf{r},\mathbf{k})$,

$$\Phi(\mathbf{r}+\mathbf{g};\mathbf{k'}) = e^{i(\mathbf{k}+\mathbf{K}).\mathbf{g}}\,\Phi(\mathbf{r};\mathbf{k}+\mathbf{K}) = e^{i\mathbf{k}.\mathbf{g}}\Phi(\mathbf{r};\mathbf{k'}), \qquad 2.41$$

and one would immediately see not only that $\Phi(\mathbf{r};\mathbf{k'})$ and $\Phi(\mathbf{r},\mathbf{k})$ can be referred to the same $\mathbf{k}$, but also that both of them are acceptable eigenfunctions of that $\mathbf{k}$ in Eq. (2.1). This behavior of BF allows us to restrict our analysis only to the first Brillouin zone. In fact the use of BFs has to be associated with the integration over the first Brillouin zone and would require *a priori* compute different quantities at a large number of **k**-points. In principle, the electronic wave functions at **k** points which are close to each other are almost identical, hence they are solved at a finite set of **k**-points and the results can be interpolated.

The block orbital in Eq. (2.40) can be expanded into a basis set of either plane wave functions $(¡_{\sim}^{PW})$

$$\begin{aligned} ¨_n(\mathbf{r}) &= \sum_{\sim}^{M_{basis}} C_{n\sim}\, ¡_{\sim}^{PW}(\mathbf{r}), \\ ¨_{n,k}(\mathbf{r}) &= e^{i\mathbf{k}.\mathbf{r}} \sum_{\sim}^{M_{basis}} C_{n\sim}\, ¡_{\sim}^{PW}(\mathbf{r}). \end{aligned} \qquad 2.42$$

Alternatively, the basis set can be selected as a set of nuclear centered (Gaussian) basis functions, from which a set of Bloch orbitals can be constructed:

$$¨_{n,k}(\mathbf{r}) = \sum_{\sim}^{M_{basis}} c_{n\sim}\, ¨_{k\sim}(\mathbf{r}) = \sum_{\sim}^{M_{basis}} \sum_{\mathbf{t}} c_{n\sim}\, e^{i\mathbf{k}\cdot\mathbf{t}}\, ¡_{\sim}^{GTO}(\mathbf{r}+\mathbf{t}). \qquad 2.43$$

The problem has now been transformed from treating an infinite number of orbitals (electrons) to only treating those within the unit cell as a function of the reciprocal lattice vector **k** in the first Brillouin zone. The set of functions $¡_{\sim}$ in Eq. (2.43) constitute the one particle basis functions given as inputs to calculations.

2.3.7 The DFT in CRYSTAL code

In this work all the calculations have been performed using the latest version of the CRYSTAL code [69, 70], CRYSTAL09 (hereafter referred as CR09). CR09 is an ab-initio HF/DFT LCAO (Linear combination of atomic orbitals: in the present sense “crystalline orbitals”) program for the treatment of periodic systems [71]. The program computes the electronic structure of periodic systems within Hartree Fock, density functional or various hybrid approximations. The Bloch functions of the periodic systems are expanded as linear combinations of atom centered Gaussian functions. Powerful screening techniques are used to exploit real space locality. Restricted (closed shell) and unrestricted (spin-polarized) calculations can be performed with all-electron and valence-only basis sets with effective core pseudo-potentials [72].

In CR09, the numerical solution of the KS orbital equation, i.e., Eq. (2.24), is obtained by constructing the crystalline orbitals (COs) as a linear combination of BFs constructed from atomic orbitals (AOs). The AOs are contracted linear spherical harmonic Gaussian Type Functions (GTFs), optimized for the crystalline environments. Analytically the $¡_{\sim}^{GTF}$ has the following form,

$$¡_{\sim}^{GFT} = e^{\left(-\sim r^{2}\right)} x^{l} y^{m} z^{n}, \qquad 2.44$$

where $\sim$ is the exponent and the *l, m,* and *n* are simply powers of the Cartesian coordinates. With the increase in the size of the basis set, the CPU time and the amount of disk space needed to store the temporary integrals increases dramatically. Thus one has to expand the orbital with less number of basis set without losing the accuracy. In most applications this is achieved by expanding the Gaussian functions as a contraction of individually normalized Gaussian primitives $g_j(\mathbf{r})$. They are characterized by the same center and angular quantum numbers but with different exponents:

$$¡_{i}(\mathbf{r}) = \sum_{j=1}^{s} d_{j} g_{j}(\mathbf{r}). \qquad 2.45$$

Here s and d_j are the length and coefficients of the contractions respectively. By proper choice of these quantities, the resulting contracted Gaussians can be used to mimic any functional form. Therefore one has to choose the exponents and the contraction coefficients of the primitives so as to lead the basis functions towards the desired properties. A typical basis set will have certain core functions with a large number of primitives and relatively large exponents. On the other hand the valence functions will have only few primitives with lower exponents. Basically, the core states are not in general affected by changes in chemical bonding. Hence, in order to reduce the computational expenses, especially for heavier atoms, the core states can be replaced by pseudopotentials. The idea behind the pseudopotentials is to treat the core electrons by their effect on the potential filled by the electrons in the valence shell by slightly modifying the Hamiltonians and moreover it is easier to incorporate relativistic effects in pseudopotentials formalism. High quality Gaussian basis sets are adopted for the present study. For heavier atom like bismuth, pseudopotentials are used to treat the core electrons.

2.3.7.1 Treatment of the Coulomb problem

One of the main strengths of the calculation scheme in CR09 is its ability in accurately evaluating the Coulomb interactions described by the nonlocal exchange contributions to Fock and KS operators. Basically these interactions are evaluated without imposing any "cutoff" and all the charges are correctly introduced in the summation of the whole Coulomb series up to infinity. The sole approximation appears in the transformation of the infinite series of long range bielectronics integrals into an infinite series of monoelectronic integral, which is evaluated according to Ewald techniques. The transformation is performed via a multipole analysis of the charge density. The use of this technique in the periodic LCAO scheme is documented in [73, 74]. An abstract of this technique is given here.

In the electrostatic contribution to the real space Fock and KS matrices, there appear infinite summations of Coulomb terms. Each matrix element refers to the interaction of a charge distribution $°_{12}^{\mathbf{o},\mathbf{g}}(\mathbf{r})$ with the charge density of the whole system $°(\mathbf{r})$:

$$\left(F_{12}^{\mathbf{g}}\right)_{Coulomb} = \iint d\mathbf{r}d\mathbf{r}'\, °_{12}^{\mathbf{o},\mathbf{g}}(\mathbf{r}) \frac{1}{|\mathbf{r}-\mathbf{r}'|}\, °(\mathbf{r}') \qquad 2.46$$

where

$$\circ^{\mathbf{o},\mathbf{g}}_{12}(\mathbf{r}) = \text{¡}^{\mathbf{o}}_{1}\,\text{¡}^{\mathbf{g}}_{2}(\mathbf{r}). \tag{2.47}$$

The lattice vector $\mathbf{o}$ refers to the reference cell of the crystal. Similar terms also appear in the evaluation of the Coulomb contribution to the total energy:

$$E_{coulomb} = \frac{1}{2N}\iint d\mathbf{r}d\mathbf{r'}\circ(\mathbf{r})\frac{1}{|\mathbf{r}-\mathbf{r'}|}\circ(\mathbf{r'}), \tag{2.48}$$

which corresponds to the interaction of whole charge density with itself. The nuclear-electron and the nuclear-nuclear contribution to the charge density are evaluated without approximations using Ewald summation. However the electron-electron Coulomb terms are much more complicated and are evaluated using a complex approximation scheme. The general contribution to the matrix element may be written as,

$$\left(F^{\mathbf{g}}_{12}\right)^{e-e}_{Coulomb} = \sum_{3,4,\mathbf{l}} P^{\mathbf{l}}_{34}\sum_{\mathbf{h}}\iint d\mathbf{r}d\mathbf{r'}\circ^{\mathbf{o},\mathbf{g}}_{12}(\mathbf{r})\frac{1}{|\mathbf{r}-\mathbf{r'}|}\circ^{\mathbf{h},\mathbf{h+l}}_{34}(\mathbf{r'}), \tag{2.49}$$

here P_{34} is an element of the density matrix and the two new lattice vector labels (**l** and **h)** have been introduced to identify the cell containing the two components of $\circ_{34}$.

In Eq. (2.49), the **l** vector sum converges rapidly; by contrast the **h** vector sum decays only Coulomb like and hence converges very slowly and conditionally. Hence the various infinite series contributions to the matrix elements are approximated using different techniques. The bielectronic Coulomb integrals are disregarded when the space integral corresponding to either of the overlap distributions ($P^{\mathbf{g}}_{12}$, and $P^{\mathbf{l}}_{34}$) is less than a predefined threshold, ITOL1. The conditionally convergent Coulomb series over **h** vector is approximated beyond a threshold using a distributed point multipole model of the charge distribution. In this method the local basis functions associated with each nuclear site in the reference cell are factorized into nonintersecting sets q (shells) sharing asymptotic decay properties and for each shell, the charge density of an associated shell distribution is then defined according to a Mulliken partition scheme as:

$$\circ^{\mathbf{h}}_{q}(\mathbf{r}) = \sum_{3\in q}\sum_{4}\sum_{\mathbf{l}} P^{\mathbf{l}}_{34}\left(\text{¡}^{\mathbf{h}}_{3}(\mathbf{r})\,\text{¡}^{\mathbf{h+l}}_{4}(\mathbf{r})\right). \tag{2.50}$$

This definition saturates the {4, **l**} indices of the basis function $¡_4^{\mathbf{h}+\mathbf{l}}$, and allows the conversion of many four-center bielectronic integrals between overlap distributions into a single three-center integral between an overlap distribution and shell distribution. The list of **h** vectors is partitioned into finite internal set {$\mathbf{h}^{bi}$} and an infinite external set {$\mathbf{h}^{mono}$} for $¡_1^{\mathbf{0}}¡_2^{\mathbf{g}}(\mathbf{r})$, using overlap criteria and a penetration threshold ITOL2. The electron-electron Coulomb contribution to the Fock matrix is then split into internal and external terms:

$$\left(F_{12}^{\mathbf{g}}\right)_{Coulomb}^{e-e}=\left(F_{12}^{\mathbf{g}}\right)_{Coulomb}^{bi}+\left(F_{12}^{\mathbf{g}}\right)_{Coulomb}^{mono}. \qquad 2.51$$

The bielectronic part is calculated through explicit evaluation of the four-center bielectronic integrals $I(12\mathbf{g};34\mathbf{l})$, to give:

$$\left(F_{12}^{\mathbf{g}}\right)_{Coulomb}^{bi}=\sum_{3,4,\mathbf{l}}P_{34}^{\mathbf{l}}I(12\mathbf{g},34\mathbf{l})=\sum_{3,4,\mathbf{l}}P_{34}^{\mathbf{l}}\sum_{\mathbf{h}}^{\{bi\}}\iint d\mathbf{r}d\mathbf{r'}\,¡_1^{\mathbf{0}}¡_2^{\mathbf{g}}\frac{1}{|\mathbf{r}-\mathbf{r'}|}¡_3^{\mathbf{h}}¡_3^{\mathbf{h}+\mathbf{l}}. \qquad 2.52$$

The monoelectronic term, which involves an infinite sum of Coulomb integrals involving electronic distributions that are “external” to each other, is calculated in an approximate way. The potential at each point $\mathbf{r'}$ due to each shell distribution $°_q^{\mathbf{h}}(\mathbf{r})$ is given to a good approximation by the spherical multipolar expansion:

$$°_q^{\mathbf{h}}(\mathbf{r'})=\int d\mathbf{r}\frac{°_q^{\mathbf{h}}}{|\mathbf{r}-\mathbf{r'}|}\cong\sum_{l=0}^{l^{\max}}\sum_{m=-l}^{l}¥_q^{l,m}\Phi^{l,m}\left(r-s_q-\mathbf{h}\right). \qquad 2.53$$

Here $¥_q^{l,m}$ is the *l*, *m* multipole of the shell charge distribution centered at s_q (the position of the function $¡_3$ in cell **h**) and the filed term $\Phi^{l,m}(\mathbf{r})$ represents the potential at the point **r** due to an infinite array of unit point multipoles $¥^{l,m}$. The multipole expansion is truncated at some maximum value l^{max} (which may be up to six from two being four as the default in CR09). With this approximation the external Coulomb contribution to the Fock matrix may be rewritten as:

$$\left(F_{12}^{\mathbf{g}}\right)_{Coulomb}^{mono}=\sum_{l=0}^{l^{\max}}\sum_{m=-l}^{l}\sum_{\mathbf{h}}^{\{\mathbf{h}^{EXT}\}}\sum_{q}\int d\mathbf{r}¥_q^{l,m}\Phi^{l,m}(\mathbf{r'}-s_q-\mathbf{h}), \qquad 2.54$$

where the sum over **h** in the field terms are treated using Ewald techniques. This approximate scheme speeds up the calculation and at the same time lowers the amount of disk space needed without losing accuracy.

The exchange series, in general, does not require particular handling as would need for the Coulomb series, however, a careful selection is necessary for the terms contributing to the Fock exchange and to the total energy. The exchange series summation is controlled by a third overlap tolerance parameter ITOL3. The actual behavior of the *P* matrix element is somewhat complicated due to its dependence on the physical nature of the compound, orthogonality constrains and the quality of the basis functions. Hence a pseudo-overlap criterion is adopted for the different range of valence and core levels and is controlled by two tolerances namely ITOL4 and ITOL5. This truncation scheme is fairly efficient in terms of space occupation and computer time.

2.3.7.2 Implementation of hybrid functionals

B3LYP in CRYSTAL is a combination of Lee-Yang-Par [75] gradient corrected functional for correlation with Becke's three-parameter hybrid functional for exchange. The exact form of Vosko-Wilk-Nusair (VWN) [76] correlation potential corresponding to a fit to the Ceperley-Alder Monte Carlo simulation data is used for the correlation correction. The B3LYP functional in CRYSTAL takes the following explicit form:

$$E_{xc}^{B3LYP} = (1-A)*(E_x^{LDA} + B*E_x^{BECKE}) + A*E_x^{HF} + (1-C)*(E_c^{VWN}) + C*E_C^{LYP}. \quad 2.55$$

A, *B*, and *C* represents the HYBRID and the NONLOCAL part in the input [69, 70], which takes the values of 20 for the HYBRID, and 0.91 and 0.81 for the NONLOCAL parameters for the pure B3LYP functional. For the use of B1-WC hybrid functional we have used WC and PBE functionals for the nonlocal exchange and correlation parts, respectively with parameter values of 16 for HYBRID and 1, 1 for NONLOCAL.

2.3.7.3 Geometry optimization

The optimization of the geometry of the cell parameters as well as the fractional coordinates is performed by using the analytical HF/DFT energy gradients [77]. The optimization algorithm evaluates the gradients each time the energy is computed and the second derivative matrix is updated by employing the gradients. At each step, a one dimensional minimization using a quadratic polynomial is carried out, followed by an n-dimensional search using the hessian matrix. The *Broyden-Fletcher-Goldfarb-Shanno* (BFGS) algorithm is used for Hessian updating [78-81]. The gradients and the estimated nuclear displacements for the next step are evaluated, and convergence is tested with reference to the root mean square (RMS) value of both the gradients (G_{rms}) and the estimated nuclear displacements (X_{rms}) as well as on the absolute value of their largest component, denoted as $G_{\max}$ and $X_{\max}$, respectively [69, 70]. Optimization is considered as complete when the values of these four parameters all simultaneously below the defined thresholds given at the input.

2.3.7.4 Vibrational frequency at Γ-point

The calculation of the vibrational spectra begins with the evaluation of the energy first derivative with respect to the atomic positions $v_i = \partial V / \partial u_j$, analytically for all u_j coordinates, while second derivatives at $\mathbf{u} = 0$ are calculated numerically using a two-point formula (N = 2)

$$\left[\frac{\partial v_j}{\partial u_i}\right] \approx \frac{v_i(0,.....,u_i,0,...)}{u_i}. \qquad 2.56$$

Or a three point formula (N=3) to improve the numerical calculation of the second derivatives:

$$\left[\frac{\partial v_j}{\partial u_i}\right]_0 \approx \frac{v_i(0,.....,u_i,0,...) - v_j(0,.....,-u_i,0,...)}{2u_i}. \qquad 2.57$$

The infinite nature of the crystalline system imposes the use of translational invariance to keep the size of the matrices finite by using the basis of generalized coordinate $q_i(\mathbf{k})$ and permits to block-factorize the vibrational problem into a set of *3N* dimensional problem (one for each **k** in the BZ), where N is the number of atoms in the cell. The **k**-th block of the **k**-factorized weighted hessian matrix will take the form:

$$W_{ij}(\mathbf{k}) = \sum_{\mathbf{G}} \exp[i\mathbf{k}\cdot\mathbf{G}] \frac{H_{ij}^{\mathbf{0G}}}{\sqrt{M_i M_j}}, \qquad 2.58$$

where H_{ij}^{0G} is the second derivative of $V(\mathbf{x})$ at equilibrium with respect to atom i in cell **0** and atom j in cell **G.** At the special point $\Gamma = (0,0,0)$, where the above equation reduces to:

$$W_{ij}(0) = \sum_{\mathbf{G}} \frac{H_{ij}^{\mathbf{0G}}}{\sqrt{M_i M_j}} \qquad 2.59$$

A set of *3N+1* SCF calculations of the unit cell are performed at the equilibrium geometry and incrementing each of the 3N nuclear coordinates in turn by *u* (Effective use of symmetry drastically reduces the number of calculations to be done). The strength of the n^{th} oscillator, f_n, is defined as:

$$f_{n,ij} = \frac{4\text{®}}{\Omega}\frac{\bar{Z}_{n,i}\bar{Z}_{n,j}}{\text{¬}_n^2}, \qquad 2.60$$

Where Ω is the unit cell volume, *i* and *j* indicate the three Cartesian components, ¬_n is the frequency of the n^{th} mode and,

$$\bar{Z}_{n,i} = \sum_{A,j} \mathbf{t}_{n,Aj} Z^{*}_{A,ij} \frac{1}{\sqrt{M_A}}. \qquad 2.61$$

$Z^{*}_{A,ij}$ is the Born effective charge tensor associated with atom A and are evaluated using a Berry phase approach as we shall see soon; and $\mathbf{t}_{n,Aj}$ is an element of the eigenvector matrix T of the mass weighted Hessian matrix W. The ionic components to the static dielectric tensor $\text{£}_{0,ij}$ are evaluated as the sum of the oscillator strengths as $F_{ij} = \sum_n f_{n,ij}$. The IR-intensity I_n of the ¬_n vibrational mode is related to the oscillator strength as:

$$I_n(\mathrm{kJ\,mol^{-1}}) = \frac{\text{®}}{3}\frac{N_A}{c^2} d_n \sum_j \left|\bar{Z}_{n,j}\right|^2 = \frac{N_A V \text{¬}_n^2 d_n}{12c^2}\sum_j f_{n,j}. \qquad 2.62$$

Where in d_n is the degeneracy of the n^{th} mode and N_A is the Avogadro constant. Obtaining the frequencies at **k** points other than Γ (phonon dispersion) would need a supercell. In the case of ionic compounds, the long range Coulomb effects due to the coherent displacement of the atomic nuclei are neglected as a consequence of imposing periodic boundary conditions. Therefore the $W_{ij}(0)$ has to be corrected for obtaining the longitudinal optical modes. This additional term depends on the electronic contribution to the dielectric tensor and the Born effective charge tensor, Z^{*}_{A}, associated to atom A. The electronic high frequency components (clamped nuclei), $\text{£}_{\infty,ij}$ are calculated through the Coupled Perturbed Kohn-Sham (Hartree-

Fock) CPKS/HF scheme [82-85]. The Born effective charge tensor elements are defined as the first derivative of the dipole moments along the i^{th} direction, $«_i$ with respect to the displacement of atom A, along the j direction u_{ij} as $Z^*_{A,ij} = \frac{\partial «_j}{\partial u_{ij}}$. In fact, the dipole moment is ill defined in the case of infinite systems but fortunately the Berry phase approach (see below 2.3.7.5) can be successfully used for the evaluation of the tensor elements. In the present approach, the Born effective charge tensor $Z^*_{ij}(A)$ associated with the atoms of the A^{th} sub-lattice is defined as:

$$Z^*_{ij}(A) = Z_A + (\Omega / e)\left.\frac{\partial P_i^{(el)}}{\partial u_{Aj}}\right|_{\text{E=0}}, \qquad 2.63$$

where Z_A is the charge associated with the nuclei of the sub-lattice, Ω is the volume of the unit cell, e is the electronic charge, and $P_i^{(el)}$ is the i^{th} Cartesian component of the electronic part of the macroscopic polarization induced as a result of the displacement of the sub-lattice in the j^{th} Cartesian direction u_{Aj}. For a small Δu_{Aj}, one assumes $\partial P_i^{(el)} / \partial u_{Aj} |_{E=0} = \Delta P_i^{(el)} / \Delta u_{Aj}$, and the change in polarization $\Delta P_i^{(el)}$ is calculated using an approach proposed by Resta [86] as:

$$\Delta \mathbf{P}_{el} = \mathbf{P}_{el}^{(1)} - \mathbf{P}_{el}^{(0)}, \qquad 2.64$$

wherein $\mathbf{P}_{el}^{(0)}$ and $\mathrm{P}_{el}^{(1)}$ denotes the electronic part of the macroscopic polarization, of the system for its initial $(ª = 0)$ and final $(ª = 1)$ states characterized by the adiabatic symmetry breaking transformation of the lattice characterized by the parameter ª. The ª have been obtained from a finite difference of polarizations as various sub-lattice displacements (Δu_{Aj}) with the electronic part of the polarization is calculated using the Berry phase approach as formulated by King-Smith and Vanderbilt [87].

2.3.7.5 The Berry phase approach

For a periodic crystal, the electronic contribution of the n^{th} band to the Berry phase along the reciprocal-lattice vector b_l can be written as [86, 88]:

$$¤^{(¶)}_{n,l} = \frac{1}{V_{BZ}} \int d^3k \left\langle u_n^{¶}(\mathbf{k}) \right| - i\mathbf{b}_l.\nabla\mathbf{k} \left| u_n^{¶}(\mathbf{k}) \right\rangle, \qquad 2.65$$

Where V_{BZ} is the first Brillouin-zone volume and $u_n^{(\kappa)} = e^{i\mathbf{k.r}}\psi_n^{(\kappa)}(\mathbf{k.r})$, the Bloch function $\psi_n^{(\kappa)}(\mathbf{k})$ are the eigenvectors of the one-electron ground-state Hamiltonian referring to the nuclear and cell configuration κ.

2.3.7.6 The finite field (FF) method

In the finite filed method a static electric field F_0 is introduced into the Fock or Kohn-Sham operator results in an additional perturbed Hamiltonian corresponding to the electric-dipole interaction into the unperturbed Hamiltonian as shown in Eq. 2.66:

$$\hat{H} = \hat{H}_0 + \hat{H}_1(F_0). \tag{2.66}$$

Correspondingly, a perturbed wave function and charge density can be obtained. Then, a response field can be obtained from the perturbed charge density using Poisson's equations. In 3D crystals, a periodic square wave electric field (triangular potential) is applied using a supercell (say N cells in z-direction) approach, in which first N/2 cells are in the positive field and the later N/2 cells are in the negative field. The N cells are then repeated in the z-direction to maintain the periodicity. The corresponding triangular electric potential is then developed in a Fourier series:

$$\hat{H}_1^{\pm}(F_z) = U(z) = -qF_0 \times f^{\pm}(z). \tag{2.67}$$

Here the f^+ or the f^- function is chosen according to the symmetry of the supercell. For the evaluation of the response field, first the charge density obtained from the SCF process is averaged with respect to the infinite plane orthogonal to the field. In the Fourier representation, this averaged charge density takes the form:

$$\bar{\rho}(z) = \frac{1}{V}\sum_{l=-\infty}^{+\infty} F_{0,0,l}\, e^{i\frac{2\pi lz}{C}}. \tag{2.68}$$

Here C is the supercell size and $F_{0,0,l}$ are the structure factors. $\bar{\rho}$ is then averaged with respect to the **z** coordinate,

$$\bar{\bar{\rho}}(z) = \frac{1}{V}\sum_{l=-\infty}^{+\infty} F_{0,0,l} \sin c\left(l\pi \frac{\Delta z}{C} \right) e^{i\frac{2\pi lz}{C}}. \tag{2.69}$$

By applying Poisson's equation, the response macroscopic field $\bar{\bar{F}}$ can be deduced as:

$$\bar{\bar{F}}(z) = \frac{-8\pi}{V}\sum_{l=-1}^{+\infty}\left[F^{R}_{0,0,l}\,\frac{\sin(\frac{2\pi lz}{C})}{\frac{2\pi l}{C}} - F^{I}_{0,0,l}\,\frac{\cos(\frac{2\pi lz}{C})}{\frac{2\pi l}{C}}\right]\operatorname{sinc}\left(l\pi\frac{\Delta z}{C}\right). \qquad 2.70$$

2.3.7.7 Reciprocal space integration

As we saw in section 2.3.6, in periodic structures the crystalline orbitals are BFs and are evaluated in the **k**-space. In CR09 the sampling of **k**-points are carried out according to *Pack-Monkhorst scheme* [89]. According to this scheme, in 3D crystals the sampling points {**k**} belongs to a lattice called *Monkhorst net* with basis vectors $\mathbf{b}_1/s_1$, $\mathbf{b_2}/s_2$, $\mathbf{b_3}/s_3$, where $\mathbf{b_1}$, $\mathbf{b_2}$, and $\mathbf{b_3}$ are the ordinary lattice vectors and S_1, S_2 and S_3 are integer shrinking factors given as IS1, IS2, and IS3 in the input. In the Pack-Monkhorst scheme only points belonging to the irreducible part of the Brillouin zone (IBZ) are considered, with associated geometrical weights w_i. In the case of conductors an additional *Gilat shrinking factor* ISP (ISP1, ISP2, and ISP3) defining a much denser net (*Gilat net*) comes into play. The BFs associated with each different **k**-points (in the Monkhorst net) in the first Brillouin zone belongs to irreducible representations of the group of one electron Hamiltonians $\hat{H}$. It is then possible to factorize the solution of HF or KS equations into separate parts for each **k** as follows:

- Consider the *p* BFs, $\varphi_\mu(\mathbf{r},\mathbf{k})$ associated with a particular **k**
- Calculate the matrix elements: $H^{\mathbf{k}}_{\mu\nu} = \langle \varphi^{\mathbf{k}}_\mu | \hat{H} | \varphi^{\mathbf{k}}_\nu \rangle$ and $S^{\mathbf{k}}_{\mu\nu} = \langle \varphi^{\mathbf{k}}_\mu | \varphi^{\mathbf{k}}_\nu \rangle$
- Solve the $p \times p$ matrix equation:

$$H^{\mathbf{k}}C^{\mathbf{k}} = S^{\mathbf{k}}C^{\mathbf{k}}E^{\mathbf{k}}. \qquad 2.71$$

Here the diagonal matrix $E^{\mathbf{k}}$ contains the eigenvalues $\varepsilon^{\mathbf{k}}_i$, and the matrix $C^{\mathbf{k}}$ contains the coefficients of the crystalline orbitals:

$$\psi_i(\mathbf{r};\mathbf{k}) = \sum_{\mu=1}^{p} c^{\mathbf{k}}_{\mu i}\varphi_\mu(\mathbf{r};\mathbf{k}). \qquad 2.72$$

The above procedure should be performed on the complete set of **k** points in the first Brillouin Zone, so as to determine the complete set of COs, the precision of which is granted by the BS adopted and the computational parameters adopted. Then, from the knowledge of eigenvalues and eigenfunctions at this sample **k** points, one can obtain the values of very important quantities like number of states below a certain energy, *i*(*e*) and the integrated density of states, *I*(*e*) as:

$$i(e) = 2V_{BZ}^{-1}\sum_i \int_{BZ} d\mathbf{k}\,\theta(e-\varepsilon_i^{\mathbf{k}}), \qquad 2.73$$

$$I_{\mu\nu}^{T}(e) = 2V_{BZ}^{-1}\sum_i \int_{BZ} d\mathbf{k}\,c_{\mu i}^{\mathbf{k}*}c_{\nu i}^{\mathbf{k}}e^{i\mathbf{k}.\mathbf{T}}\theta(e-\varepsilon_i^{\mathbf{k}}). \qquad 2.74$$

The step function included $(\theta(e-\varepsilon_i^{\mathbf{k}}))$ in the integrand ensures that only orbitals of energy less than *e* are included. The step function takes the value 1 if $\varepsilon_i^{\mathbf{k}}$ is less than *e*, else the function vanishes. Once we know *i(e)* we can extract the value of Fermi energy (e_F) by imposing the condition $i(e_F)=2n$ by requiring there are exactly *2n* spin orbitals per cell with energy less than e_F. The value of *I(e)* at Fermi energy, e_F give the *P* matrix [$P=I\,(e_F)$].

2.3.7.8 Mulliken population analysis

The probability of finding one electron in the position $\mathbf{r}$, the electron density $\rho(\mathbf{r})$, is one of the essential quantities required for the characterization of the electronic properties of the system studied in coordinate space. By analyzing the electron density then it is possible to extract, the chemical features of the system such as type and nature of bonds. One of the widely used methods for such analysis is the Mulliken population analysis (MPOP). It uses the matrix representation of the electron density in the local basis function formulation:

$$P_{pq}^{\mathbf{g}} = \int_{BZ}\sum_l n_l c_{pl}(\mathbf{k})c_{ql}^{*}(\mathbf{k})e^{i\mathbf{k}.\mathbf{g}}d\mathbf{k}, \qquad 2.75$$

In MPOP, by exploiting the localization of the basis functions, and the atomic orbitals χ, the electron density is partitioned into atomic (ionic), bond and single orbital contributions. In the MPOP method a new matrix $M_{pq}^{\mathbf{g}}$ is defined as follows:

$$M_{pq}^{\mathbf{g}} = P_{pq}^{\mathbf{g}}\cdot S_{pq}^{\mathbf{g}}. \qquad 2.76$$

The electrons described by the matrix element $P_{pq}^{\mathbf{g}}$ are attributed to the atoms on which the basis functions *p* and *q* are centered and are equally shared among the two atoms on which p and q belong to. Under this formalism, the electronic charge attribute to the p^{th} basis function is simply:

$$Q_p = \sum_{\mathbf{g},q} M_{pq}^{\mathbf{g}}. \tag{2.77}$$

By summing the orbital charge of all the atomic charges in the basis set the charge attributed to Nth atom can be obtained as:

$$Q_N = \sum_{p \in N} Q_p. \tag{2.78}$$

A bond charge between atoms N and N′ is obtained by summing the value of all the off-diagonal elements $M_{pq}^{\mathbf{g}}$ in which one of the atomic orbitals belongs to atom N and the other belongs to N′:

$$Q_{NN'} = \sum_{p \in N, q \in N'} M_{pq} + \sum_{p \in N', q \in N} M_{pq} = 2 \sum_{p \in N, q \in N'} M_{pq}. \tag{2.79}$$

By comparing the value of Q_N with a formal electronic charge one can deduce information about the ionicity and formal charge of the atom N in the crystalline environment.

2.3.7.9 Band-structure and density of states

Band structure analysis can provide a better understanding of the conductivity and the chemistry of the crystal. The band structure plots represent the energy solutions along several representative paths in the reciprocal space, usually along the paths connecting the high symmetric points, where often the energy minima and maxima fall. The nature of the interactions can be understood by examining the atomic composition of the eigenvalues and the energy dispersion of the eigenvectors in reciprocal space. The shape of the band plots itself give a general idea about the nature of the bonding. For instance, the more flat the band, the higher the ionic nature and materials with wide bands indicate covalent type bonding. The strength of such covalent bonds entirely depends on the band width. The number of bands increases with the number of basis functions in the unit cell. As the size and the complexity of the system changes the number of bands also increases and it becomes extremely difficult to follow individual bands and predict the properties. Alternatively, a convenient way for dealing with such complex systems is the density of states (DOS). DOS can be obtained by integrating the band structure over the whole of the reciprocal space and gives information on the number of energy levels available for the system as a function of energy. The DOS can be further decomposed into partial density of states (PDOS) according to a Mulliken partition scheme by projecting the contribution of a selected set of atoms or atomic orbitals to the eigenstate at each energy. From the resulting PDOS equation one can define both orbital N_p(e) and atomic N_A(e) values as follows:

$$N_p(e) = V_{BZ}^{-1} \sum_{q,l,\mathbf{g}} \int_{BZ} n_l(\mathbf{k}) S_{pq}(\mathbf{k}) c_{pl}(\mathbf{k}) c_{ql}^{*}(\mathbf{k}) e^{i\mathbf{k}\cdot\mathbf{g}} \text{¢}[e - e_l(\mathbf{k}) d\mathbf{k} \tag{2.80}$$

$$\begin{gathered} N_A(e) = \sum_{p \in A} N_p(e), \\ N_{tot}(e) = \sum_{A} N_A(e). \end{gathered} \tag{2.81}$$

2.4 Visualization of graphics

Manipulations and visualizations of structures were done by *XCrySDen* [90] and VESTA [91] software packages. Rendering of vector graphics was done with INKSCAPE [92] in combination with gnuplot [93].

3 ELECTRONIC PROPERTIES OF TERNARY FE_2O_3-CR_2O_3-AL_2O_3 CORUNDUM SOLID SOLUTIONS

3.1 Introduction

Transition metal oxides are known to be ideal for photocatalytic applications since they show relatively high stability due to the presence of O-2*p* energy levels in the top of the valence bands. For instance, TiO_2 [94] and WO_3 [95] are extensively studied ever since the first demonstration of *Honda-Fujishima effect*. Unfortunately, these materials are transparent to a major portion of the incident solar light due to their large band gap. This limits the maximum possible STH (solar to hydrogen) conversion efficiency of TiO_2 and WO_3 to 3.4% and 5% respectively [22, 34]. On the other hand, because of the low cost, low band gap (~2.2 eV), stability, nontoxicity, and abundance, α-Fe_2O_3 (hematite) is considered as a promising material with potential to convert 16% of solar energy into hydrogen [34, 96]. However, the reported experimental STH conversion efficiency of α-Fe_2O_3 is too low (ca. 2%) [97] due to its extremely poor charge transport properties such as poor majority carrier conductivity and low diffusion length (ca. 2-4 nm) for minority charge carriers. Besides the charge transport, relatively low absorption coefficient, a too low conduction band level with respect to the proton reduction potential, and a relatively large over potential needed for the water oxidation also remains as a drawback. The handicap with respect to the potentials can be addressed by a photovoltaic or a photocathode in tandem [98, 99]. However, the charge transport properties still have to be improved for an efficient conversion of solar energy to hydrogen on a global scale.

A number of studies have been undertaken both experimentally and theoretically [100] in order to explore the right pathway for overcoming these drawbacks. There are earlier reports on the improvement of the electronic properties of hematite by introducing transition metal cations and aluminium [100-103]. Furthermore, the corundum structured Cr_2O_3 (eskolaite) has not been studied yet on the perspective of photocatalysis. The dark green color of eskolaite is expected to be very beneficial in the field of visible light driven photocatalysis. For example, Zhang *et al*. [104] have demonstrated that Cr_2O_3 loaded TiO_2 nanotubes (TNTs) has much higher visible light driven photocatalytic hydrogen production activity by splitting water, than that of pure TNTs. Moreover, it is well known that the presence of Cr_2O_3 along with Al_2O_3 increases the carrier life time [105] dramatically in ruby laser. Both Cr_2O_3 and Al_2O_3 are amphoteric and are widely used as catalysts in wide area of science. These interesting features of Cr_2O_3 and Al_2O_3 together with the capabilities of Fe_2O_3 could result in an efficient solar to hydrogen energy conversion.

The research on Fe_2O_3 [106-109], Cr_2O_3 [110, 111] and Al_2O_3 [112-117] compounds that all crystallize in corundum structure has got a long history. The binary solid solutions of Fe_2O_3, Cr_2O_3 and Al_2O_3 have long been studied due to their industrial and catalytic applications. For instance, the Fe_2O_3-Cr_2O_3 mixed oxide system is considered as a good candidate for catalysis in a wide range of processes [118-120] especially in the high temperature water gas shift reaction [121], dehydration of ethyl benzene to styrene [122], oxidative dehydrogenation of butene to butadiene [123], etc. Recently the rich functionality of Fe_2O_3-Al_2O_3 mixed oxide as a magnetoelectrics is reported and therefore it has been subjected to an extensive theoretical and experimental investigation [124-127]. It is also reported that the addition of Al oxide improves the morphological stability and the attrition resistance of catalysts [128].

Earlier attempts in the synthesis of Fe_2O_3-Cr_2O_3-Al_2O_3 mixed oxide ternary systems [129] are interesting even though there were no reports on the characterization of the electronic properties. Due to the experimental difficulties involved with the synthesis and characterization of these ternary corundum compounds, we have performed an intensive and systematic theoretical study on the structural, electronic and magnetic properties of Fe-Cr-Al oxide ternary systems for photocatalytic applications within the framework of DFT. The thorough analysis of twelve different compositions within the corundum homogeneity range is carried out and the results are presented here. The rest of the chapter is organized as follows: first we present the computational parameters employed for the present study and later the structural, electronic and magnetic properties are discussed. A conclusion on the general findings is given at the end of the chapter.

3.2 Theoretical methods

3.2.1 Computational parameters

The parallel version of CR09 [69, 70] program installed in the Pablo supercomputer (PowerPC cluster) in Malaga has been used for this part of the study. Electronic exchange and correlation has been taken into account at the B3LYP level of theory [63, 66]. The performance of the B3LYP hybrid functional in describing the structural, electronic and magnetic properties of a wide range of materials including hematite [106, 119, 130] has been previously reported [131]. In order to ensure high-quality calculations the triple zeta basis sets are employed. Triple zeta quality GTO basis sets are taken from the literature and they have the same structure [Fe, Cr; 8-6411(41d),Al; 8-511(1d),O; 8-411(1d)][2], as reported elsewhere [119, 132]. The complete basis set is given in Appendix.

All calculations were performed using tight tolerance factors for the Coulomb and exchange series evaluation (ITOL values). The ITOL*n* (*n*=1, 2, 3, 4, 5) tolerance parameters were set to 7, 7, 7, 7, and 14, respectively. The SCF convergence threshold was set to 10^{-9} hartree. The Brillouin zone integrations were performed using the (4×4×4) Pack Monkhorst k-mesh for the SCF calculations and (8×8×8) for the electronic properties calculations for the 30 atom supercell, and was found to provide sufficient precision in the calculation of the ground state electronic properties and total energy convergence. The DFT exchange-correlation contributions were evaluated by numerical integration using a comparatively large internally predefined grid (corresponds to a pruned grid with 75 radial and 974 angular points).

Geometry optimization was performed by use of analytical energy gradients with respect to the atomic coordinates and the unit cell parameters (see section 2.3.7.3 for details). The spin polarized electronic structure calculations for the

---

[2] The first figures show an *s* contraction and the later shows *sp* contractions. Th figures represented in parantheses shows *d* contraction.

ternary corundum oxides and the end members were carried out within a supercell approach. A large series of runs are performed in order to check the configurational effect that might arise due to a large number of possible permutations.

3.3 Results and discussion

3.3.1 Structural properties

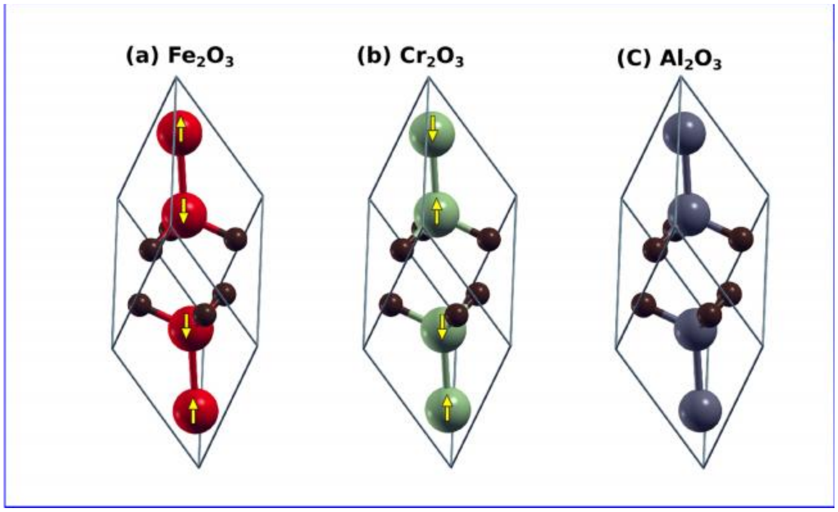

Figure 3-1: Rhombohedral unit cell of a) Fe_2O_3, b) Cr_2O_3, and c) Al_2O_3. The spins up and down states are represented by yellow arrows. Coloring of the ions are as follows Fe (red), Cr (Green), Al (blue) and O (grey).

For the present study the lattice parameters and the cell positions of the end members are taken from the literature [109, 115]. They were re-optimized by considering the known antiferromagnetic setting for Fe_2O_3 and Cr_2O_3, and nonmagnetic for Al_2O_3, with respect to the B3LYP functional. The rhombohedral primitive cell of the end members are shown in Fig. 3-1, with the ground state magnetic setting. To model the complex ternary corundum structure, we have created a larger hexagonal super cell of hematite with 30 atoms in the unit cell (with 12-Fe and 18-O atoms) along the **c**-axis as shown in Fig. 3-2. The cation composition of the model structure is varied by the successive substitution of Al and Cr atom into the Fe-sub lattice position within the ground state AFM configuration. A full geometry relaxation (cell parameters and lattice coordinates) is carried out for all the compositions for minimizing the external pressure induced by the substitution. Since we are interested in the Fe_2O_3 rich range of solid solutions, our modeled compositions always contained more Fe than Cr and Al. For that we followed a strategy for selecting the number of cations (*n*) in the supercell as follows; *n*Fe ≥ *n*Cr ≥ *n*Al. This results in twelve different compositions within the homogeneity range. The minimum energy configuration of all the twelve compositions optimized with the B3LYP functional is presented in Fig. 3-3.

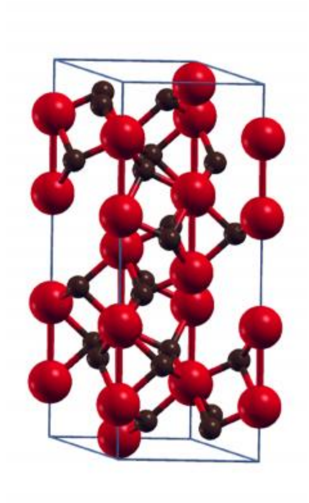

Figure 3-2: Hexagonal cell of Fe_2O_3 with 30 atoms in the asymmetric unit. The colorings of ions are done according to Fig. 3-1.

The investigation of configurational effects in solid solutions within a supercell approach using computer simulations, however, possess the problem of the large number of possible configurations that can exist for a particular supercell, especially when spin polarized calculations are demanded. In order to avoid the ambiguity in selecting the composition with right spin setting we have performed a series of run for the configurational checking and ensured the thermodynamic stability of the studied compounds. The formation energies of all the studied compositions are calculated by subtracting the total energy of the end members from the total energy of the ternary system.

$$\Delta H^{f} = E^{(Fe-Cr-Al)O_3} - (xFe_2O_3 + yCr_2O_3 + zAl_2O_3);\ x + y + z = 2 \qquad 3.1$$

Where, $E^{(Fe-Cr-Al)O_3}$ is the energy of the ternary system and x, y, and z are the percentage of Fe_2O_3, Cr_2O_3, Al_2O_3, respectively in the ternary oxide system. We found that the formation energy per formula unit is very small but positive (endothermic); even the maximum energy calculated is only 200 meV. This slightly positive, rather negligible energy value comes from the reference energy i.e., total energy of the end members.

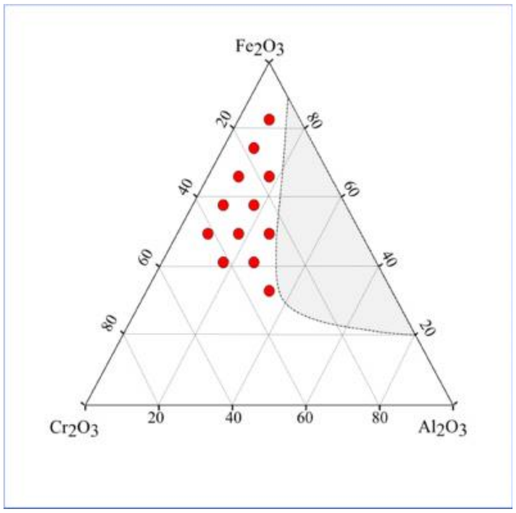

Figure 3-3: Solubility limit (non-colored) and the composition spectra of the studied 12 Fe-Cr-Al mixed oxides with corundum structure. The solubility limit is taken from the literature [133]

The optimized lattice parameters, volume, and c/a ratios of the most stable configuration within each composition are reported in Table 3-I. From our calculations we found that for the ternary system, minimum energy configurations are those in which all the cations are segregated as shown in Fig. 3-4. This is in agreement with the previous studies on the thermodynamic stability of Fe_2O_3-Cr_2O_3 binary oxide systems; see Benny *et al.* [118]. However, the energy difference (per formula unit) between different clustered configurations and the randomly substituted configurations within each composition is of the order of ~10 meV, which is so small that can be neglected within the computational accuracy. Neither the unit cell parameters nor the volume significantly change by changing the position of the substituted atoms. We are aware that in this kind of complex system it is not possible to experimentally control the cation site occupancy, which would to a large extend be random.

As evidenced from Table 3-I, the lattice parameters of Fe_2O_3, Cr_2O_3 and Al_2O_3 sesquioxides are well reproduced compared to the experimental results [117, 134, 135] with a maximum absolute error of 0.06 Å and 0.16 Å for the **a** and **c** lattice parameters, respectively. This rather small over estimation is quite usual for the B3LYP functional. The lattice parameters of the ternary systems show a general trend of decrease with the increase in the Al content. This is expected due to the large size difference between Al and Fe atoms. The symmetry analysis on the theoretically modeled ternary systems indicates that for the entire composition range the ternary system retains the corundum, $R\overline{3}c$, symmetry. The c/a ratio for all the compositions remains nearly at 2.73±0.01, which further corroborates the corundum symmetry. Due to the size difference in Fe and Al cations, an increase in the aluminum content considerably decreases the volume as shown in Fig. 3-5, resulting in an internal strain similar to the case of Fe_2O_3-Al_2O_3 binary systems.

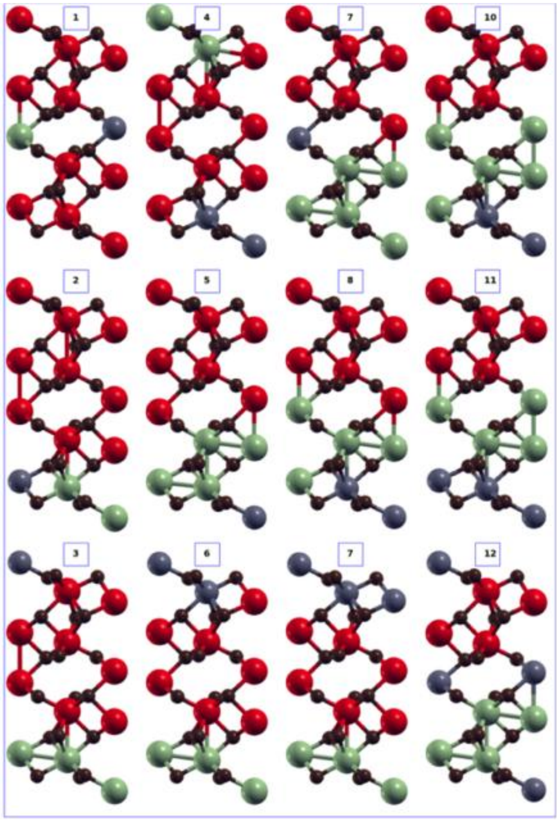

Figure 3-4: Asymmetric unit representation of the optimized structure of the twelve studied compositions from the corundum system. Coloring has been done according to Fig. 3-1. The numbering of the compositions (blue square boxes) has been done according to Table 3-I.

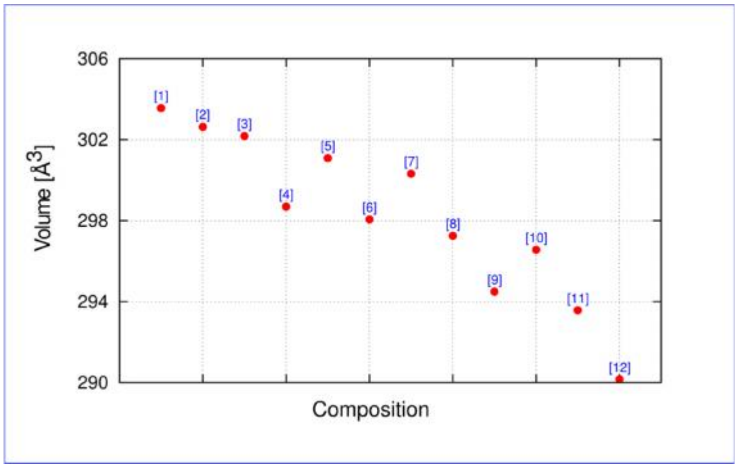

Figure 3-5: Volume of each composition is plotted in numerical order. The compositions are numbered according to Table 3-I.

3.3.2 Structure related charge transport properties

The charge transport properties of hematite are dominated by the small polaron mobility [136, 137] and is well known for its anisotropic behavior in the charge transport along the (001) plane and [001] direction. The conduction in the (001) plane is up to four orders of magnitude faster than the [001] one direction. This can be explained by considering the Hund's rule, i.e., since the Fe atoms are antiferromagnetically coupled along the [001] direction, the hopping of electrons along [001] direction is spin forbidden. In our case the strain induced within the crystal due to the decrease in the volume results in a decrease in the nearest neighbor Fe-Fe distance, especially along the (001) plane. This decrease in the Fe-Fe distance in the (001) plane eventually results in an enhancement of the hopping probability and this will increase the conductivity of the electrons/holes in the (001) plane. This could be further explained in terms of nearest neighbor interaction.

In our case, as we saw before, the inclusion of Al into the Fe lattice results in a reduction in the Fe-Fe distances by nearly 0.05 Å on an average, while the distance to the bridging oxygen is reduces by 0.02Å. As a result of the decrease in this distance, the direct exchange interaction through the bridging oxygen atoms will be enhanced and the electron coupling between the nearest neighbors Fe atoms in the (001) plane will be strengthened due to the extended special mixing of Fe-Fe *d* orbitals. This should favor the electron transfer and would result in increased majority carrier conductivity. This is consistent with the results of Rosso *et al*. [120], i.e., a reduction in the nearest neighbor Fe-Fe distance should facilitate a reduction in the activation energy, and hence an increased electronic coupling. In hematite, the activation energy for holes is three times bigger and hence a higher conductivity for holes can be achieved only at a smaller volume. Thus, our analysis indicates that the inclusion of Al_2O_3 into Fe_2O_3 mainly increases the majority carrier conductivity and is therefore beneficial for photocatalytic applications. However, such enhancement in the charge transport properties would need to be further confirmed by experiments.

Table 3-I: The optimized geometrical parameters, c/a ratio and the volume of 12 ternary compositions and the end member oxides. Relative error is indicated in parenthesis.

No.	System	a(Å)		c(Å)		c/a	V (Å$^{3)}$	
		Calc	Exp	Calc	Exp		Calc	Exp
1	$Fe_{1.666}Cr_{0.166}Al_{0.166}O_3$	5.04		13.80		2.74	303.56	
2	$Fe_{1.50}Cr_{0.333}Al_{0.166}O_3$	5.04		13.78		2.73	302.63	
3	$Fe_{1.333}Cr_{0.500}Al_{0.166}O_3$	5.03		13.80		2.74	302.18	
4	$Fe_{1.333}Cr_{0.333}Al_{0.333}O_3$	5.01		13.72		2.74	298.69	
5	$Fe_{1.166}Cr_{0.666}Al_{0.166}O_3$	5.03		13.72		2.73	301.09	
6	$Fe_{1.166}Cr_{0.500}Al_{0.333}O_3$	5.01		13.70		2.73	298.06	
7	$Fe_{1.00}Cr_{0.833}Al_{0.166}O_3$	5.03		13.72		2.72	300.32	
8	$Fe_{1.00}Cr_{0.666}Al_{0.333}O_3$	5.01		13.67		2.73	297.25	
9	$Fe_{1.00}Cr_{0.500}Al_{0.500}O_3$	4.99		13.68		2.74	294.49	
10	$Fe_{0.833}Cr_{0.833}Al_{0.333}O_3$	5.01		13.64		2.72	296.56	
11	$Fe_{0.833}Cr_{0.666}Al_{0.500}O_3$	4.99		13.62		2.73	293.57	
12	$Fe_{0.666}Cr_{0.666}Al_{0.666}O_3$	4.97		13.58		2.74	290.16	
13	Fe_2O_3	5.06	5.03[a]	13.89	13.74	2.75	307.87	301.76[a]
		(0.59)		(1.1)			(2.02)	
14	Cr_2O_3	5.01	4.95[a]	13.71	13.57	2.74	298.28	287.98[a]
		(1.21)		(1.03)			(3.57)	
15	Al_2O_3	4.79	4.75[b]	13.07	12.98	2.73	260.09	255.89[b]
		(0.84)		(0.69)			(1.64)	

[a]Ref. [109]; [b]Ref. [115]

3.3.3 Electronic properties

We begin the discussion on the electronic properties of the ternary systems by presenting the B3LYP calculated electronic band structure of the end members. The band gap values calculated in the spin up and spin down channel are collected in Table 3-II. As clearly seen from the table, the pure B3LYP overestimates the experimental band gap value of Fe_2O_3 and Cr_2O_3 by nearly ~1eV due to an overestimation of the exchange contribution, which is consistent with earlier reports; see for example Moore *et al.*, [119]. Both the shape and the nature of the bands, on either side of the Fermi level are well reproduced. The band structures of Fe_2O_3, Cr_2O_3, and Al_2O_3 are plotted in Fig. 3-6. The top of the valence band as well as the bottom of the conduction band in the hematite lay along the K-M direction, but are located at different points indicating an indirect band gap nature; it is, however, hard to identify the conduction band minima from the band structure of Fe_2O_3 due to the presence of flat bands, consistent with the presence of strongly localized states, see below. In the case of Cr_2O_3, both the valence band maxima and conduction band minima are located at the **k**-point K, showing a direct band gap. Conversely, in the case of Al_2O_3, both the band edges are located at the gamma point. For a better description of the nature of the bands, in Fig. 3-7, we have plotted the atom projected density of states of all the three end members. The valence band of Fe_2O_3 is contributed by O-2*p* and Fe-3*d* hybridized states with a higher contribution from the O-2*p* states. While the conduction bands are dominated by Fe-3*d* localized orbitals. As seen from the DOS plot, in the conduction band, two narrow Fe-3*d* bands appear; this narrowness of the Fe-3*d* bands substantiates the occurrence of extremely flat bands at the conduction band edge. Unlike in the case of Fe_2O_3, the valence band of Cr_2O_3 is dominated by Cr-3*d* orbitals, indicating that the hybridization with the oxygen 2*p* levels is rather weak. The comparatively less dispersion in the valence band levels are attributed to the domination of Cr-3*d* bands. The conduction band of Cr_2O_3, are again contributed by two separate Cr-3*d* bands but are much wider compared to the Fe-3*d* levels. From the band structure analysis of Fe_2O_3 and Cr_2O_3, thus we could conclude that, Fe_2O_3 is a charge transfer type semiconductor, while Cr_2O_3 shows an intermediate behavior between that of a charge transfer (*p-d*) and Mott-Hubbard type (*d-d*). The band structure of Al_2O_3 is like that of a typical ionic insulator, with highly dispersed bands at both the valence and conduction bands. Another characteristic is that both the bands come from the anion orbitals (2*s* and 2*p*) yielding a very large band gap.

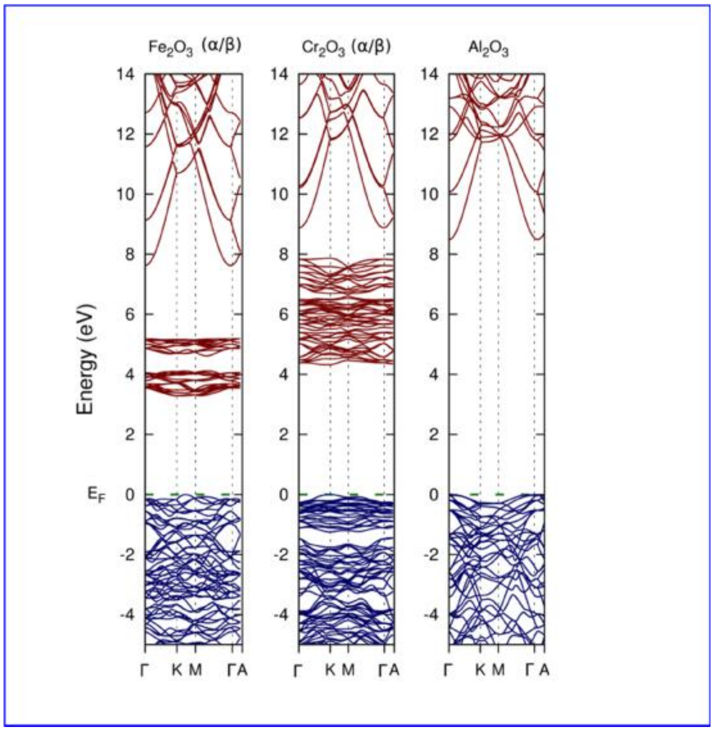

Figure 3-6: Band structure of a) Fe_2O_3 b) Cr_2O_3, c) Al_2O_3. Blue curves represent the valence band and the red curves represent the conduction band. The top of the valence band (green dotted lines) is taken as the reference zero energy. X axis labels shows different high symmetric points in the first Brillouin zone. Valence bands below -5 eV are omitted from the figure for clarity. (α/β) indicates that the band structure is spin polarized. Since both are same in the present case only that in the spin-up (α) channel is plotted.

The calculated electronic band gap for the spin up and spin down channels for all the ternary structures are also collected in Table 3-II. As seen from the Table 3-II, the band gap of the ternary systems is smaller than that of the pure hematite system, especially for systems with higher Cr_2O_3 content. There is a general trend of decrease in the band gap value with an increase in the Cr_2O_3 content. For instance, for compositions (see compositions numbered 5 and 6 in Table 3-II) with 58.3% Fe_2O_3, an increase in the Cr_2O_3 content from 25% to 33.3% causes a decrease of 0.51 and 0.43 eV, respectively in the spin up and spins down channels (c.f. Table 3-II). However, the reduction of band gap value for compositions containing less than 25% Cr_2O_3 is not dramatic. A red shift in the band gap value without affecting the conduction band edge is very useful as it allows capturing more photons in the visible region of the spectra. At the same time, the percentage of Al_2O_3 in the ternary system does not have any direct impact on the electronic band gap value. In addition, as seen from Table 3-II, the calculated band gap of few compositions is direct band gap, which will certainly enhance the absorption coefficient of the ternary compositions especially in the visible spectrum.

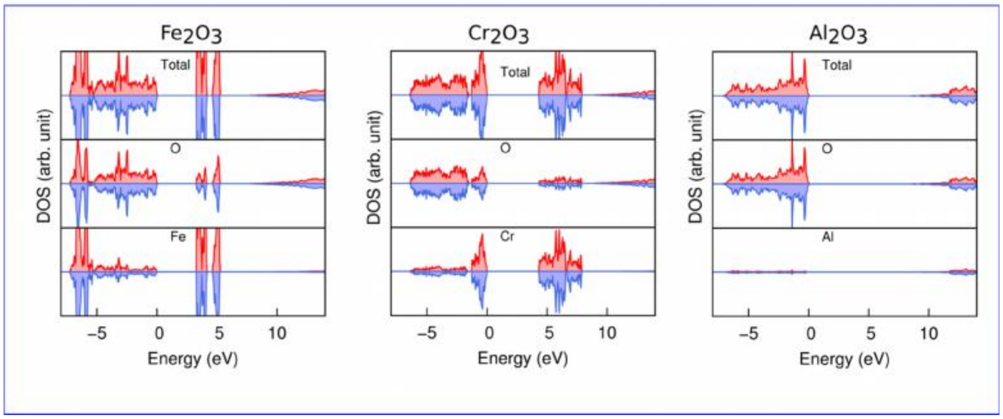

Figure 3-7: Total (T) as well as the orbital projected density of states of a) Fe_2O_3, b) Cr_2O_3 and c) Al_2O_3. The DOS is plotted with arbitrary units. The red portion represents up spin and blue portion represents down spin. The top of the valence band is taken as the zero reference energy.

The total densities of states of all the ternary compositions that have been studied are collected in Fig. 3-8. The inclusion of Cr into the Fe sub lattice in hematite has a direct influence on the band edges. The position of the valence band is shifted upwards for about ca. 0.3 eV compared to Fe_2O_3 for most of the compositions, especially the one with more Cr_2O_3. This is because, before the inclusion of Cr, the valence band edge was predominantly contributed by the O-2*p* levels whereas after the inclusion of Cr into the Fe sub lattice the d^3 state fills t_{2g} levels of Cr-3*d* states and the unoccupied e_g levels will be separated from the t_{2g} levels due to strong crystal field splitting. The highly localized t_{2g} levels fall at the top of the valence band. The more negative and highly localized Cr-3*d* bands drag the O-2*p* orbitals towards the Fermi level due to the tendency to hybridize. This not only reduces the band gap but also increase the valence band width. These two characteristics are very important for photocatalytic efficiency, as in hematite the photogenerated holes are expected to be located at the narrow Fe-3*d* orbitals. If the holes are generated very deep inside the bulk semiconductor an immediate recombination occurs (low hole-diffusion length). In the case of Cr-doped hematite, the calculations indicate an increase in the band width, which should result in a lower recombination rate. This would give much freedom for the holes to migrate. Hence alloying Fe_2O_3 with Cr_2O_3 can be considered as a very promising method also for improving the charge transport kinetics of holes in hematite.

At the same time, the shift in the conduction band minima is gentle since neither Cr nor Al unoccupied levels falls close to the conduction band edge. The observed very small downward shift (positive) might be due to the reduction in the volume. In Fig. 3-8, the shift in the valence and conduction band edges with respect to the pure Fe_2O_3 systems are indicated by drawing reference lines at the energies corresponding to the valence and conduction band edges of pure Fe_2O_3. From Fig 3-8, it is also clear that as the percentage of Fe-decreases (especially below 50%), the width of the conduction band also decreases due to a much denser packing. The decrease in conduction band width reduces the number of available excited states; this is an a priori indication of reduced photocatalytic efficiency. Hence, reducing the percentage of Fe_2O_3 far too low from 50% is not beneficial for the H_2 evolution.

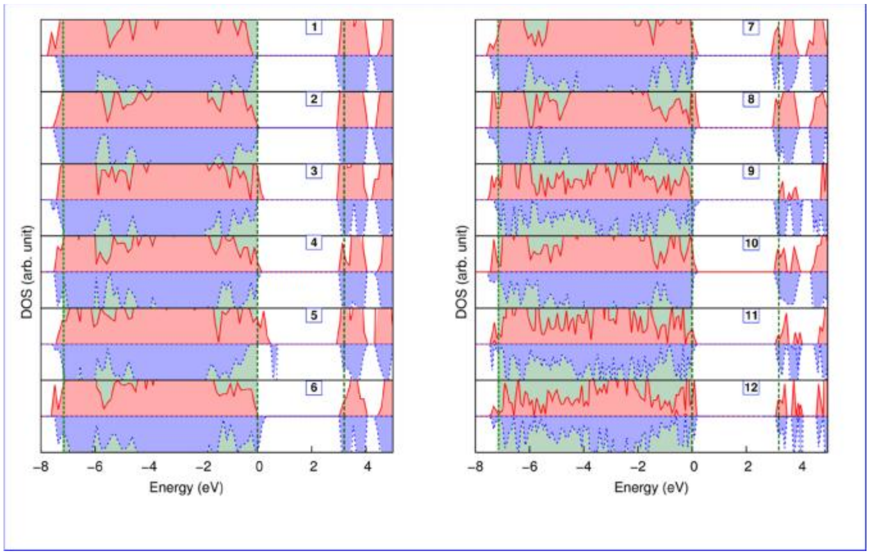

Figure 3-8: Total density of states of all the 12 different ternary oxides. The red and blue colored portions represent up and down spins respectively. The green dashed line at 0 eV represents reference zero energy and which correspond to the top of the valence band of pure Fe_2O_3. The green shaded portion (separated by green dashed lines) represents the width of the valence band of pure Fe_2O_3. The numbers in the blue box represents compositions.

For further interpretation and a deeper analysis, here onwards we will be showing plots corresponding only to three different compositions namely

$Fe_{1.666}Cr_{0.166}Al_{0.166}O_3$ [#1], $Fe_{1.333}Cr_{0.333}Al_{0.333}O_3$ [#4], and $Fe_{0.666}Cr_{0.666}Al_{0.666}O_3$ [#12]. In Fig. 3-9, we have plotted the atom projected density of states of these selected three compositions. Compared to pure Fe_2O_3 it is clear from Fig. 3-9 that the nature of the valence band is modified upon Cr- inclusion. The Cr-3*d* bands are nearly degenerate with the Fe-3*d* bands, but are more negative, i.e., close to the Fermi level. Hence the valence band edge of all the ternary compositions comes from the Cr-3*d* levels. The lower valence bands are an admixture of metal 3*d* (especially Fe-3*d*) orbitals and O-2*p* orbitals.

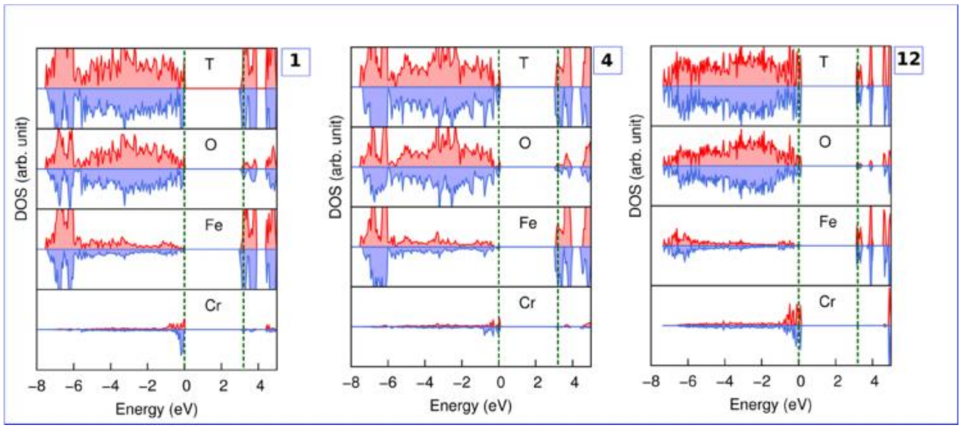

Figure 3-9: Total (T) and atom projected density of states of three selected compositions. The top of the valence band is taken as the zero reference energy. Green dotted lines are drawn at the energy level corresponding to the top of the valence band of pure hematite for reference. The red portion represents the spin up states and the blue portion represents the spin down states. The composition numbers are represented in blue boxes at the top corner of each figure. The numbering of the compositions is according to Table 3-I.

The oxygen 2*p* levels are well hybridized with the metal 3*d* levels. This can be attributed to a reduction in the distance between the bridging oxygen upon inclusion of Al and Cr. At the same time, in the conduction band, the unoccupied Cr-3*d* levels fall well above the Fe-3*d* unoccupied levels and thus the conduction band minima come solely from Fe-3*d* orbitals. This is further clarified by the orbital projected density of states plotted in Fig. 3-10. Thus we could conclude that, the presence of Cr-3*d* orbitals is responsible for the band gap reduction, as it causes an upward shift of the top of the valence band.

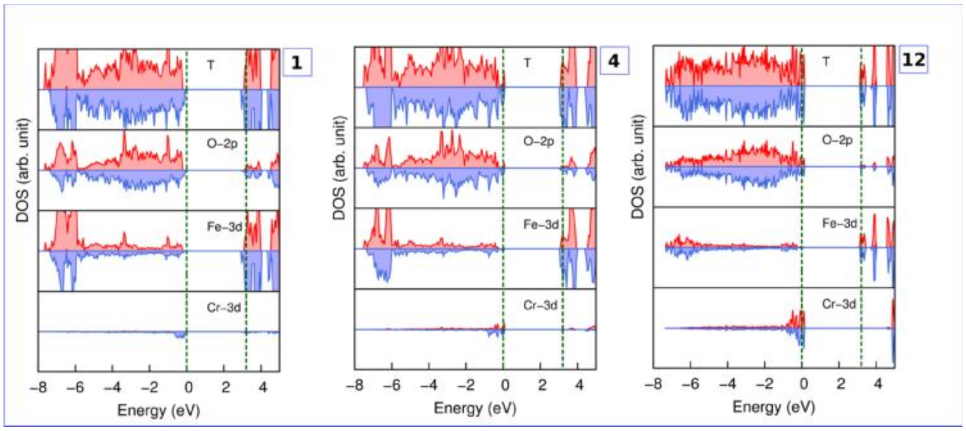

Figure 3-10: Total (T) and orbital projected density of states of three selected compositions. The top of the valence band is taken as the zero reference energy. Green dotted lines are drawn at the energy level corresponding to the top of the valence band of pure hematite for reference. The red portion represents the spin up states and the blue portion represents the spin down states.

Table 3-II: Calculated electronic band gap in the spin up (α-electrons) and in the spin down channel (β-electrons) for the ternary compositions as well as the end members. Absolute error is reported in parenthesis in eV.

#	Composition	Band gap (Spin up) $E_g^{\sim}$ (eV)	Band gap (Spin down) E_g (eV)	Band gap E_g (eV)	Expt
1	$Fe_{1.666}Cr_{0.166}Al_{0.166}O_3$	3.32	3.03	3.03	
2	$Fe_{1.50}Cr_{0.333}Al_{0.166}O_3$	2.98	3.05 (direct)	2.98	
3	$Fe_{1.333}Cr_{0.500}Al_{0.166}O_3$	2.80	3.20	2.80	
4	$Fe_{1.333}Cr_{0.333}Al_{0.333}O_3$	3.07 (direct)	2.96	3.07	
5	$Fe_{1.166}Cr_{0.666}Al_{0.166}O_3$	2.74	2.47	2.47	
6	$Fe_{1.166}Cr_{0.500}Al_{0.333}O_3$	3.25	2.90	2.90	
7	$Fe_{1.00}Cr_{0.833}Al_{0.166}O_3$	2.78 (direct)	2.84	2.78	
8	$Fe_{1.00}Cr_{0.666}Al_{0.333}O_3$	2.75	2.87	2.75	
9	$Fe_{1.00}Cr_{0.500}Al_{0.500}O_3$	3.23 (direct)	2.84	2.84	
10	$Fe_{0.833}Cr_{0.833}Al_{0.33}O_3$	2.93	2.89	2.89	
11	$Fe_{0.833}Cr_{0.666}Al_{0.5}O_3$	3.02	2.94	2.94	
12	$Fe_{0.666}Cr_{0.666}Al_{0.666}O_3$	3.02 (direct)	3.01	3.02	
13	Fe_2O_3	3.28	3.30	3.28 (+1.01)	2.27[a]
14	Cr_2O_3	4.30	4.31	4.30 (+0.90)	3.40[b]
15	Al_2O_3	8.60	8.60	8.60 (+0.6)	8.00[c]

[a]Ref. [134]; [b]Ref. [135]; [c]Ref. [117]

The band structures of the selected compositions are plotted in Fig. 3-11. As mentioned earlier, the valence band of the ternary system shows a strong hybridization of O-*p* and Fe-*d* states in the lower valence band region and thus it shows higher dispersion, although the top lying levels are comparatively flat due to the presence of highly localized Cr-3*d* levels. The localization of the Cr levels at the top of the valence band is clearly visible in the band structure plots. For instance, in Fig. 3-12, the plots for the compositions #4 and #12, two well localized bands can be clearly seen close to the Fermi level. When the Cr_2O_3 content increases these bands become more and more localized and might facilitate the recombination of charge carriers. Unlike the parental Fe_2O_3 band structure as shown in Fig. 3-6a, the conduction bands of the mixed oxide system shows more dispersion (along K-M direction in the Brillouin zone) especially for the systems with higher Al content, due to the reduced volume (Fig. 3-11b, and Fig. 3-11c). A close observation on the conduction band indicates that as the percentage of Cr_2O_3 increases, all the conduction bands become narrower and more and more localized states appear and the bottom of the conduction band splits into two separate levels. The localized bands falls above 4 eV are mainly from the Cr-3*d* orbitals due to much higher crystal field splitting.

For better clarity, the top of the valence band and the bottom of the conduction band, both in alpha and beta channels, for all the compositions are plotted in Fig. 3-12. The higher dispersion in the conduction band is a clear indication of a reduction in the electron effective mass and thereby results in improved majority carrier conductivity. This further corroborates our assumptions on the possibility of strain induced conductivity.[3]

---

[3] The calculation of effective mass at the band edges gave us unreasonable values since at the extreme, the energy values are degenerate (flatness). Hence we were unable to give quantitative information about the conductivity from effective masses.

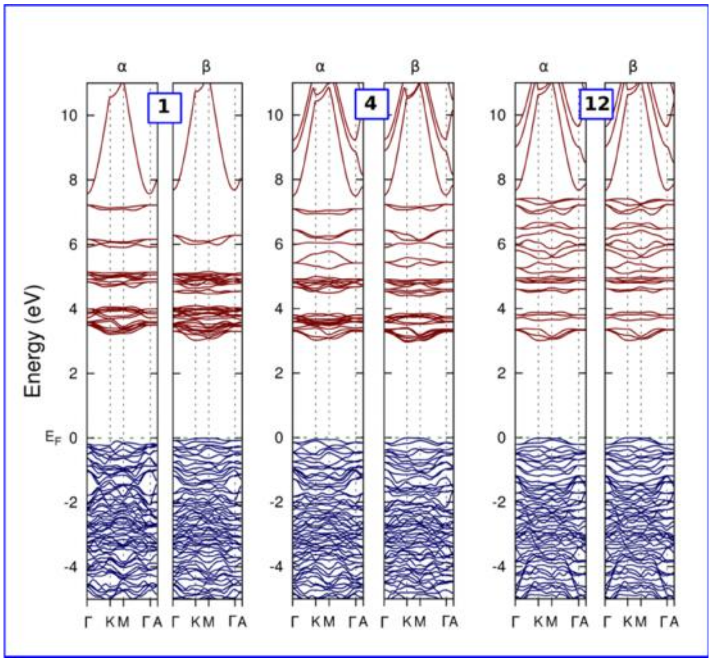

Figure 3-11: The band structure (up and down spin channels) of three selected compositions (For details regarding the numbering of the compositions see Table I). Blue bands represent valence band and the red bands represent conduction band.

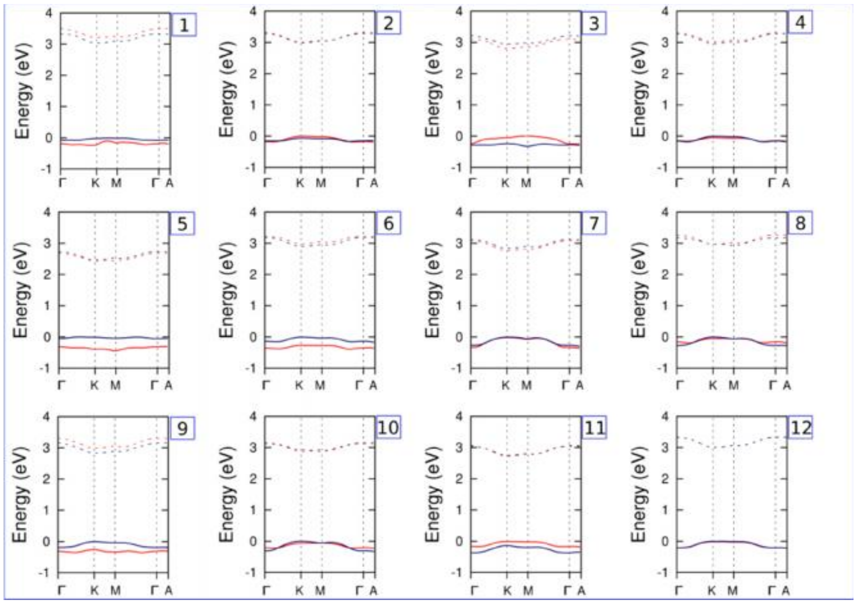

Figure 3-12: The top of the valence band (solid lines) and the bottom of the conduction band (broken lines), for all the compositions are plotted along the high symmetric directions. The compositions are numbered according to Table I. Blue color corresponds to down spin (beta channel) and red line corresponds up spin (alpha channel)

3.3.4 Magnetic properties

Although electrically all the ternary compositions remain insulating, they shows different magnetic behavior. Due to the unequal number of *d* electrons in the 3*d* orbitals of Fe and Cr, only few of the ternary compositions ($Fe_{0.666}Cr_{0.666}Al_{0.666}O_3$,

$Fe_{1.333}Cr_{0.333}Al_{0.333}O_3$, $Fe_{1.00}Cr_{0.666}Al_{0.333}O_3$) remain antiferromagnetic. The rest of the compositions are ferrimagnetic with a net magnetic moment. The nominal sublattice magnetic moment calculated at the Fe, Cr, Al and O sites as well as the total magnetic moment of all the compositions and the end members are given in Table 3-III. The Fe-sublattice magnetic moment is well below the ideal ionic value of $5\mu_B$ for both the end members as well as the ternary compositions. This is due to the hybridization with the oxygen 2*p*-orbitals. The nominal magnetic moment at the Cr site is close to the ideal ionic value of $3\mu_B$ for most of the composition. This supports the strong localization of the Cr-3*d* orbitals due to the crystal field splitting. Due to a strong hybridization with the Fe-3*d* orbitals, the O-sites also show a very small nominal moment. But the nominal moment at the Al site is negligible. Since the characterization of the magnetic properties of the material is not relevant from the photocatalytic applications, a deep analysis on this topic is skipped from the present context.

Table 3-III: Nominal magnetic moment as well as total magnetic moment of all the compositions together with the parental Fe_2O_3 and Cr_2O_3. The units are in Bohr magnetons μ_B.

#	System	μ_{Fe}	μ_{Cr}	μ_{Al}	μ_O	μ_{TOTAL}
1	$Fe_{1.666}Cr_{0.166}Al_{0.166}O_3$	4.22	2.87	0.01	0.08	7.00
2	$Fe_{1.50}Cr_{0.333}Al_{0.166}O_3$	4.21	2.89	0.01	0.07	5.00
3	$Fe_{1.333}Cr_{0.500}Al_{0.166}O_3$	4.21	2.92	0.00	0.08	3.00
4	$Fe_{1.333}Cr_{0.333}Al_{0.333}O_3$	4.21	2.90	0.00	0.06	0.00
5	$Fe_{1.166}Cr_{0.666}Al_{0.166}O_3$	4.21	2.46	0.00	0.06	5.00
6	$Fe_{1.166}Cr_{0.500}Al_{0.333}O_3$	4.21	2.90	0.00	0.06	2.00
7	$Fe_{1.00}Cr_{0.833}Al_{0.166}O_3$	4.21	2.90	0.01	0.06	3.01
8	$Fe_{1.00}Cr_{0.666}Al_{0.333}O_3$	4.21	2.90	0.00	0.06	0.00
9	$Fe_{1.00}Cr_{0.500}Al_{0.500}O_3$	4.21	2.89	0.01	0.07	7.00
10	$Fe_{0.833}Cr_{0.833}Al_{0.33}O_3$	4.21	2.89	0.00	0.06	2.00
11	$Fe_{0.833}Cr_{0.666}Al_{0.5}O_3$	4.21	2.90	0.00	0.06	5.00
12	$Fe_{0.666}Cr_{0.666}Al_{0.666}O_3$	4.21	2.92	0.01	0.08	0.00
13	Fe_2O_3	4.21	-	-	0.00	0.00
14	Cr_2O_3	-	2.92	-	0.00	0.00

3.4 Summary

In this chapter a key insight into the electronic and magnetic properties of a series of hematite based Fe-Cr-Al ternary oxides within the homogeneity range are presented. We observed that all the compositions are stable and they retain the corundum, $R\overline{3}c$, symmetry. The presence of Al_2O_3 is found to decrease the volume of the crystal and this substantially facilitates the charge transfer properties of the majority carriers, while the presence of Cr_2O_3 alters the nature of the valence band. As the percentage of Cr_2O_3 is increased, there is a decrease in the band gap as well as an increase in the band width. An increase in the band width would enhance the charge transfer kinetics of holes. At the same time, an indirect to direct band gap transition is also observed for few compositions. A direct band gap is always beneficial for a better photo response. Observed higher dispersion at the conduction band indicates a reduction of the effective mass of electrons, hence an increased mobility. Thus, as a conclusion we could say that by making a solid solution with Cr_2O_3 and Al_2O_3 several key issues of hematite, mainly charge transport properties of electrons, charge transfer kinetics of holes can be addressed.

4 EFFECT OF ELECTRIC FIELD ON THE STRUCTURAL AND ELECTRONIC PROPERTIES OF ROCK-SALT CRYSTAL STRUCTURE.

4.1 Introduction

The variation of many physical and chemical properties of materials, caused by the application of an electric field, has been investigated to a greater extent within the last few decades [44, 45, 138-146]. In photocatalysis it is attracting an increased interest as it has been proved that the presence of an external electric field enhances the photocatalytic and hydrogen storage properties [44, 45, 147].

In the field of photocatalysis the major factor controlling the light capture is the electronic band gap [7]. Since a large number of semiconductors are excluded from the list of photocatalysts due to their too wide band gap [148], the possibility of tuning the width of the band gap with the external electric field seems to be promising. For this reason, we initiated a series of studies on the band gap variation of wide band gap insulators as well as semiconductors in the presence of the external electric field. Difficulties in experimental characterization of the crystal response in the presence of the extremely high external fields lead us to choose the computational approach within the framework of density functional theory (DFT) [49, 53].

For the sake of definiteness, ease of computation, and to ensure the accuracy of the approach, we begin with a series of wide band gap insulators. Since a large amount of experimental data was available for alkali halides, we have selected first six light alkali halides as prototypical examples, LiF, LiCl, NaF, NaCl, KF, and KCl. Later we extended the approach to two semiconductors, AgCl and AgBr with excellent applications in the field of photochemistry. The rest of the chapter is arranged as follows. The following section provides the general details about the computational tools that we have employed throughout the work presented in this chapter. Later on, structural and electronic properties of alkali halides and silver halides in the presence and the absence of an external static electric field are provided. For better clarity, the results obtained for the both halide families are given in separate parts. A general summary of the present work is provided at the end of the chapter.

4.2 Computational methods

The calculations were performed within the framework of DFT using CRYSTAL program [69, 70] and the local Gaussian-type-orbital (GTO) basis sets. The treatment of exchange and correlation was performed using the well-known hybrid B3LYP functional [63, 66]. It has been shown in a previous section that B3LYP functional reproduces equilibrium geometry, vibrational frequencies, magnetic properties, and electronic band gap in good agreement with the experimental values [106, 131, 149]. In addition to the already mentioned B3LYP, we have also used its two modified variants and the local-density-approximation (LDA). For the modified scheme the percentage of Fock mixing in the B3LYP functional has been reduced to zero and forty. The resulting Hamiltonians are referred as H0-B3LYP and H40-B3LYP respectively. As for the LDA, we used the Dirac-Slater exchange for the exchange part and the Vosko-Wilk-Nusair (VWN) [76] correlation functional for the correlation part.

The GTO basis sets were taken from the CRYSTAL basis set library [150]. In particular, valence electrons were described by triple-zeta basis sets, augmented with polarization functions [151-155] (for Li, only double-zeta + polarization). The exponents of the most diffused outer orbitals were re-optimized for the bulk crystals using the B3LYP functional and the complete basis set is given in the Appendix. The employed basis sets are of the following contraction: Li, 5-11(1); Na, 8-511(1); K, 86-511(31); Ag, 9766-311(41); F, 7-311(1); Cl, 86-311(1): Br, 976-311(31). Equilibrium lattice parameters were obtained by fitting calculated energy vs. volume data using polynomials.

All calculations were performed using tight tolerance factors for the coulomb and exchange series evaluation (ITOL values). The ITOL*n* (n=1, 2, 3, 4, 5) tolerance parameters were set to 7, 7, 7, 7, and 14, respectively. The SCF convergence threshold was set to 10^{-10} Hartree. The Brillouin zone integrations were performed using the (4×4×4) Pack Monkhorst k-mesh [156], whereas for frequency calculations a denser (8×8×8) Pack Monkhorst k-mesh was used. DFT exchange-correlation contributions were evaluated by numerical integration using the largest internally predefined grid (a pruned grid with 75 radial and 974 angular points) [69, 70].

The optical dielectric constant, electronic polarizability, and refractive index were evaluated using a highly accurate and analytical coupled Perturbed Kohn Sham Scheme (CPKS) that was recently implemented in CRYSTAL [83, 84, 157]. It was shown that [158, 159] the CPKS scheme is accurate for the calculations involving 0-, 1-, 2-, and 3-dimensional systems. To increase the computational accuracy we modified the above mentioned ITOL*n* values for all calculations mentioned hereafter to 8, 8, 8, 8, 16.

The transverse optic mode frequencies are evaluated by performing a vibrational frequency analysis [106, 160]. The Born charge tensor and static dielectric constant were evaluated through a Berry phase approach. For a description of the method and its recent applications we refer to a series of papers [161, 162]. The effective mass of electrons (m^*) was calculated for the bottom of conduction band by fitting the E (k) curve around the Γ symmetry point with parabola and using the relation $m^* = \left(\frac{d^2E}{dk^2} \right)^{-1}$ [in Hartree atomic units].

The variation of electronic band structure with respect to an external static electric field was studied using the Finite Field (FF) perturbation method [163] available in the code. In the FF method a sawtooth bare potential (square wave electric field) is applied along a given crystallographic direction. For these calculations, we used two different elongated supercells that are rotated so that the basal plane is perpendicular to the applied field direction. In this rotated basis the two supercells can be ascribed as (1×1×4) and (1×1×6). These elongated supercells were used to provide a region with a constant field value where the effects due to the change of slope in the bare potential are expected to be small. The static electric field was applied in three different crystallographic directions, i.e., [001], [011], and [111]. A schematic of the applied sawtooth-like bare potential (in the [001] direction) and resulting square-wave electric field is shown in Fig. 4-1 for the (1×1×4) supercell. Electric fields ranging from 0.00 to 0.02 a.u. (1a.u.=Hartree/Bohr = 51.42 V/Å) were applied along a given crystallographic direction; these values refer to a displacement field, which is related to a theoretical macroscopic electric field through a relation $F = F_0 / £_0$, where $£_0$, is the static dielectric constant.

An alternative scheme was also used to check the results. This scheme consists of applying a uniform static electric field to a slab in the direction orthogonal to the surface and the response properties are then evaluated at the center of the slab (the advantage of this model is that the electric field is not required to be periodic).

The breakdown field of the studied alkali halide crystals was evaluated by a general equation originally proposed by Callen [164] on the basis of the low-energy criterion put forward by von Hippel. Callen equation is related to the reststrahl energy $(\hbar µ_t)$, static $(£_0)$ and optical $(£_\infty)$ dielectric constants and has the following form:

$$\mathrm{F_b(Vcm^{-1})=134\times10^6}\hbar\omega_\mathrm{t}\left(\frac{\varepsilon_0\text{-}\varepsilon_\infty}{\left(\varepsilon_0\varepsilon_\infty{}^3\right)^{\frac{1}{2}}}\right)\left(\frac{m^*}{m}\right). \qquad 4.1$$

Where $\hbar µ_t$ is in units of eV and $µ_t$ is the transverse optic mode frequency, while m^*/m is the effective mass ratio. In alkali-halides, it is known that the Callen equation gives good agreement with experiments only with the $m^*/m = 1$ [165].

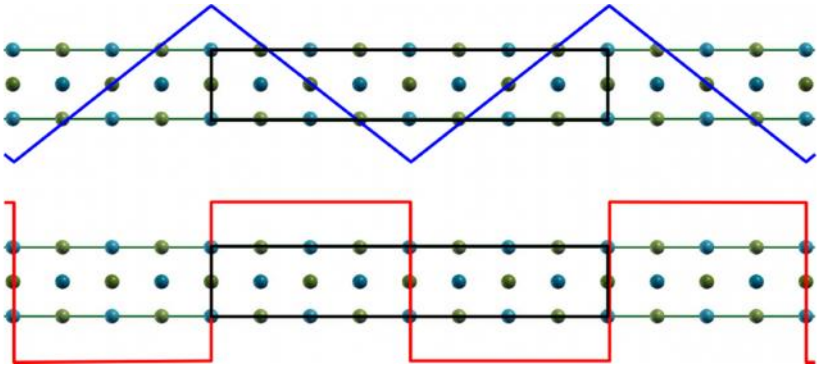

Figure 4-1: Schematic of the applied sawtooth electric potential (top) along the [001] direction and the resulting square wave electric field (bottom) in the case of (1×1×4) supercell of alkali halide crystal. Cations are cyan, anions are greenish.

4.3 Response properties of alkali halides under external static electric field

4.3.1 Results and discussion

4.3.1.1 Structural properties

Alkali halides have a rock salt crystal structure (face centered cubic symmetry) as shown in Fig. 4-2. The optimized lattice parameters at zero field, Mulliken net charges on the cations, and the bond populations along the nearest-neighbor alkali-halide distance are reported in Table 4-I. In all the cases, the lattice parameters are slightly overestimated, as usual for the B3LYP functional. Nevertheless, the maximum relative error is about 2%, which is acceptable. For a general comparison on the performance of different levels of theory, we have also collected some of the previous theoretical and experimental values in the Table 4-I [165, 166]. From our results it is evident that the error in the calculated lattice parameter is affected by both the cations and anions due to the electronic and interionic correlation effects [167]. The error always increases down the periodic table for both the cation and anion. For instance, the absolute error in the optimized lattice parameter is 0.05 Å for NaF and 0.10 Å for KF, whereas for NaCl the error is 0.09 Å. The net charges on the ions are evaluated according to a Mulliken population analysis. The net charge of alkali cation, q_M, is very close to the formal +1 |e| charge corresponding to the ideal ionic situation thus confirming the highly ionic nature of the alkali halides. This is further corroborated by a bond population analysis which gives vanishing values. As can be further seen from the table, the fluorides are more ionic than the chlorides as evidenced by both the net charges and the bond populations. Compared to the previous HF and DFT [166, 168] calculations, our B3LYP results for the Mulliken population analysis correctly predict the more ionic nature of the M-F bond compared to M-Cl bond, despite the use of a very rich basis set.

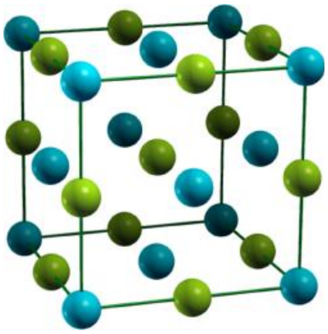

Figure 4-2: Crystal structure of alkali halide; cations are cyan, anions are greenish.

Table 4-I: B3LYP calculated lattice parameters and Mulliken population analysis for six alkali halide crystals.

Property	LiF	LiCl	NaF	NaCl	KF	KCl
Lattice parameter (Å)						
This work(B3LYP)	4.03	5.16	4.66	5.72	5.41	6.42
Experimental[a]	4.03	5.11	4.61	5.63	5.31	6.28
Relative error (%)	0.00	1.9	1.6	1.5	1.8	2.2
Others						
HF[b]	4.02	5.27	4.62	5.78	5.49	6.57
SCAD[c]	3.99	4.98	4.64	5.58	5.21	6.08
Mulliken charge of cation						
This work	0.96	0.81	1.01	0.97	0.94	0.89
Others						
HF[b]	0.86	0.94	1.01	0.97	1.00	1.00
Bond population						
This work	+0.002	+0.021	+0.003	+0.003	+0.007	+0.011
Others						
HF[b]	-0.003	+0.005	-0.015	-0.004	-0.018	-0.007

[a]Ref. [165] ; [b]Ref. [167] ; [c]Ref. [168]

4.3.1.2 *Dielectric and optical properties*

The calculated Born effective charge (Z_i^*), static $(\pounds_0)$ and optical $(\pounds_\infty)$ dielectric constants, electronic polarizability $(\sim)$, transverse optic mode frequency $(\neg_t)$, refractive index (n_∞), and electron effective mass (at the bottom of conduction band) of first six light alkali halides are reported in Table 4-II. Our results are in good agreement with the available theoretical and experimental values [165, 168, 169]. Because the alkali halides have cubic crystal structure, the dielectric and Born tensors are diagonal with equal diagonal elements. For this reason the average values of the diagonal elements are given in the Table 4-II for $\pounds_0$, $\pounds_\infty$, and Z_i^*. Because the Z_i^* values for cations and anions are complementary, only the values for cations are reported in the table. It can be noticed that the calculated Born effective charges for chloride salts are well over the formal ionic charges. This implies that the chlorides are more polarizable than the fluorides. The value of dielectric constant depends on the polarizability and is connected to valence charge density since the polarizability itself is a measure of deformability of electronic distribution. For a clear presentation of the polarizability, the response of the electron charge density of NaCl on the electric field perturbation of F_0= 0.02 a.u. is plotted in Fig. 4-3 for the (1×1×4) supercell along the [001], [011], and [111] crystallographic directions. It can be easily observed that a large polarization is induced on the chloride anions in all the three crystallographic directions (refer to anions in the middle of the flat field regions).

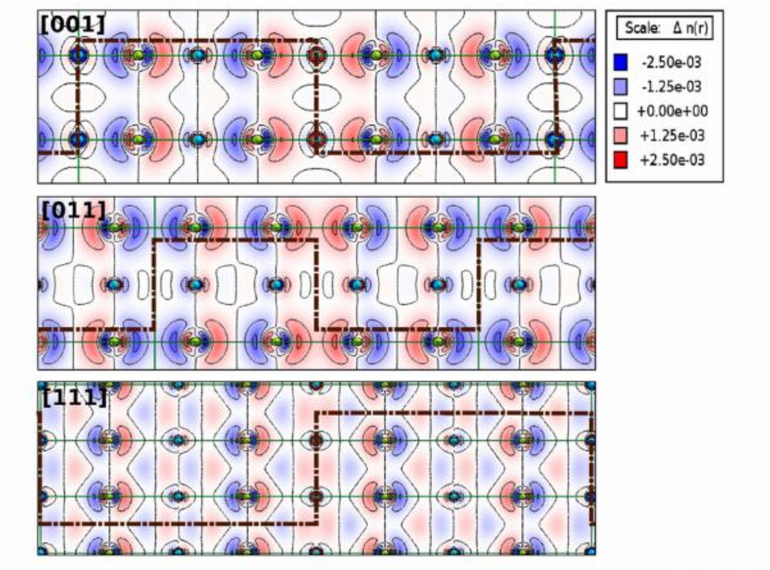

Figure 4-3: Electron charge density difference map between the perturbed (applied field of F_0=0.02 a.u.) and unperturbed (no field) NaCl system in three different crystallographic directions. Na^+ is cyan, Cl^- is greenish. Seven contours are drawn from -0.0025 to +0.0025 e-/bohr^3 with linear increments.

The calculated values of the high frequency dielectric constant were evaluated with the CPKS scheme. While making a comparison with the reported experimental values, the following factors should be taken into account: (i) our calculations correspond to a perfectly static crystal, which means that it is at zero Kelvin and the zero point vibrations are excluded; (ii) the experimental measurements may be affected by lattice phonons induced by finite temperatures; (iii) the experimental data may contain some defect or impurity induced errors; and (iv) the variation of the dielectric constant with the wave length is not taken into account in the current implementation of time–independent CPKS calculations. For all these reasons, the calculated values of the high frequency dielectric constant within a relative error of 5% are very acceptable. Our results show a general trend of the increase in the discrepancy from fluorides to chlorides. The static dielectric constants are overestimated by few percent. This is due to the underestimation of the transverse optic mode frequencies by a considerable amount. The reported high frequency refractive index, $n_{\infty} = \sqrt{\pounds_{\infty}}$, is also in fair agreement with the available experimental data.

4.3.2 Effect of electric field on the electronic and structural properties

We first investigated the electronic structure of alkali halides in the absence of external electric field. The B3LYP calculated values of the electronic band gap are presented in Table 4-III. For a comparison, the experimental band gap values [165] as well as those calculated by others [168, 170, 171] using either Hartree-Fock or LDA methods are also reported. Although the DFT typically underestimates the band gap, the B3LYP performs better than the pure GGA (generalized-gradient-approximation) functionals due to the Hartree-Fock part in the B3LYP functional [131].

As our intention is to study the variation of the band structure in the presence of the external static electric field, the band gaps were tuned close to experimental values by increasing the percentage of Hartree-Fock exchange in the B3LYP functional from 20 to 40%. Hereafter the so adjusted functional is denoted as H40-B3LYP. The H40-B3LYP calculated band gaps are also presented in Table 4-III, while the performance of H40-B3LYP for some other basic properties (e.g. lattice parameter, dielectric constants) is compared to that of B3LYP in Table 4-IV.

To study the response properties (structural and electronic) on static external electric field (F_0), the applied F_0 was set to a given value within the range from 0.00 a.u. to 0.02 a.u. These values correspond to the displacement fields, which are related to theoretical macroscopic fields through the relation $F = F_0 / \varepsilon_0$, where ε_0 is the static dielectric constant. Since all the crystals behave in the same way, for the sake of the brevity, only the results for the prototype NaCl crystal are presented. The response properties were studied by (i) the 1×1×6 supercell model of the bulk with the FF method utilizing a sawtooth external bare potential and (ii) a two-dimensional NaCl (001) slab model consisting of 9-layers, where a uniform static electric field was applied in the direction orthogonal to the surface. It was found that within the computational accuracy both models give the same results.

Table 4-II: B3LYP calculated and experimental values of optical and static dielectric constant, Born effective charge, transverse optic mode frequency, electronic polarizability per formula unit (f.u.), refractive index, and electron effective mass at the bottom of conduction band.

Property	LiF	LiCl	NaF	NaCl	KF	KCl
Static dielectric constant (ε_0)						
This work	10.1	14.1	5.11	6.42	5.65	4.92
Experimental[a]	9.01	11.9	5.10	5.92	5.51	4.86
Optic dielectric constant (ε_∞)						
This work	1.93	2.68	1.74	2.23	1.83	2.06
Experimental[a]	1.96	2.75	1.74	2.33	1.85	2.17
Born effective charge (Z_i*)						
This work	1.06	1.17	1.01	1.10	1.12	1.11
Experimental[b]	1.05	1.24	1.02	1.12	1.21	1.16
Others[c]	1.14	1.32	1.07	1.15	1.23	1.27
Transverse optic mode frequency (ν_{TO} /cm^{-1})						
This work	283	171	237	148	178	132
Experimental[a]	305	203	246	164	194	142
Electronic polarizability (α/(bohr^3/f.u))						
This work	8	31	10	31	18	38
Refractive index (n_∞)						
This work	1.39	1.63	1.32	1.49	1.35	1.43
Experimental[a]	1.39	1.66	1.33	1.54	1.36	1.47
Effective mass (m^*/m)						
This work	1.08	0.43	0.62	0.44	0.65	0.57
Others	1.2[d]	--	--	0.6[d]	--	0.5[a]

[a]Ref. [165]; [b]Ref. [172]; [c]Ref. [168]; [d]Ref. [169]

4.3.2.1 *Structural response*

The effect of electric field on the structural properties have been studied by fully relaxing the geometry in the presence of external static electric field applied along the [001] direction. It was found that in the presence of electric field, the lattice parameter along the applied field direction is almost not affected, at a displacement field of F_0=0.01 a.u. it expands by about 0.7% in the middle of the 9-layer NaCl (001) slab. However, there is an internal relaxation of ions and the corresponding pattern is shown schematically in Fig. 4-4.

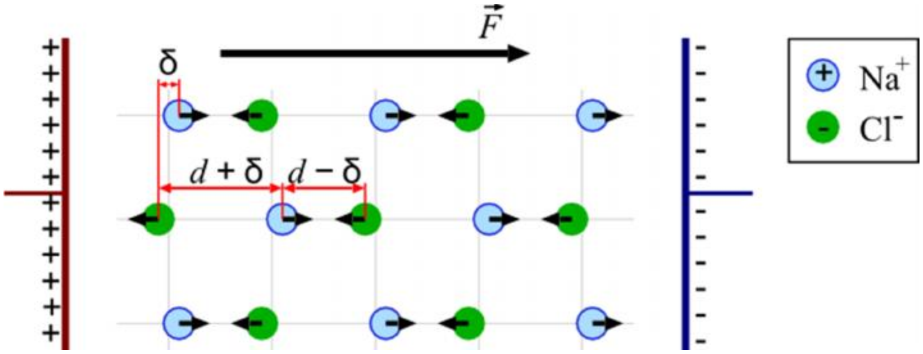

Figure 4-4: Schematic of the displacement pattern of ions due to the applied electric field along the [001] direction. Cations (cyan) are displaced along the field and anions (green) opposite to the field.

Cations (Na^+) are displaced along with the applied field, whereas anions (Cl^-) are displaced opposite to the field. Referring to the figure, this complementary displacements result in an expansion (contraction) of the cation–anion (anion–cation) distances by an amount of δ. The δ value increases linearly with the applied field and at a displacement field of F_0=0.01 a.u. the δ is about 0.07 Å. A similar behavior has been also observed in a previous study [145]. The fact that δ varies linearly with the applied field is rather reasonable, as for small displacements the potential should be quasi-harmonic.

Table 4-III: Calculated, experimental, and other theoretical values of electronic band gap (in eV).

Method	LiF	LiCl	NaF	NaCl	KF	KCl
B3LYP	11.68	8.05	8.70	6.96	8.86	7.77
H40-B3LYP	14.43	9.45	11.30	8.78	11.27	9.52
Experimental[a]	13.70	9.40	11.50	8.75	10.80	8.70
Others						
SCAD[b]	11.5	7.5	10.3	6.7	5.0	5.1
LDA[c]	7.65	5.59	5.77	4.92	6.26	5.98
HF+cc[d]	14.0	9.7	12.0	10.0	10.9	10.0

[a]Ref. [165]; [b]Ref. [168]; [c]Ref. [170]; [d]Ref. [171]

4.3.2.2 Electronic response

The applied electric field lowers the symmetry and makes the ions nonequivalent. Only the ions within a given layer that is perpendicular to the applied field direction remain equivalent to each other, i.e., anions to anions and cations to cations. This means that band structure, density of states (DOS), and band gap have significance only within the reference to a given layer. The main effect of electric field on electronic structure is shown in Fig. 4-5, which shows a layer resolved DOS for three consecutive layers. Notice that DOS simply follows the applied bare potential (black thick solid line), i.e., the DOS at each next layer is shifted by the amount the potential changes between the two consecutive layers. In addition to this shift, we also noticed that in the presence of electric field the bands (layer-resolved) widens. This can be seen from Fig. 4-6, which compares the DOS projected to a single (001) layer of NaCl in the absence and presence of 0.02 a.u. field. These two effects are by far the most important effects of electric field on DOS. It is worth mentioning that the effect of the induced structural relaxation on the band structure is rather small.

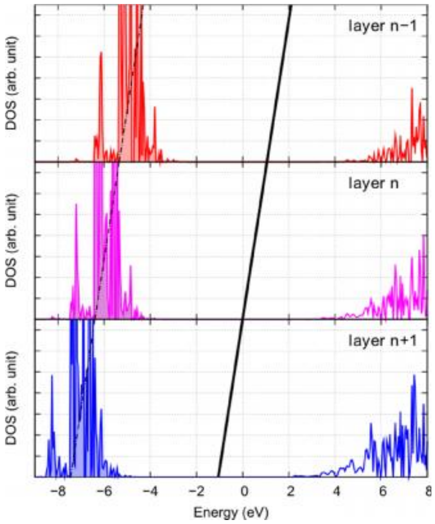

Figure 4-5: Layer resolved density of states (DOS) for NaCl exposed to the applied electric field along the [001] direction (F_0=0.02 a.u.). Notice that the DOS---consider, e.g., the centre of the occupied band---follows the change of the potential due to applied field. The black tilted bold line indicates the changing (macroscopic) potential.

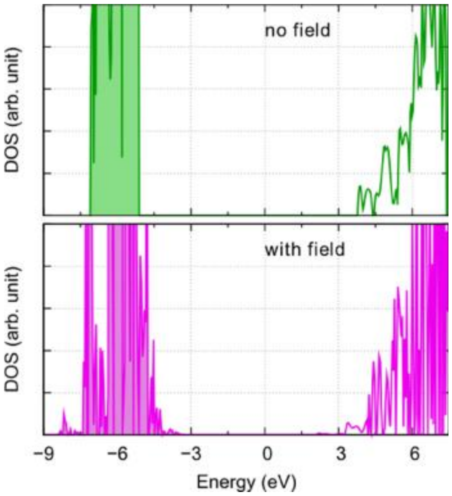

Figure 4-6: Comparison between the (001)-layer resolved DOS for NaCl at zero field (top) and at field of F_0=0.02 a.u. (bottom).

To explain the reason for the widening of the DOS, we plot in Fig. 4-7a the charge density associated with three bands that correspond to chlorine *p*-states at a given layer. Notice that although this states are mainly located at the reference layer (i.e. the one marked with the mesh), some satellite density extents to the first nearest-neighbor layers below and above it. This spill out of the density is the main reason for the widening of the DOS width, i.e., in addition to the states of the reference layer, also states from the first layer below and above it contribute to the DOS of the reference layer; this is schematically presented in Fig. 4-7b. The valence states of the layer above contribute to the top of the valence DOS, while the conduction states of the layer below contribute to the bottom of the conduction DOS of the reference layer. As a consequence of this band widening the band gap is reduced. On the basis of Fig. 4-7b, it can be estimated that the reduction of band gap (*ΔE*) is proportional to twice the amount that the applied bare potential (energy) changes (*ΔV*) between the two layers, i.e.

$$\Delta E \approx 2\Delta V = -2d_{12}eF, \tag{4.2}$$

where d_{12} is the interlayer spacing, e is the unit charge, and F is the macroscopic field value. The H40-B3LYP interlayer distance is 2.00, 2.84, and 3.27 Å for (011), (001), and (111)[4] layers of NaCl, respectively. When the magnitude of ΔE becomes equal to the band gap at zero-field, H40-B3LYP calculated zero-field band gap of NaCl is 8.8 eV -the band gap would vanish and the material would become metallic. This would, according to Eq. (4.2), happen at electric field strengths of the order of 100 MVcm^{-1}. However, the measured breakdown field for NaCl is two orders of magnitude smaller, 1.5 MVcm^{-1}. Note that Eq. (4.2) suggests anisotropy of dielectric breakdown on the direction of applied field or at least directional dependence of the breakdown paths (see von Hippel [173]). This anisotropy has been never observed in experiments.

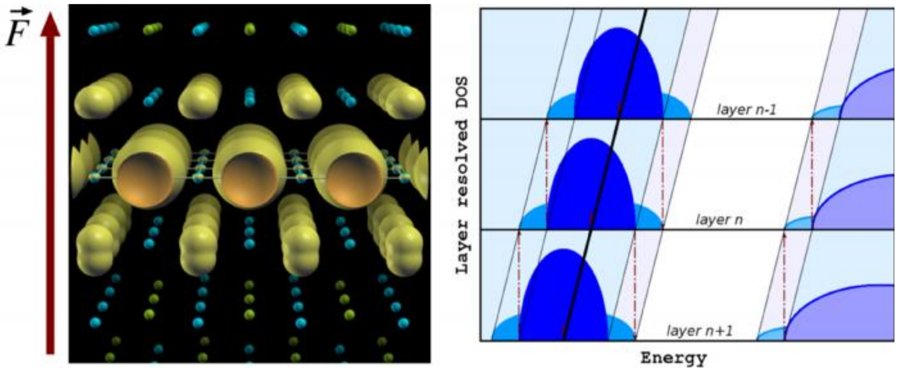

Figure 4-7: (a) The integrated local density of states corresponding to three p-states of Cl$^-$ at a reference (001) layer. The direction of the applied field is shown by the arrow. Note that although the density is mainly localized around the reference layer (marked by mesh) some satellite density is also located at the Cl$^-$ anions in the layer above and below the reference layer. (b) Schematic of the effect of this satellite spill out density on the width of the layer resolved DOS and the corresponding reduction of the band gap.

Table 4-IV: Comparison of a few properties as calculated by H40-B3LYP and B3LYP functionals. The values for the latter are in parenthesis.

Property	LiF	LiCl	NaF	NaCl	KF	KCl
Lattice parameter (Å)	3.99 (4.03)	5.19 (5.16)	4.61 (4.66)	5.67 (5.72)	5.36 (5.41)	6.39 (6.42)
Static dielectric constant (ε_0)	9.49 (10.07)	13.22 (14.13)	4.75 (5.11)	5.43 (6.42)	5.37 (5.65)	4.58 (4.92)
Optic dielectric constant (ε_∞)	1.89 (1.92)	2.60 (2.68)	1.69 (1.74)	2.21 (2.23)	1.79 (1.83)	2.03 (2.06)
Electronic polarizability (α/(bohr^3/f.u.))	7 (8)	30 (31)	9 (10)	30 (31)	16 (17)	36 (38)

---

[4] The (111) is composed of alternate layers consisting either solely of Na$^+$ or solely of Cl$^-$ and the reported distance is the distance between the two neighboring Cl$^-$ layers.

4.3.3 Dielectric breakdown

According to the intrinsic breakdown theory of Zener [174], the breakdown can be described as free electrons generated by tunneling from the occupied valence band to the conduction band (at the same energy) in the presence of a strong field. The reduction of the band gap described above would certainly aid in Zener tunneling, as it would increase the electron tunneling probability. However it is known that in large band gap dielectrics the Zener effect may be neglected [175]. The dielectric breakdown strengths of alkali halides are therefore neither related to the disappearance of the band gap nor to the Zener tunneling effect, but rather to the probability of exciting lattice vibrations and the electron-phonon scattering[5] [173, 175, 176].

For this reason we consider the dielectric breakdown on the basis of the low-energy criterion put forward by von Hippel [176] and we follow the equation developed by Callen [164], Eq. (4.1). The so calculated dielectric strengths are listed in Table 4-V. The agreement with experiments [165, 177] is rather good[6] with the exception of LiF for which the calculated dielectric strength is considerably overestimated; already Callen have pointed out that LiF is a notable exception (also see Fig. 4-8). Our results show a general trend of decrease in breakdown field value from fluorides to chlorides and from Li to K cations. The dielectric breakdown field strengths therefore display a similar trend as the band gaps, cf. Table 3. Indeed, there is a moderate linear correlation between the two as evident from Fig. 4-8, which compares the dielectric strengths and the band gaps (Experimental and calculated). Hence the dielectric breakdown fields and the band gap values may be seen as being indirectly related through the electronic structure of the material.

---

[5] In real materials there are always electron trap states, e.g., impurities and structural defects that reduce the tunneling probability.

[6] On the other hand, the use of the calculated effective mass ratios (cf. Table 4-II) would make the agreement with experiments rather unsatisfactory, which is compatible with the assessment that Callen equation works well if the $m^*/m = 1$ is used [17]. Sideshmukh, P.B., L. Siderhmukh, and K.G. Subhadra, Alkali Halides A Handbook of Physical Properties, Springer Series in Materials Science 2001].

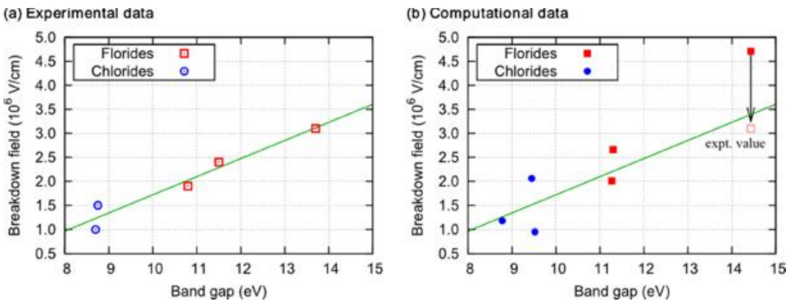

Figure 4-8: Correlation between the dielectric breakdown field strength and the band gap for first six alkali-halides. (a) Experimental [18, 60] and (b) our H40-B3LYP computational data.

Table 4-V: Calculated values of reststrahl energy (E_{vt}) and breakdown field (F_b). Experimental breakdown strengths from Refs., [165, 177] are also reported.

System	E_{vt} (eV)		F_b (MV cm^{-1})		
	B3LYP	H40-B3LYP	B3LYP	H40-B3LYP	Experimental
LiF	0.035	0.037	4.50	4.71	3.1
LiCl	0.021	0.022	1.97	2.06	---
NaF	0.029	0.031	2.53	2.66	2.4
NaCl	0.018	0.021	1.22	1.18	1.5
KF	0.022	0.023	1.91	2.01	1.9
KCl	0.016	0.017	0.95	0.95	1.0

4.4 Effect of electric field on the electronic properties of silver halides

Silver has a $d^{10}s^1$ electronic configuration, which is similar to the p^6s^1 configuration of the alkali metals, hence they are traditionally designated as the subdivision of alkali group [178]. Due to the comparatively weak shielding from the filled *d* orbitals, silver shows relatively high first ionization energy. The monovalent oxidation state is far more common than the divalent state. The bonding in silver halides is in borderline nature between ionic and covalent [179]; giving rise to unique properties and behavior compared to alkali halides. Although the mono halides of silver are structurally very simple and have many properties in common with the alkali halides, they are very good photocatalysts due to their low band gap and improved stability upon loading onto a conducting support; e.g., AgBr/SiO_2 [180] and AgCl/TiO_2 [181]. Through computational studies Galus *et al.* [182] showed that the photochemical activity of AgCl can be extended from the near-UV region into the visible region of the electromagnetic spectra through a process called self-sensitization. The silver halides also find application in different areas like photographic processes [183, 184], holography [185], photo and electro chemistry [186], catalysis [187-189], as liquid semiconductors [190], etc.

In photochemical applications, AgCl and AgBr are the most widely studied materials among silver halides both experimentally [191, 192] and theoretically [155, 186, 193, 194]. Both of them crystallize in the rock salt structure at room temperature. However their electronic structure is more complicated than the alkali halides. As Kunz [195] has highlighted their chief distinction from the alkali halides is the presence of 4*d* levels in the valence band, together with the halogen *p* levels. The energy proximity of the *d*-levels with the halogen *p*-levels brings strong *p–d* hybridization and results in considerable complexities, like the presence of an indirect band gap and the large band width of the valence band [195]. In 1970, Ballarò *et al.* [196] showed improved phonon assisted optical transitions under the presence of an electric field. In this context, a study on the variation of the electronic band gap and the band structure of AgCl and AgBr, under the influence of electric field is of interest from the perspective of visible light photocatalysis.

Following our previous work on alkali halides [197], we have evaluated the effect of electric field on the electronic properties of AgCl and AgBr. We also studied the breakdown strength of these materials by considering explicitly the numerically calculated effective mass ratio.

4.4.1 Structural properties

We begin with reporting the structural properties of the optimized AgCl and AgBr structures. The B3LYP, and LDA optimized lattice parameters, bulk modulus, and the pressure derivative of the bulk modulus are given in Table 4-VI and are compared with the available theoretical and experimental data. Overall, results are in fair agreement with the previously reported experimental and computational data. The B3LYP lattice parameters are overestimated by 0.3 Å as expected due to correlation of the fully occupied *d* electrons in the silver atom [198]. The overestimation of the lattice parameter reflects also in other structural parameters like bulk modulus and the pressure derivative of the bulk modulus as shown in Table 4-VI.

Table 4-VI: B3LYP (†) and LDA (‡) calculated lattice parameter, a_0 (in Å), bulk Modulus, B (in GPa) and pressure derivative of the Bulk modulus B′ (unit less). Available experimental (Expt) and other theoretical values (Others) are also reported for comparison.

	AgCl	AgBr
a_0	$5.84^{\dagger,}$ $5.51^{\ddagger}$	$6.08^{\dagger}$, $5.73^{\ddagger}$
Expt	5.55[a]	5.77[a]
Others	5.39 (SIC)[b], 5.41 (LDA)[c], 5.79 (GGA)[d], 5.61(PBE)[e]	5.71 (SIC)[b], 5.64 (LDA)[c], 5.90 (GGA)[d]
B	$35.7^{\dagger}$, $66.6^{\ddagger}$	$35.7^{\dagger}$, $61.2^{\ddagger}$
Expt	47[a]	45[a]
Others	71.6 (LDA)[f], 43.3 (PWGGA)[f], 66.8 (LDA)[c], 45.7 (PBE)[e]	63.5 (LDA)[f], 39.2 (PWGGA)[f], 60.3 (LDA)[c]
B′	$5.0^{\dagger}$, $5.51^{\ddagger}$	$6.2^{\dagger}$, $5.73^{\ddagger}$
Expt	5.98[g]	8.5[h]
Others	5.2 (LDA)[c],5.21 (PWGGA)[f], 4.4 (LDA)[f]	5.1 (LDA)[c], 5.3 (PWGGA)[f], 5.0 (LDA)[f]

[a]Ref. [199]; [b]Ref. [200]; [c]Ref. [201]; [d]Ref. [202]; [e]Ref. [203]; [f]Ref. [194]; [g]Ref. [204]; [h]Ref. [205].

The former is underestimated by nearly 30% and the later by 15%. On the other hand, despite the lattice parameters, which are very close to the experimental values, LDA gives less satisfactory values for bulk modulus and the pressure derivative of bulk modulus. The Mulliken population analysis, reported in Table 4-VII, shows ionic nature for AgCl and to lesser extent also for AgBr. In the case of AgCl, the net charge on the chlorine atom is 0.85 |e|, whereas for AgBr this value is reduced to 0.39 |e| thus showing a tendency towards having a covalent nature of bonding. The slightly higher value of 0.05 |e| given by the Mulliken bond population analysis for AgBr (0.02 |e| for Ag-Cl) further corroborates its covalent tendency. These findings are supported by Fig. 4-9, which shows the B3LYP formation densities (i.e. charge density difference between the SCF solution and the atomic superposition) of AgCl and AgBr. The spherical charge accumulation (intense red) and depletion (intense blue) regions around halogen and silver nuclei indicate the ionic nature of the crystals. Note also that, compared to AgCl, AgBr displays more pronounced charge accumulation in the interstitial region which is a sign of its larger percentage of covalent character.

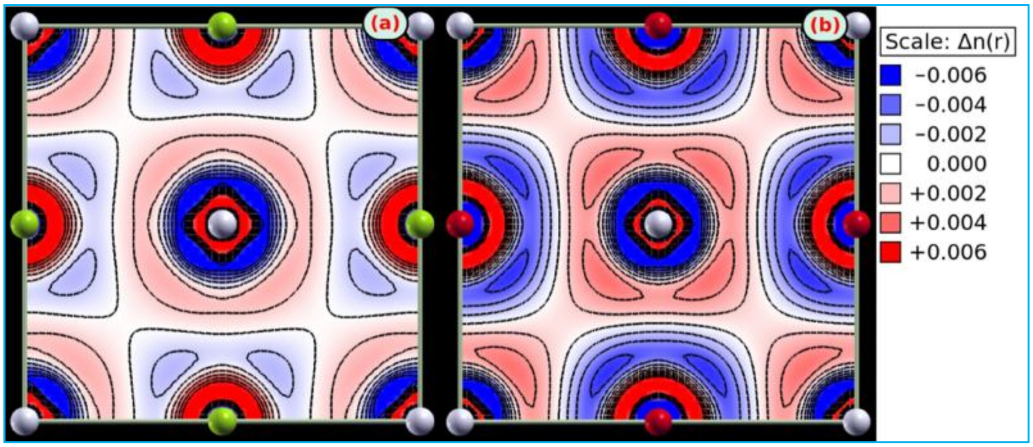

Figure 4-9: Formation densities (i.e., charge density difference between the SCF solution and the atomic superposition) of (a) AgCl and (b) AgBr crystals. Nine contours are drawn from -0.006 to +0.006 |e|/bohr^3 with linear increments. The blue color represents the electron deficit regions, while the electron excess regions are colored red, i.e., charge flows from blue to red regions.

As seen from Table 4-VII, the LDA values for the net charge and the bond population details are very close to that of B3LYP. However, LDA predicts a rather strong covalent nature for AgBr by giving the net charge for Br as 0.17 |e|. On the other hand the structural parameters given by the H0-B3LYP are almost same as the B3LYP values and so are omitted from Table 4-VII.

Table 4-VII: Mulliken Population analysis: B3LYP (†) and LDA (‡) values.

Property	AgCl	AgBr
Cation Charge (|e|)	$0.85^{\dagger}$, $0.83^{\ddagger}$	$0.39^{\dagger}$, $0.17^{\ddagger}$
Bond population (|e|)	$0.02^{\dagger}$, $0.03^{\ddagger}$	$0.05^{\dagger}$, $0.05^{\ddagger}$

4.4.1.1 Electronic, Dielectric and Optical properties

Since our key interest is to study the effect of electric field on the electronic properties like band gap and band structure of AgCl and AgBr, we calculated the direct and indirect band gap of both the crystals and these are reported in Table 4-VIII. For comparison, previously reported theoretical and experimental values are also presented in the Table. Our B3LYP, H0-B3LYP and LDA calculations clearly reproduce the indirect nature of the band gap, which is due to the complex *p-d* hybridization [195]. As shown in Table 4-VIII the reported direct and indirect band gap values are very close to the experimental values for B3LYP. On the other hand, LDA and H0-B3LYP (GGA variant) underestimate the band gaps as it is well known.

Table 4-VIII: Indirect (L-Γ) and direct (Γ-Γ) band gaps of AgCl and AgBr calculated with B3LYP, H0-B3LYP and LDA formalisms.

	AgCl				AgBr			
	B3LYP	H0-B3LYP	LDA	Expt	B3LYP	H0-B3LYP	LDA	Expt
Indirect band gap (eV)	3.66	1.88	1.36	3.2[a]	3.36	1.68	1.46	2.7[a]
Direct band gap (eV)	5.02	3.36	3.63	5.2[a]	4.45	2.89	3.18	4.3[a]

[a] Ref. [206].

The band structure and the nature of the bands on either side of the Fermi level are correctly reproduced [207] at the B3LYP level of theory. The B3LYP calculated band structure is shown in Fig. 4-10. The atoms as well as the orbital projected (Ag-*d*; Cl, Br-*p*) densities of states are plotted in Fig. 4-11. The high level of hybridization between the silver *d* and the halide *p* orbitals are clearly seen from Fig. 4-11. In Table 4-IX, we reported dielectric and optical properties calculated with all three density functionals. The optical dielectric constant (ε_∞), and refractive index (*n*) were calculated using the CPKS scheme and are in reasonable agreement with the available experimental data measured at 4.5 K and in the range of 10^2 -10^6 Hz. While the B3LYP and H0-B3LYP functionals underestimate optical dielectric constants, the LDA gives values which are very close to the experimental ones. For instance the relative error in LDA values for AgCl and AgBr are respectively +3.3% and -1.5%, while the error of B3LYP is -25% for AgCl and -30% for AgBr. The optical dielectric constant sensitively depends on the electronic band gap [208]. The reason that LDA gives such a good agreement with experimental ε_∞ is due to fortunate error cancelation, because it underestimates both the band gap and the oscillator strength. The discrepancies between the calculated and experimental values can be ascribed to the following factors. Our calculations refer to a perfectly static crystal, which means that the crystal is at 0 K and the zero point vibrations are omitted. In addition, the variations of dielectric constant with UV-visible wavelength is not taken into account in the present implementation of CPKS, while the experimental measurements of refractive index, $n = \varepsilon_{\infty}^{1/2}$ may be affected by the phonons at the zero frequency extrapolation. Also the experimental measurements may be affected by lattice phonons induced by finite temperatures. Finally, the experimental data may contain some defect or impurity induced error.

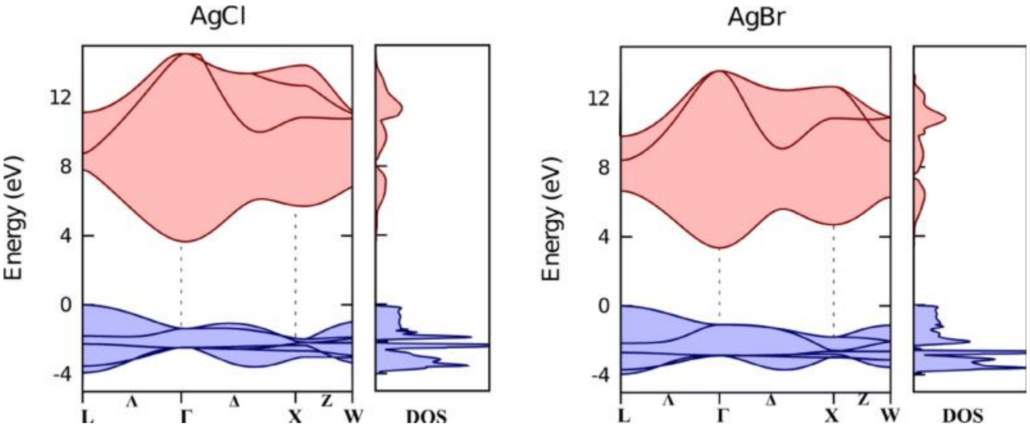

Figure 4-10: Band structure and total densities of states of AgCl and AgBr.

In order to calculate the Born charge tensor and the static dielectric constant ε_0, we performed a vibrational frequency analysis at gamma point. The longitudinal (ω_{LO}) and transverse (ω_{TO}) optic mode frequencies thus obtained are also presented in Table 4-IX and are compared with the experimental values. The B3LYP and H0-B3LYP functionals give values very close to the experimental values for both ω_{TO} and ω_{LO}, whereas the LDA values are too large. Due to the cubic symmetry of AgCl and AgBr, the Born charge and the dielectric tensors are diagonal with equal diagonal elements, similar to the case of alkali halides. Hence the average value of the diagonal elements $(Z_i^* \text{ and } \varepsilon_0)$ is reported in Table 4. Since the Z_i^* for cations and anions are complementary, only the values of cations are reported in the Table for brevity. As seen from Table 4-IX, the Z_i^* value is insensitive with respect to the Hamiltonian used. Compared to alkali halides (e.g., Z_i^* of Na in NaCl 1.06 |e| [197]) the Born charges of the silver halides are larger; for instance in the case of AgCl the Born charge for Ag is 1.37 |e| and in the case of AgBr it is 1.45 |e|. A large Z_i^* value of the crystal is a clear evidence of the strong ability of the Ag ions to polarize the halide ions.

Table 4-IX: Static (ε_0) and optical (ε_∞) dielectric constant, diagonal value of the Born charge tensor (Z_i^*), refractive index (n), transverse optic mode frequency ($³_{TO}$), and the longitudinal optic mode frequency ($³_{LO}$) of AgCl and AgBr crystals. Along with the B3LYP, H0-B3LYP and LDA results, experimental parameters are also reported for comparison.

	AgCl				AgBr			
	B3LYP	H0-B3LYP	LDA	Expt	B3LYP	H0-B3LYP	LDA	Expt
$£_\infty$	3.05	3.50	4.18	4.04[a]	3.21	3.77	4.55	4.62[a]
$£_0$	8.82	9.50	7.45	9.50[a]	7.88	8.76	7.44	10.60[a]
Z_i^*	1.37	1.39	1.37		1.45	1.49	1.48	
n	1.75	1.87	2.04		1.79	1.94	2.13	
$¬_{TO}$ (cm^{-1})	110.3	109.8	159.5	121.0[b]	93.2	92.9	132.1	91.4[b]
$¬_{LO}$ (cm^{-1})	183.7	181.1	212.9	197[a]	146.0	141.6	169.0	132[a]

[a]Ref. [209]; [b]Ref. [210].

Unlike the optical dielectric constant, the static dielectric constant is very sensitive to the Z_i^* and $³_{TO}$ values [208]. As reported in Table 4-IX, LDA largely overestimates $³_{TO}$, hence the Z_i^*, $³_{TO}$, and static dielectric constant values are the worst in the case of LDA. On the other hand, the $³_{TO}$ values of B3LYP and H0-B3LYP are in much better agreement with experiment, in particular for the case of the H0-B3LYP.

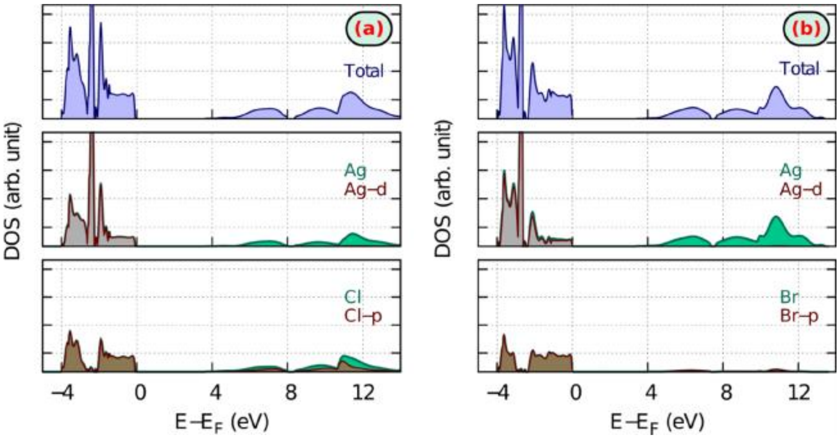

Figure 4-11: Total, atom projected (Ag, Cl and Br) and orbital projected (Ag-*d*, Cl-*p*, Br-*p*) densities of states of (a) AgCl crystal and (b) AgBr crystal.

4.4.2 Effect of external electric field

The effect of electric field on the electronic properties of silver halides was studied using the 1×1×6 supercell model of AgCl and AgBr, where an external static electric field (i.e., saw tooth potential) was applied along the z-direction. Several calculations have been performed where the electric field, F_0, was increased stepwise in steps of 0.0025 a.u. (1 a.u. of field corresponds to 5.14×10^{11} $\mathrm{Vm^{-1}}$). Here the electric field F_0 corresponds to the displacement field and is related to the macroscopic field, F via $F=F_0/\varepsilon_0$. Since the low band gap predicted by LDA and H0-B3LYP may lead to convergence problems in the presence of an external field, only B3LYP functional is considered for the modeling of the effect of external electric field on the electronic properties of the crystal. The results obtained from this were compared to those obtained from the 7-layer slab model calculations (see Computation details). We did not relax the geometry in the presence of electric field since a previous work on alkali halides has shown us that the relaxation of geometry has rather small effect on the electronic properties [145, 197]. The charge density difference map between the perturbed (applied field of F_0=0.01 a.u.) and unperturbed (no field) system along the [001] crystallographic direction of 1×1×6 supercell model is plotted in Fig. 4-12. It is clearly seen that the atoms are polarized along the applied field direction.

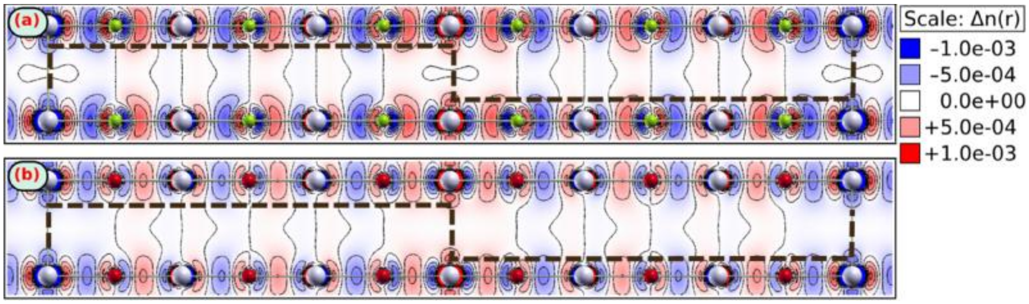

Figure 4-12: The charge density difference map between the perturbed (applied field of F_0 = 0.01 a.u.) and unperturbed (no field) system: (a) AgCl and (b) AgBr. Nine contours are drawn from -0.001 to +0.001 |e|/bohr^3 with linear increments. Coloring is according to Fig. 4-9.

In order to assess the effect of electric field on the electronic properties, we present the results obtained from the slab model. Because the applied electric field breaks the symmetry of the crystal, the energy levels lose the degeneracy and the atoms become nonequivalent. Thus only ions within a given layer that is perpendicular to the field direction remains equivalent (i.e., anions to anions and cations to cations). This means the electronic properties, such as; band structure, density of states (DOS), and band gap have significance only when referring to a given layer. In Fig. 4-13, we report the layer resolved density of states for three consecutive layers in the middle of the slab. It can be seen that the DOS simply follows the potential (black thick solid lines). That is, the DOS at each next layer is shifted by the amount the potential changes between the two consecutive layers. The other observation in the presence of electric field is the band widening. For instance, in Fig. 4-14, we plotted the DOS projected to the middle layer of the slab, both in the presence (F_0=0.01 a.u.) and absence of electric field. The effect on the valence band width is much more pronounced than that in the conduction band. The reason for the band widening is that bands associated with a given layer are not strictly localized around it due to nonzero off diagonal terms in the Hamiltonian in the presence of electric field perturbation. This results in the spill out of charge density to neighboring layers. This is similar to the case we have explained in the earlier section on alkali halides. Unlike the case of alkali halides, where the states are delocalized up to the first nearest neighbor layers [197], the delocalization is considerably larger for silver halides. Analysis of electronic densities of individual valence states at Γ-point reveals that the delocalization extends up to second nearest neighbor layers. According to this picture, the upshift (downshift) of the upper (bottom) edge of the valence band is equal to $l_{\text{de}}eF$, where l_{de} is the extent (length) of delocalization, e is the unit charge, and F is the macroscopic field value. From Fig. 4-14, it can be inferred that in the presence of F_0 = 0.01 a.u. field the upper edge of the valence DOS is up shifted, compared to the zero field case, for about 0.88 and 0.76 eV for AgCl and AgBr, respectively (the bottom edge is downshifted for similar amount). The resulting value of l_{de} is 5.3 Å for AgCl and 5.1 Å for AgBr, which corresponds to nearly twice the interlayer distance along the [001] direction for both the crystals, thus confirming above arguments.

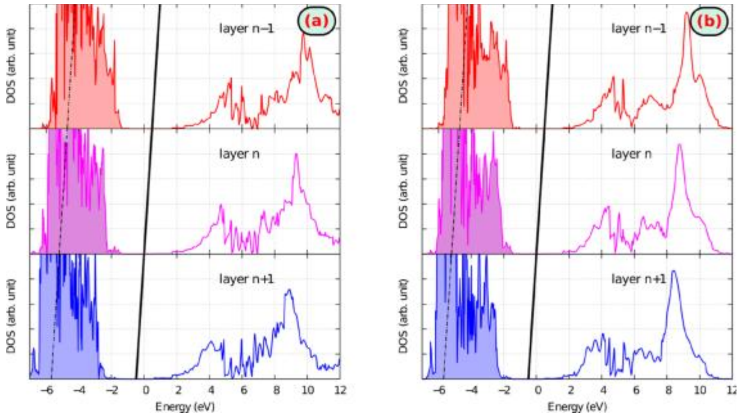

Figure 4-13: Layer resolved density of states (DOS) for three consecutive layers for (a) AgCl and (b) AgBr exposed to the applied electric field along the [001] direction (F_0 = 0.01 a.u.). Notice that the DOS follows (dash-dotted line) the change of the potential due to applied field. The black tilted bold line indicates the changing (macroscopic) potential.

Due to the increased band widths, the band gap value is correspondingly reduced and would vanish at enough large field strength. For instance, the band gap reduces by 0.98 eV for AgCl in the presence of F_0=0.01 a.u. field implying that the band gap would vanish at the field value of F_0=0.037 a.u. (this corresponds to a macroscopic field of 0.004 a.u.= 20 MVcm^{-1}). The crystal would, however, undergo dielectric breakdown much before this field is reached, because the experimental breakdown strength is two orders of magnitude smaller (0.15 MVcm^{-1}). A considerable red shift in the band gap value indicates that, an external electric field can be used to tune the band gap of a wide band gap semiconductor to fit into the visible region of the solar spectra. In addition, a reduction in the band width is an indication of an enhancement in the charge transfer kinetics, especially for semiconductors with low hole diffusion length.

Like in the case of alkali halides, also for silver halides the dielectric breakdown is therefore not related to disappearance of band gap. As pointed out long ago by Callen, the dielectric breakdown strength is often due to vibrational contributions and other parameters like temperature and the defects of the crystal [164]. In such a situation, calculation of the dielectric strength of the crystal by including the vibrational contribution to the dielectric constant is indispensable.

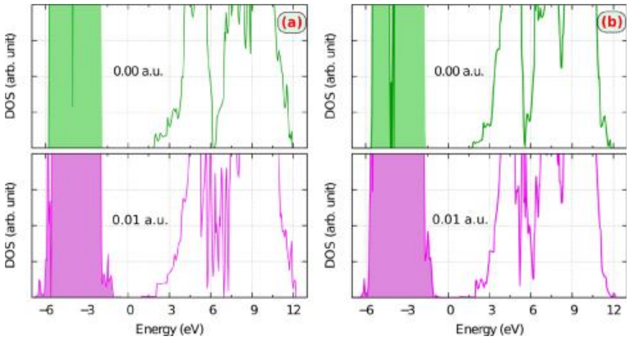

Figure 4-14: Comparison between the density of states projected to the middle layer of the (001) slab in the presence (F_0=0.01 a.u.) and absence of electric field for (a) AgCl and (b) AgBr.

4.4.3 Dielectric breakdown

Following our previous work on alkali halides [197] we made an attempt to calculate the dielectric strength of AgCl and AgBr. For that we have followed the general equation, Eq. (4.1), proposed by Callen, for the alkali halide type crystals at 0K, developed from von Hippel's low energy criterion [176]. In his original paper Callen approximated the effective mass ratio (*m*/m*) by setting it to 1 for alkali halides. Here we report the performance of the Callen equation for the dielectric breakdown strength of AgCl and AgBr compared to that of alkali halides.

First, we calculated the dielectric strength by using our calculated parameters and setting the effective mass ratio to 1, because in the case of alkali halides the so obtained values show reasonable agreement with the experimental strengths [197]. The so calculated values are reported in Table 4-X and it is evident that they are several times larger compared to experimental breakdown field value of AgCl crystal, 0.15 MVcm^{-1} (no experimental datum is available for AgBr, to our knowledge). The overestimation is the largest for B3LYP (factor of four) and smallest for LDA functional (factor of two). This may imply that in the case of correlated systems like silver halides, the breakdown strength is largely sensitive to the effective mass ratio. For this reason, we recalculated the dielectric strengths by using the numerically calculated effective mass ratios. Effective mass ratio was calculated by fitting the lower conduction band energy against several **k** points close to the minimum at Γ-point using a quadratic polynomial. The fitting was performed for different directions, namely, X-Γ-X, L-Γ-L, and W-Γ-W. Due to the high symmetry, the effective mass ratio is almost the same in all the directions. The average value of *m*/m* is about 0.3 (see Table 4-X) and leads to B3LYP and H0-B3LYP breakdown strengths in much better agreement with the available experimental value, while the value given by LDA is underestimated by a factor of two and a half. The agreement with experiment is especially good for H0-B3LYP and the reason that it outperforms B3LYP is because it predicts more accurate static and optical dielectric constants, while both of them give almost identical transverse optic mode frequency. Hence one could conclude that the most predictive functional for the breakdown field strength is the one which predicts the static and optical dielectric constants as well as the transverse optic mode frequency with a reasonable accuracy. Unfortunately, the experimental value for the breakdown strength of AgBr is not available, which would make the comparison and conclusion more reliable.

Table 4-X: Reststrahl energy (μ_t), effective mass ratio (m^*/m) and dielectric breakdown strengths calculated by $m^*/m=1$ $(F_b^{m^*/m=1})$ and by using calculated m^*/m $(F_b^{m^*/m=calc.})$ for AgCl and AgBr crystals. The only available experimental datum is the breakdown strength of AgCl.

Property	AgCl			AgBr		
	B3LYP	H0-B3LYP	LDA	B3LYP	H0-B3LYP	LDA
μ_t (eV)	0.014	0.014	0.016	0.012	0.012	0.019
m^*/m	0.38	0.33	0.29	0.33	0.27	0.23
$F_b^{m^*/m=1}$ (MVcm^{-1})	0.67	0.54	0.37	0.45	0.40	0.24
$F_b^{m^*/m=calc.}$ (MVcm^{-1})	0.25	0.18	0.06	0.15	0.09	0.11
$F_b^{Experimental}$ (MVcm^{-1})		0.15[a]				

[a]Ref. [210].

4.5 Summary

In this chapter, we have presented the effect of an external static electric field on the structural and electronic properties of alkali halide and silver halide crystal families. From our studies, we have observed that the electric field induces a considerable red shift in the band gap of the material. Thus an external electric field can be used for tuning the band gap of a UV active photocatalyst to the visible region of the solar spectra. In addition we also found that, in the presence of the electric field, the band width of the material increases. This is very beneficial for the charge transport properties, especially in the case of indirect band gap semiconductors. We also provided an explanation for the band widening by considering the spreading of electron charge density in the presence of the electric field. Finally, we have calculated the dielectric strength of all these crystals using the equation proposed by Callen. By contrast to alkali halides, for correlated systems like AgCl it is very important to consider the effective mass ratio to calculate their dielectric strength.

5 STRUCTURAL, ELECTRONIC AND MAGNETIC PROPERTIES OF A NOVEL BI-BASED PEROVSKITE, BIVO$_3$

5.1 Introduction

Intense research work on the development of an efficient visible light driven photocatalyst is ongoing at the global level. It is aimed at addressing the planetary need for water and air purification and hydrogen fuel production by the splitting of water. To date, no single candidate has met all the requirements for water splitting, with an economically viable efficiency (ca. 10 %) [1, 2]. In addition to the countless efforts in improving the catalytic activity of existing photocatalytic semiconductors, such as TiO_2 [94], Fe_2O_3 [34], $BiVO_4$ [211], much attention has been paid in developing novel single phase metal oxide visible-light active photocatalysts. However, the challenge is still open as metal oxides are poor visible light absorbers (band gap >3 eV), despite their excellent chemical stability.

It has been demonstrated [212, 213] that the 6*s* orbitals in Pb^{2+} and Bi^{3+}, 5*s* orbitals in Sn^{2+}, and 4*d* orbitals in Ag^{4+} can form valence levels above the O-2*p* valence levels. The contribution of these orbitals to the valence band depends on the crystal structure and the concentration of the metal cations in the compound. Thus, a novel oxide semiconductor with a narrow band gap can be developed by incorporating the aforementioned cations in the structure. From a structural point of view, generic ABO_3 perovskites are good starting structures, as their compositional and structural flexibility enables a variety of fascinating properties such as ferroelectricity, superconductivity, ferromagnetism, antiferromagnetism, and large dielectric constants. Several perovskites have shown stable photocatalytic activity under illumination, e.g., $SrTiO_3$ [214], $NaTaO_3$ [215], $KTaO_3$ [215], $AgTaO_3$ [216]. Many Bi-based (especially with transition metals) low band gap semiconductors have also been realized, e.g., $BiVO_4$ (2.4 eV) [36], $BiInO_3$ (2.08 eV) [217], $BiGaO_3$

(2.03 eV) [218], $BiCrO_3$ (1.5 eV) [219], $BiMnO_3$ (1.1 eV) [220], $BiFeO_3$ (2.5 eV) [221]. For a detailed description of the perovskite structure see section (1.3.2).

In addition to the observed catalytic activity, Bi-based oxide perovskites have recently gained much interest due to their multi-functionality [222]. Bi-based transition metal oxides can be considered as an alternative to lead-free ferroelectrics and multiferroics materials [223-226]. The multiferroics constitute a class of materials where two or more ferroic orders such as ferromagnetism, ferroelectricity and ferroelasticity coexist in the same phase [227]. Most of the recent research has focused on materials that combine some form of magnetic order with ferroelectricity [228] therefore, nowadays, the word "multiferroics" is often used instead of "magnetoelectrics". Due to their versatility, multiferroics find application in multiple state memory devices, electric field controlled ferromagnetic resonance devices, transducers with magnetically modulated piezoelectricity, etc. A striking factor about multiferroics is that, there is no unique theory which describes the properties of multiferroics; and hence each material has to be studied on its own. Generally, the ferroelectricity in an ABO_3 perovskite is driven by a d^0 or d^{10} transition metal ion at the B-site and hence they are nonmagnetic. Thus ferroelectricity and ferromagnetism, in general, are treated as mutually exclusive. This is not the case if the A site contains a Bi or Pb ion. A bismuth ion in the 3+ state is similar to the Pb in the 2+ state; both of them possess the $6s^2$ lone pair electrons. These lone pair electrons have, in general, a tendency to hybridize with the n*p* orbitals and hence to off-center the Bi/Pb ions from their ideal positions in the polyhedral. This off-centring could lead to ferroelectricity [224, 226, 227]. In addition to the off-centring driven ferroelectricity, for the material to be multiferroics, a partially filled transition metal ion should be present at the B site to drive ferro/antiferromagnetism.

With a transition metal, having a partially filled *d* orbital, occupying the perovskite B-site, a net magnetic moment can be introduced into the system. In that case both ferroelectricity and ferromagnetism can co-exist and be coupled within a single system (multiferroics). Hence, incorporation of transition metals on the B-site in Bi-based perovskites has been intensively investigated for the past few years. Among the first row transition metals, Bi-based perovskites with Sc, Cr, Fe, Mn, Co, and Ni at the B-site have already been realized. Among them, $BiFeO_3$ and $BiMnO_3$ have been extensively investigated and they are demonstrated to be multiferroics [219, 223, 229]. Early attempts to synthesize $BiVO_3$ [230] and $BiTiO_3$ [230] have not been successful due to the oxidation of V^{3+} and Ti^{3+} to their 4+ oxidation state, which resulted in the formation of $Bi_4M_3O_{12}$ (M=V, Ti) [230, 231]. No attempts to synthesize $BiCuO_3$ have yet been reported. Because of this, almost nothing is known about either the stability or the properties of the V^{3+}, Ti^{3+} and Cu^{3+} perovskites.

In this chapter, making use of the structure predicted by the *SPuDs* software, we present a complete ab-initio characterization of the structural, electronic, magnetic and dynamical properties of the paraelectric phase of $BiVO_3$.

5.2 Computational details

The parallel version of CR09 installed at the Marenostrum supercomputing centre, Barcelona has been used for the calculations in this chapter. All electron basis set has been employed for vanadium and oxygen atoms and has the following contraction V: (8-6411d(31G)); O (8-411(d1)) [150]; while the Hay and Wadt large core pseudopotentials have been employed for the heavier bismuth atom [232]. The complete optimized basis sets are given in the Appendix. All calculations have been performed using the tight tolerance factors (ITOL*n* parameters) for the Coulomb and exchange series evaluation. In the present context the ITOL*n* parameters were set to 8, 8, 8, 8, 14. The convergence in total energy for all the calculations was set to 10^{-10} Hartree. The Brillouin zone integration was carried out using a 6×6×6 Pack-Monkhorst **k**-mesh (resulting in 80-**k** points) and a denser 10×10×10 (312 **k**-points) mesh for evaluation of one-electron properties.

A parameter, which is often used [227, 233] to estimate the stability of the perovskite is its tolerance factor, t, defined as $t = \frac{r_A + r_B}{\sqrt{2}(r_B + r_O)}$ where r_A, r_B, and r_O represent the ionic radius of A-, B-site cations and the oxygen atom respectively [212, 217]. Using the Shannon ionic radii [234] we have calculated the tolerance factor of $BiVO_3$ as 0.892 and found it to fit well into the perovskite family. Starting from this, we have predicted the crystal structure of $BiVO_3$ using the *SPuDs* [235], crystallographic structure prediction and diagnostic software. The optimum magnitude of the octahedron tilting is calculated using the bond valence model as suggested by Brown [236] and is related to the minimum difference between the calculated bond valence and the formal charge. The program calculates the optimal configuration of a given composition in ten Glazer tilt systems by distorting the structure to minimize the global stability index while maintaining the rigid octahedral. The global stability index was found to be at its minimum (0.0089) for the orthorhombic *Pnma* space group.

The lattice parameters of aristotype $Pm\overline{3}m$ and the hettotype orthorhombic $Pnma$ structure were optimized using the B1WC hybrid functional. The B1WC hybrid functional was chosen for the present purpose, because it has shown excellent reproducibility of structural, electronic, and magnetic properties of Bi-based transition metal oxide perovskites such as $BiFeO_3$ [232, 237], $BiMnO_3$ [237]. A benchmark description on its excellent functionality has recently been demonstrated by Dovesi *et al.* [238]. The energy gradient in the presence of electric field is not yet been available with respect to the WC exchange functional. Hence we chose the B3LYP functional for the evaluation of the optical dielectric constant using the CPKS scheme. This was required for calculating the IR-reflectance spectra as well as the static dielectric constants. In the relaxation of the cell parameters and the atomic coordinates using the B1WC functional, the convergence was tested on the RMS and the absolute value of the largest component of the gradients and the estimated displacements (quasi Newton optimization scheme). A more detailed description is provided in an earlier section, see section (2.3.7.3). The thresholds for the maximum force, the RMS force, the maximum displacement, and the RMS atomic displacement on all atoms have been set to 0.0045, 0.0003, 0.00180, and 0.0012, respectively. Such tight parameters were necessary for ensuring a high degree of accuracy in the vibrational frequency calculations.

5.3 Results and discussion

According to the bond valence calculations performed by the *SPuDs* software [235] the orthorhombic *Pnma* structure has the minimum global stability index (0.0089). The *Pnma* structure can be thought of as being formed by repeated tilting of the VO_6 octahedral unit in a zig-zag manner ($GdFeO_3$ type distortion [239]) as shown in Fig. 5-1. The tilting can be assigned as two anti-phase tilts of equal magnitude (i.e., $a^-b^+a^-$) with respect to the [100] and [001] pseudo cubic axes and an in-phase tilt with respect to the [010] pseudo-cubic axes. The tilting results in a decrease in symmetry as well as in an increase in the size of the unit cell from one formula unit (5-atoms) for the cubic cell to four formula units (20-atoms) for the orthorhombic cell. For a detailed description on the distortion in perovskites see section (1.3.2). The total energy of the aristotype cubic and the hettotype orthorhombic structures after relaxing the geometry are presented in Table 5-I. As seen from the table, the ferromagnetic orthorhombic structure is 1.275 eV/f.u. lower in energy compared to the cubic structure. Thus, structurally the orthorhombic phase is far more stable than the cubic. In addition, the B1WC functional predicts the electronic nature of the cubic structure as conducting while that of the orthorhombic structure as semiconducting. This further corroborates that the cubic structure is less likely to be the ground state of $BiVO_3$ crystal. Similar instabilities for the cubic structures are noticed for the other perovskites from the same family. For example, Ravindran *et al.* [222] have shown on the instability of the cubic phase of $BiFeO_3$ because of its higher energy (1.1 eV/f.u) compared to the *R3c* phase. Since the cubic structure is shown to be less stable, from here onwards we focus mainly on the hettotype orthorhombic *Pnma* structure, and data from the cubic structure will be provided when a comparison is indispensable. The *Pnma* structure has a point group symmetry of D_{2h} (space group 62 in the standard setting), with four formula units per unit cell. Therefore, there are four transition metal atoms in the unit cell and this allows assigning different anti-ferromagnetic structures in addition to the ferromagnetic structure.

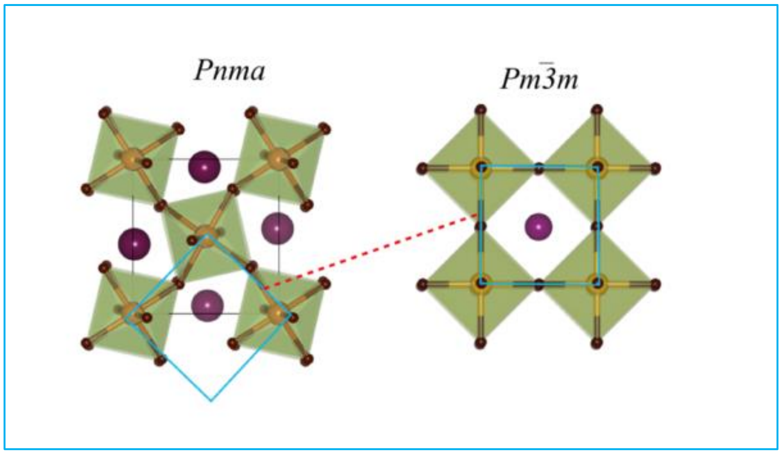

Figure 5-1: Pnma structure (left) is shown as a distorted derivative of the cubic structure (right). For a clear indication of the nature of the distortion, the undistorted cubic part is notated as a blue square. Coloring of the atoms is as follows: Bi (dark magenta); V (dark orange (left); O (dark brown).

Table 5-I: Total energy per formula unit (f.u) of cubic $(Pm\bar{3}m)$ and orthorhombic $(Pnma)$ BiVO$_3$. The energy of the ferromagnetic *Pnma* structure is taken as the reference energy. Total energy corresponds to different antiferromagnetic setting of *Pnma*, A-AFM, C-AFM, and G-AFM is also provided.

Structure	$Pm\bar{3}m$ FM	$Pnma$ (FM)	$Pnma$ $(A-AFM)$	$Pnma$ $(G-AFM)$	$Pnma$ $(C-AFM)$
Total Energy (eV/f.u.)	-31955.67891	-31956.95370	-31956.92895	-31956.90702	-31956.92593
$\Delta E = (E - E_{Pnma}^{FM})$(eV)	1.275	0.0	0.02475	0.0466	0.0277

In our case we have assigned all the possible three anti-ferromagnetic orderings, namely A-type (A-AFM), G-type (G-AFM) and C-type (C-AFM)[7]. The total energies of all three relaxed anti-ferromagnetic structures are collected in Table 5-I. As it can be seen from the table, the energy difference between the ferromagnetic and the anti-ferromagnetic structures is very small. These nearly degenerate energies indicate on a high level of competition among the FM and the AFM states and possibility on a magnetic phase transition even at low temperature. In the present study, the slightly more stable FM (ca. 25 meV compared to the close lying AFM

---

[7] A-AFM-type: the nearest neighbor moments are ferromagnetically coupled in a within a defined plane and antiferromagnetically coupled between neighboring planes; C-AFM-type: the nearest neighbor moments are antiferromagnetically coupled in a within a defined plane and ferromagnetically coupled between neighboring planes; G-AFM-type: all the nearest neighbor moments are antiferromagnetically coupled: 228. Silvia, P. and E. Claude, *First principles studies of multiferroic materials.* Journal of Physics: Condensed Matter, 2009. **21**(30): p. 303201.

state) state is considered as the ground state of $BiVO_3$, on which a full characterization of the structural electronic and vibrational properties is performed.

5.3.1 Structural properties

The calculation showed that the perovskite $BiVO_3$ ground state structure is orthorhombic *Pnma* (D_{2h}). In the nonmagnetic state, the D_{2h} point group contains 8 symmetry operations, namely E, C_{2x}, C_{2y}, C_{2z}, σ_x, σ_y, σ_z, and i. In the magnetic states, four of these symmetry operations become permissible only if the time reversal symmetry T is present, and hence in the magnetic state, the symmetry operations become; E, TC_{2x}, TC_{2y}, C_{2z}, $T\sigma_x$, $T\sigma_y$, σ_z, and i. However in the ferromagnetic state, the time reversal symmetry cannot be a symmetry operation as it would reverse the spin, hence the symmetry operations are reduced to four within the FM setting. As a result the assigned space group will be C_{2h}, the invariant unitary subgroup of D_{2h}. In the present case, the number of irreducible atoms in the asymmetric unit increases from four to six with the magnetic setting. The Wyckoff positions are assigned according to the C_{2h} point group symmetry. The assigned Wyckoff positions as well as the optimized atomic coordinates are given in Table 5-II. As seen from the table, only the vanadium atoms are at the special position. The optimized lattice parameters for both cubic and orthorhombic structures are also presented in the Table 5-II. Since *Pnma* structure can be treated as a derivative structure of the cubic, the lattice parameters of the former can be deduced from the later as $a \approx c \approx \sqrt{2}a_{cubic}$, and $b \approx 2a_{cubic}$. The lattice parameters calculated for the *Pnma* structure from the cubic structure are given in Table 5-III in parentheses. The table shows that, the lattice parameters are in good agreement with the values predicted from the cubic lattice parameter. The optimized structure of orthorhombic $BiVO_3$ is shown in Fig. 5-2 and the corresponding bond lengths are presented in Table 5-II. As can be seen, there are six different V-O bond lengths coming from the octahedrons centered at V1 and V2. In the cubic case the V-O bond length is 1.93 Å while that of Bi-O is 2.72 Å. However when it comes to the *Pnma* structure the V-O bond length increases by ca. 4% and the Bi-O bond length decreases by ca. 17%. This indicates that both the V-centred and Bi-centred polyhedra are highly distorted in the *Pnma* structure.

The V-O-V bond angle in the cubic structure is 180°. Conversely, in the *Pnma* structure, two vanadium and three oxygen atoms are crystallographically non-equivalent. As a result there are three different V-O-V bonds. The V1-O2-V2 and V1-O3-V2 bond angles lying in the **a-c** plane are calculated as 149.6º and 147.3º, while the V1-O1-V2 bond angle measured along the **b** axis is 148.8°. This large deviation of the bond angles from 180° indicates stronger octahedral tilting. The tilt angles are estimated[8] from the lattice parameters as 9.25º, 19.09º and 22.03º for the [110], [001] and [111] pseudo-cubic axes, respectively. These values calculated from the cell dimensions may not exactly correspond to the original values; since the distortion of the octahedral is not taken into account. Nevertheless, the calculated values of the tilt angles close to the common $GdFeO_3$ type distortions, e.g., $GdFeO_3$: 9.46º, 17.58º, 19.89º for the [110], [001] and [111] pseudo-cubic axes, respectively.

The high level of octahedral tilting in orthorhombic $BiVO_3$ will result in an extended mixing of the orbitals. Such mixing of orbitals would be responsible for stabilizing a magnetic ground state. In other words, due to a dramatic reduction in the bond angles connecting the neighbouring transition metal atoms (V1-O-V2), the direct exchange interaction will be favoured (always ferromagnetic) due to weak σ bonding between V and O atoms. This substantiates the stability of FM state (insulator) in the *Pnma* structure compared to the metallic cubic state.

The net charges on all the irreducible atoms are also presented in Table 5-II. The net charge on the Bi atom, i.e., +3.471 |e| is well above its formal charge of +3 |e|, this shows a strong localization of charge density close to the bismuth atom (lone pair). These lone pair electrons are responsible for the large reduction in the Bi-O bond length. By contrast the net charge on the V and O atoms are well below from their formal value of +3 |e| and -2 |e|, indicating a very strong covalent bond between them.

---

[8] From the cell dimentions **a**, **b** and **c** the tilt angle corresponding to three pseudocubic axes are calculated as follows, $¤_{[110]} = \cos^{-1}\left[\frac{\sqrt{2}\mathbf{c}}{\mathbf{b}}\right]$, $-_{[001]} = \cos^{-1}\left[\frac{\mathbf{c}}{\mathbf{a}}\right]$, and $\Phi_{[110]} = \cos^{-1}\left[\frac{\sqrt{2}\mathbf{c}^{2}}{\mathbf{ab}}\right]$.

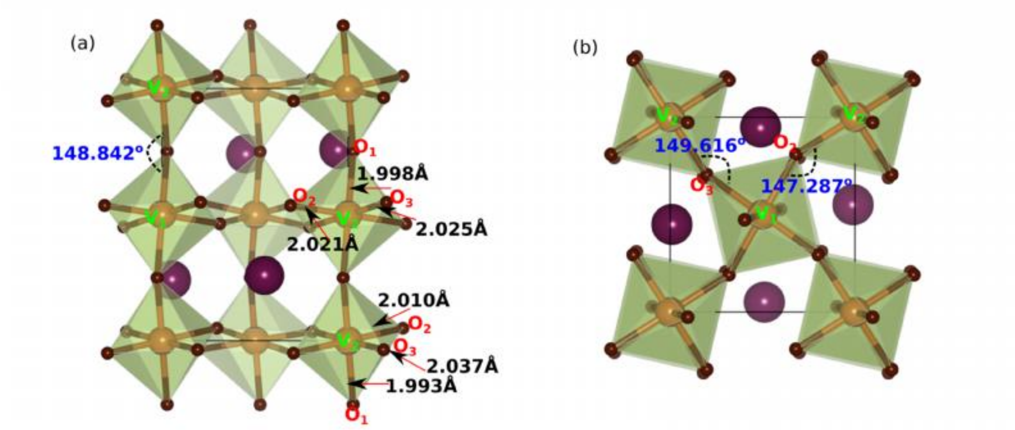

Figure 5-2: Optimized structure of FM-BiVO$_3$. The bond lengths are measured in Å and the angle is measured in degrees. (a) projection along the c-axis (b) projection along the b-axis. Coloring of the atoms has been done according to Fig. 5-1.

Table 5-II: B1WC optimized fractional coordinates, Wyckoff positions, net charge (q) on the irreducible atoms, lattice parameters and volume (**Ω**). Values in the parentheses shows the lattice parameters of the *Pnma* structure predicted from the cubic parameters.

Fractional Coordinates and Wyckoff positions (*Pnma*)					
Atom	x	Y	z	Wyckoff position	q (|e|)
Bi	-0.4494	0.2588	-0.0102	4f	+3.471
V1	0.5	0.0	0.5	2d	+1.918
V2	0.0	0.0	0.0	2a	+1.924
O3	-0.0269	0.2496	0.0960	4f	-1.140
O5	0.1905	-0.0362	0.3188	4f	-1.159
O6	0.2938	0.0493	-0.1989	4f	-1.152

Lattice parameters and volume				
Structure	a(Å)	b(Å)	c(Å)	Ω (Å^3)
$Pm\overline{3}m$	3.85	-	-	57.20
Pnma	5.66 (5.44)	7.69 (7.70)	5.35 (5.44)	232.8(228.8)

Table 5-III: Population analysis: the nearest neighbour cation-anion distance, bond populations and cation-anion bridging angle. Values in the parentheses show the corresponding parameters in the cubic structure.

Cation-Anion Pair	Distance (Å)	Bond Population
Pnma		
Bi-O1	2.26 (2.72)	-0.069
Bi-O2	2.28	-0.064
Bi-O3	2.39	-0.089
V1-O1	2.00 (1.93)	0.039
V1-O2	2.02	0.034
V1-O3	2.03	0.037
V2-O1	1.99	0.038
V2-O2	2.04	0.027
V3-O3	2.01	0.040
V-O-V	bond angle (deg)	
V1-O1-V2	148.8° (180°)	
V1-O2-V2	149.6°	
V1-O3-V2	147.3°	

5.3.2 Electronic properties

For a detailed description of the electronic properties of orthorhombic $BiVO_3$ we begin with the band structure plots. In Fig. 5-3, we have plotted the band structure of $BiVO_3$, both in the up spin and down spin channel along eight high-symmetry points in the irreducible part of the Brillouin zone (BZ). The plotted energy range is from -14 to +8 eV, the lower lying semi-core states are omitted from the plot for clarity, and the top of the valence band is aligned to zero. As seen from the figure, the top of the valence band lies in between the T and R high symmetric points, while the bottom of the conduction band lies at the high symmetry point, T. Since the top of the valence band and the bottom of the conduction band corresponds to different k-points, the nature of the electronic transition in $BiVO_3$ should be indirect. The calculated indirect band gap between the highest occupied crystalline orbital (top of the valence band) and the lowest unoccupied crystalline orbital (bottom of the conduction band) is 1.76 eV. Fortunately in the case of $BiVO_3$, a direct band gap value of 1.96 eV is calculated at the Γ point (centre of the BZ) and this value indeed falls in the visible region of the spectra. Such a narrow and direct band gap would result in very good absorption of visible light. Thus $BiVO_3$ can be considered as a very promising candidate for water splitting applications. The calculated low band gap value is in a good agreement with the general trend from the Bi-based transition metal perovskite family, e.g., $BiCrO_3$ (1.5 eV) [219], $BiMnO_3$ (1.1 eV) [220], $BiFeO_3$ (2.5 eV) [221].

Further analysis of the bands shows that the valence and conduction bands are highly dispersed. Apparently, the higher dispersion in the bands is an indication of lesser effective mass for the charge carriers (holes in the valence band and electrons in the conduction band). As a direct consequence, holes and electrons will have higher mobility, enhancing charge carrier kinetics. This one-to-one correspondence between the dispersion in the band structure and the high mobility of the charge carriers has been demonstrated in many photocatalytic materials, for instance see Kudo *et al.* [36] and Kim *et al*. [240],

To gain a qualitative insight into the nature of the bands, we have plotted in Fig. 5-4, the total and atom projected density of states. The width of the upper valence band is about 8.3 eV and is separated from the lower valence band with an energy gap of nearly 1.7 eV. As discussed for hematite (an indirect band gap semiconductor) in chapter 3, a large band width in the valence band is always very beneficial for the photo-response of a material, as it would substantially reduce the recombination probability for the exciton pair and enhance the effective charge transport in the bands. The lower conduction band is narrow and is separated from the wider upper conduction band by a very narrow gap of nearly 0.1 eV (in the up spin channel - alpha). As seen from Fig. 5-4, the oxygen and vanadium levels are nearly degenerate throughout the energy range from -8.3 to +7 eV. This indicates a very strong covalent nature of the bonding between oxygen and vanadium and can thus be attributed to the highly entangled bands, especially in the upper valence band region.

Although the bismuth levels also fall in the same energy range as oxygen, the hybridization between the Bi-*s* and O-2*p* facilitates mainly the antibonding interaction due to the distortion of the octahedra. The Bi-*p* states are mostly empty, and a small fraction of these appears in the top of the valence band, just below the V-3*d* states due to the stericochemical activity of the lone pair (cross gap hybridization). This can be further linked to the Mulliken bond population details given in Table 5-III (see the third column). The covalent nature of the V-O bonding is substantiated by the higher positive bond population (0.027 |e| to 0.040 |e|), while the Bi-O weak bonding is supported by the large negative population (-0.064 |e| to -0.089 |e|) of the bonds.

The contribution of different orbitals to a given band can be assessed from the orbital projected density of states plotted in Fig. 5-5. In the upper valence band, the hybridization between the O-2*p* and V-3*d* orbitals are clearly visible. In the lower edge of the upper valence band, the O-2*p* orbitals are dominant, while the energy range closer to the top of the valence band is dominated by the vanadium 3*d* levels. Due to the octahedral coordination of the V atoms, further decomposition of the 3*d* levels into the t_{2g} (d_{xy}, d_{yz}, d_{xz}) and the e_g (d_{x2-y2}, d_{z2}) manifolds is necessary. The decomposition of the V-3*d* bands, as shown in the Fig. 5-5, indicates that the t_{2g} levels dominate in contribution to the *d* orbitals at the top of the valence band. Regarding the contribution of bismuth, both the 6*s* and 6*p* orbitals are well separated from each other. The fully occupied 6*s* orbitals lay in the -12.4 to -10 eV range; in Fig. 5-3 the highly parabolic bands in the -12.4 to -10 eV range corresponds to this level. A small contribution of Bi-3*p* falls in the upper valence band. This is apparently due to the charge transfer from the oxygen 2*p* levels to the Bi 6*p* levels (cross gap hybridization due to lone pair electrons) due to the reduced Bi-O bond length in the *Pnma* structure compared to the cubic.

The lower conduction band is predominantly contributed by the V-*3d* orbitals. From the orbital projected DOS (see Fig. 5-5), it is clear that these V-*3d* orbitals are mainly contributed by the t_{2g} levels just as in the case of the top of the valence band. The upper conduction band is dominated by the unoccupied Bi 6*p* orbitals with a small fraction of contributions from O-2*p* and V-3*d* orbitals. Thus, from the band structure analysis, it is clear that the top of the valence band as well as the bottom of the conduction band predominantly comes from the V-*3d* orbitals. Hence, one can conclude that $BiVO_3$ is a low band gap (ca. 2 eV) Mott-Hubbard (*d-d* transition) insulator.

Since the absolute position of the valence and conduction band edges has a crucial role in the water splitting reaction, commenting on this aspect, for the orthorhombic phase of $BiVO_3$ is decisive. From early reports on V^{3+} doped hematite and TiO_2 it is clear that the 3+ state of vanadium always falls above the Fe-3*d* and Ti-3*d* levels. If this is true, we could anticipate that a band gap of 2 eV for $BiVO_3$

would initiate O_2 evolution smoothly and perhaps H_2 evolution would need a small bias. However, we are unable to present a quantitative data on this since we lack vacuum as a reference level in our calculations.

Due to the centrosymmetric nature of the crystal the DOS of the Bi-6*p* is very low in the occupied bands (a strong hybridization is necessary to populate the Bi-6*p* levels). Although the cross gap hybridization between the O-2*p* and Bi-6*p* orbitals is very weak, there is a possibility for ferroelectric instability in a low symmetric structure due to a lone pair effect. If such a structure could exist (non-centrosymmetric) one would expect a much stronger hybridization between oxygen and bismuth, which would eventually reduce the symmetry and stabilize the ferroelectric structure. In consistence with the earlier reports on $BiFeO_3$ and $BiMnO_3$, strong cross gap hybridization will increase the band gap of $BiVO_3$. When a ferroelectric phase is formed, the bottom of the conduction band will be dominated by the Bi-*6p* orbitals; this will widen the band gap and further disperse the bands. For instance, Goffinet *et al.*, [232] and Ravindran *et al.*, [222] have calculated that in the ferroelectric $R3c$ phase of $BiFeO_3$, the band gap value is higher by 0.5 eV compared to its paraelectric $R\bar{3}c$ structure. If this would happen in a ferroelectric phase of $BiVO_3$, then one might expect that the conduction band edge will fall well above the proton reduction potential and should, in principle, facilitate H_2 evolution.

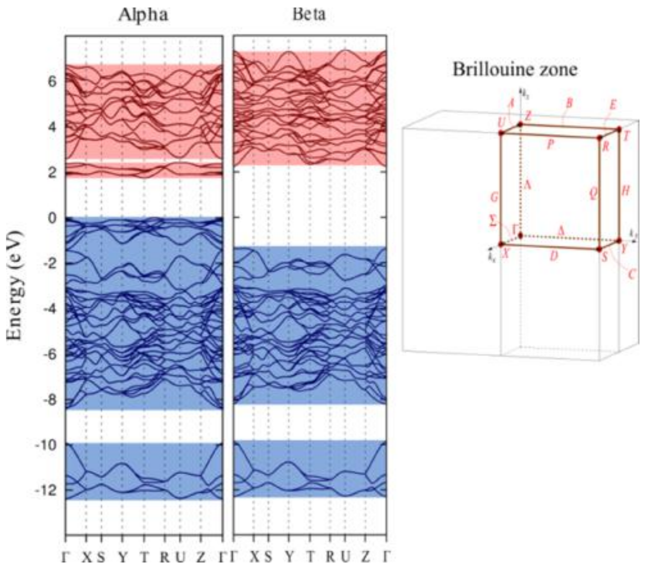

Figure 5-3: Band structure (alpha and beta) of the paraelectric ferromagnetic phase of $BiVO_3$ plotted along the high symmetric points in the irreducible part of the first Brillouin zone. The shapes of the Brillouin zone as well as the special points in the BZ are notated at the right panel.

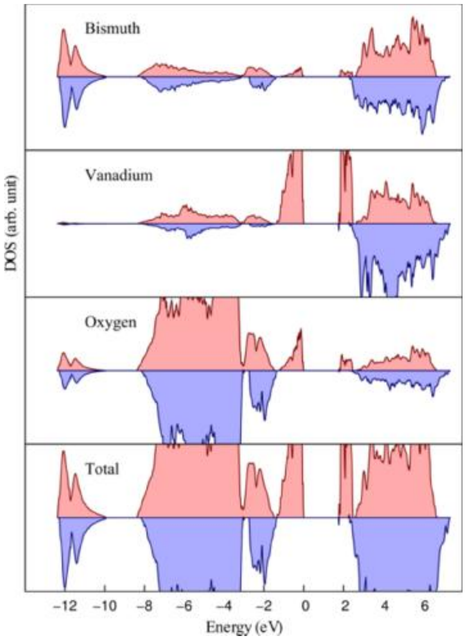

Figure 5-4: Total and atom projected DOS of $BiVO_3$. The top of the valence band is taken as the zero reference energy (Fermi energy). Red and blue areas represent the contributions from alpha (up) and beta (down) spins respectively.

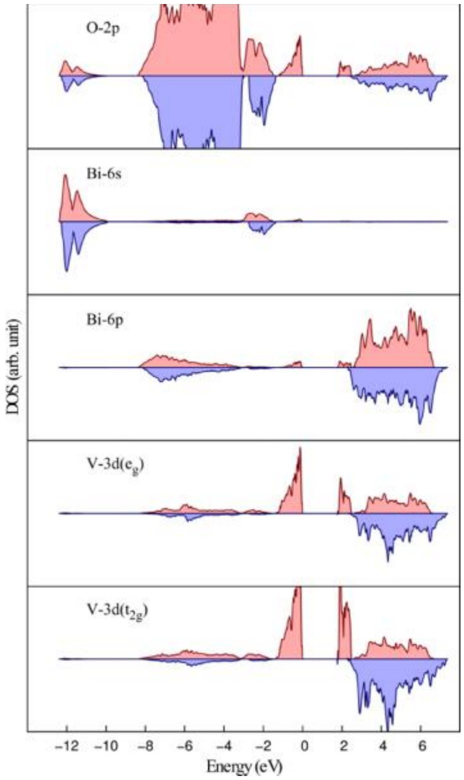

Figure 5-5: Orbital projected DOS of $BiVO_3$. Top of the valence band is taken as the reference zero energy. Colouring of the graph is according to Fig. 5-4.

5.3.3 Dielectric properties

5.3.3.1 Static and optical dielectric constants

Since the energy gradient in the presence of an electric field with respect to the WC exchange functional has not yet been implemented in CR09, the optical dielectric constant $(£_{\infty})$ is calculated using the B3LYP functional within the CPKS scheme. At fixed geometry, influence of the functional choice on the dielectric constant value is rather small [241]. Hence we have used the B1WC optimized lattice parameters for the evaluation of the optical dielectric constant using the CPKS functional. The dielectric tensor is highly isotropic for orthorhombic crystals; hence only the diagonal elements of the tensor are presented in Table 5-IV. The calculated static dielectric constant $(£_{0})$ is also present in Table 5-IV. The static dielectric constant shows high anisotropy along different Cartesian directions. The higher values of the dielectric constant are expected due to strong covalent bonding between V-O and the anomalous Born effective charges.

Table 5-IV: Static $(£_{0})$ and optical dielectric $(£_{\infty})$ constant of $BiVO_3$ in different Cartesian directions**.**

Component	$£_{0}$	$£_{\infty}$
Xx	43.3	6.3
Yy	115.9	6.5
Zz	36.9	6.3
zx=yz	2.1	--

5.3.3.2 Born effective charge tensor

The Born charge tensor (Z^{*}) is an inevitable quantity in describing the lattice dynamics of a complex crystal. In binary crystals the Born charge tensor can be extracted from the infrared measurements. But for materials like distorted perovskites, having complex structure, the experimental determination of Z^{*} is not straight forward due to the LO-TO splitting. For a detailed description of the evaluation of Z^{*} by computational means we refer to the earlier section, (see section 2.3.7.4). The calculated Born effective charge tensor is given in Table 5-V. The formal valence charge of Bi, V, and O in $BiVO_3$ are +3, +3 and -2 respectively. Due to the ferromagnetic nature of the crystal, the site symmetry is reduced from D_{2h} to C_{2h} as discussed in the previous section. As a consequence of this, a large anisotropy is observed in the diagonal values of the Z^* tensor as evidenced from Table 5-5. In the rigid ionic picture, in which the ions are assumed to have a closed shell like structure, the charge will be localized on the ion and hence each ion would carry an effective charge close to its nominal ideal ionic value. For instance, in a high symmetric ionic oxide material, the Z^* value of oxygen would be close to its nominal value of -2. However, for crystals like $BiVO_3$ this is not the case due to the covalent nature of the bonding. Due to the covalency, the charge density is strongly delocalized and these rearrangements of electrons give rise to anomalous Born effective charge. An anomalous Born effective charge is therefore a good indication of the off-centring tendency of an atom by covalent bond formation (often considered as an indication of ferroelectricity). The high value for the Born charge tensor, thus triggers a much higher spontaneous polarization when a relative displacement of adjacent atoms occurs. As shown in Table 5-V, the Z^* value of Bi is very high $(Z^*_{zz} = 4.99)$ compared to its nominal value (+3), this indicates the strong tendency of Bi atoms to off-center due to the lone pair effect. Similar high values of Z^* for Bi ion are reported for many other Bi-based perovskite oxides (e.g. $BiFeO_3$ ($Z^*_{Bi} = 4.23$) [232]. In order to build up the spontaneous polarization, the centrosymmetry has to be lifted. However in the present work the FM structure of $BiVO_3$ remains as centrosymmetric and thus shows zero spontaneous polarization, i.e., the crystal remains paraelectric.

Table 5-V: Born Effective charge tensor of $BiVO_3$ in different Cartesian directions.

Atom	Z^*_{XX}	Z^*_{YY}	Z^*_{ZZ}	Z^*_{xy}	Z^*_{xz}	Z^*_{yx}	Z^*_{yz}	Z^*_{zx}	Z^*_{zy}
Bi (4f)	4.919	5.226	4.992	0.173	0.127	0.111	-0.115	-0.556	-0.071
V1 (2d)	4.145	3.753	4.275	-0.400	0.028	-0.077	0.043	-0.248	-0.034
V2 (2a)	3.901	3.947	3.622	0.085	-1.005	0.254	-0.154	-0.602	-0.211
O1 (4f)	-2.880	-3.370	-2.854	-0.144	-0.650	0.237	0.195	-0.588	-0.109
O2 (4f)	-3.047	-2.893	-2.639	-0.269	-0.172	-0.184	-0.138	-0.129	-0.222
O3 (4f)	-3.491	-2.814	-3.020	0.347	-0.400	-0.359	0.113	0.250	0.246

The Z^* value for Bi shows a variation of +1.9 to +2.2 from its ideal ionic value. This shows as a charge transfer between the n*p* orbitals of the nearest neighboring Bi and O atoms. As discussed earlier, this is a direct consequence of the lone pair effect and can be linked to the small Mulliken charge of -1.14 |e| on the O atom (see Table 5-II). Conversely, the noticeable off-diagonal component in all the three oxygen sites is a clear indication of a large hybridization between the V-3d orbitals and the O-2*p* orbitals and this is in consistent with the Mulliken population analysis

5.3.4 Vibrational frequency at gamma point

The point group C_{2h} has only four symmetry operations. There are twenty atoms in the orthorhombic unit cell giving rise to 60 normal modes. The decomposition of the irreducible representation built on the basis of the Cartesian coordinates of the atoms in the unit cell leads to the following symmetry assignments for the 60 normal modes.

$$\Gamma_{\text{total}} = 18\,\text{AU} \oplus 18\,\text{BU} \oplus 12\text{AG} \oplus 12\text{BG}$$

All the 60 modes are active; of these 36 $(18\,\text{AU} \oplus 18\,\text{BU})$ modes are IR active and the remaining 24 modes $(12\text{AG} \oplus 12\text{BG})$ are Raman active. Among the 36 IR active modes three modes corresponds to translation $(1\text{AU} \oplus 2\text{BU})$. The simulated IR and Raman modes are presented in Table 5-VI. Unfortunately, there are no experimental data available for a detailed comparison. As seen from the table, the spectrum is continuous from 60 cm^{-1} to 670 cm^{-1}. In order to consider the long range Coulomb effects due to the coherent displacement of the crystal nuclei, a correction is added to the Hessian matrix. This essentially depends on the electronic dielectric tensor and the Born effective charge. All the AU modes except one that corresponds to the translation undergo LO-TO shift. Two highly positive (59.1 and 360.0 cm^{-1}) and two negative (-48.2 and -31.9 cm^{-1}) shifts are observed. An IR active mode at 77.1 cm^{-1} (BU) is observed with a very high intensity of ~2767 cm^{-1}. A detailed analysis of this mode suggests that, it is likely to be rotational (O-Bi-O). The rotation corresponding to this mode can be anticipated as the system prefers stabilization of the paraelectric structure than the off-centring driven ferroelectric structure (this would show an unstable soft mode), at least at the B1WC level of the theory.

The nature of each mode can be further analysed by an isotopic substitution of the constituent atoms. Substitution of an isotope with higher mass compared to the original atom will result in a negative shift $(\Delta\neg\ \mathrm{cm}^{-1})$ in the modes $(\neg\ \mathrm{cm}^{-1})$. A shift less than -5 cm^{-1} can be ignored. In the present case the ^{209}Bi atom is substituted with a ^{212}Bi, ^{51}V is substituted by ^{54}V, and ^{16}O is substituted by ^{18}O. The shifts in the peak positions with respect to the isotopic substitution (one at a time) are shown in Fig. 5-6. As seen from the figure, the contribution of the vanadium atom is only to the IR active modes in the 200-400 cm^{-1} range, while the Bi atom contributes only to the modes in the low wave number range (60-110 cm^{-1}). The oxygen atoms contribute to all modes and the isotopic shift increases with the frequency. All Raman modes above 100 cm^{-1} are affected by the isotopic substitution of oxygen. The shifts in the Raman modes are between 20 and 40 cm^{-1} in the high frequency range. The IR reflectance spectra are calculated from modes and the oscillator strengths (ionic contribution to the static dielectric tensor; see section (2.3.7.4) for more details). The corresponding spectra for three different Cartesian directions are plotted in Fig. 5-7. The damping factor is set to 9 cm^{-1} and the angle of incidence is kept as 10° and the intensities are normalized to unity.

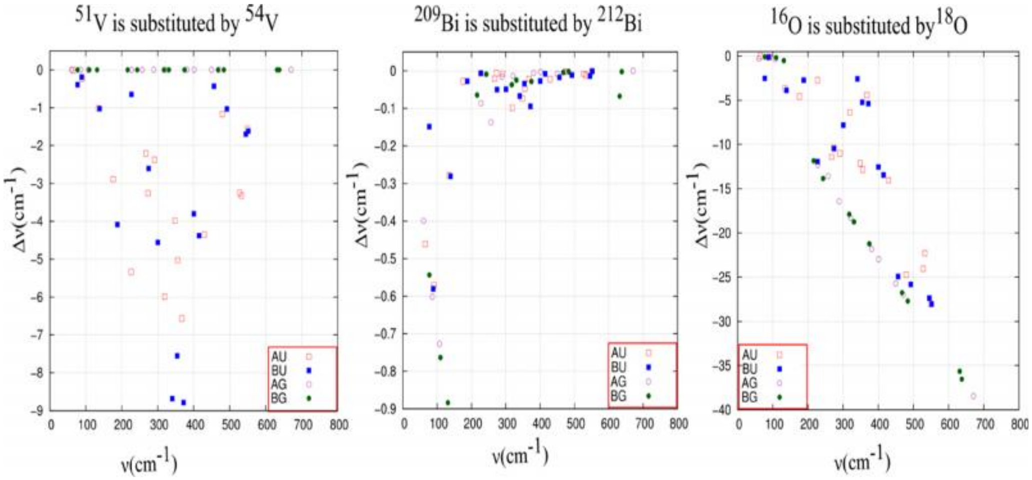

Figure 5-6: The shifts in the IR and Raman modes with respect to isotopic substitution are shown. ^{51}V is substituted by ^{54}V, ^{209}Bi is substituted by ^{212}Bi, and ^{16}O is substituted by ^{18}O**.**

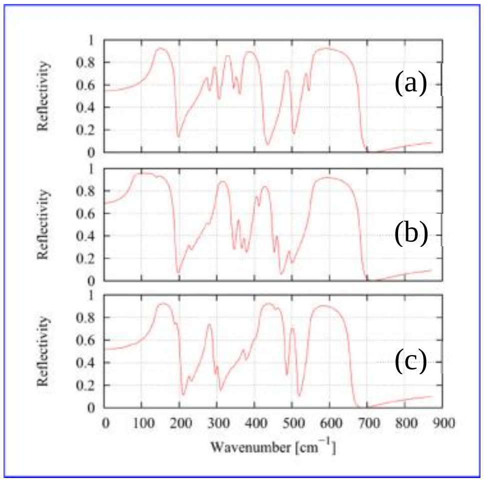

Figure 5-7: IR reflectance spectrum of $BiVO_3$ calculated along three different axes a, b and c, as notated in the figure. The oscillator strengths are normalized to unity. The damping factor is set to 9 cm^{-1} and the angle of incidence is kept as 10 degrees.

Table 5-VI: Calculated IR and Raman active vibrational modes are provided in cm^{-1}. Longitudinal optical modes (LO), transverse optic modes (TO) as well as the LO-TO splitting are given. Modes are separated according to the symmetry (AU, BU, AG and BG)

	AU (IR)			BU (IR)	AG	BG (Raman)
	LO (cm^{-1})	TO(cm^{-1})	LO-TO (cm^{-1})	LO (cm^{-1})	(Raman) LO (cm^{-1})	LO (cm^{-1})
1	65.1	65.2	0.1	77.0	60.5	77.3
2	90.3	90.4	0.1	88.8	85.9	109.6
3	134.7	193.8	59.1	138.8	107.1	131.4
4	175.9	175.6	-0.3	188.0	227.4	216.5
5	226.7	226.9	0.2	227.1	257.0	242.9
6	267.1	268.6	1.5	274.5	288.7	317.4
7	272.9	278.3	5.4	300.3	321.2	330.8
8	290.9	303.2	12.2	340.4	381.1	374.5
9	319.4	679.4	360	354.2	400.9	467.3
10	348.1	343.3	-4.8	371.5	449.8	483.7
11	355.4	354.1	-1.3	400.2	470.6	631.6
12	367.2	359.5	-7.7	414.7	670.7	637.6
13	428.7	424.2	-4.5	456.1		
14	479.4	431.1	-48.2	492.5		
15	527.3	528.6	1.2	545.2		
16	532.8	500.9	-31.9	551.7		
17	549.5	542.9	-6.6			

5.3.5 Magnetic properties

An analysis on the atomic integrated spin density of the $BiVO_3$ crystal at its ferromagnetic state is provided in Table 5-VII. The nominal spin density on the vanadium atoms, i.e., 1.980 μ_B (V1) and 1.959 μ_B (V2) are close to its ideal d^2 spin state. The small difference in the atomic spin densities of V1 and V2 vanadium atoms are attributed to the slight difference in the strength of their covalent bonding with oxygen atoms. The atomic spin density map in the (110) and (010) planes are plotted in Fig. 5-8. As can be seen from the figure, most of the spin density is centred on the V sites. A non-negligible spin density is, however, present both at the oxygen and the Bi sites (not shown). At the oxygen site, two variations of spin density can be seen. Firstly, the negative spin corresponds to the delocalization of V-3*d* charge towards the oxygen sublattice due to the comparatively small V1-O1-V2 and V1-O3-V3 bond distance. Delocalization of charge towards the oxygen atoms induces an opposite polarization at the O1 and O3 oxygen sites, as a direct consequence of the hybridization between the vanadium and oxygen atoms (O1 and O3). This further substantiates the much higher Mulliken population density of V1-O1 (0.039 |e|), V2-O1 (0.038 |e|), V1-O3 (0.037 |e|), and V2-O3 (0.040 |e|) bond given in Table 5-II. On the other hand, the spin density at the O2 oxygen is slightly positive (+0.13 μ_B). Due to the comparatively larger distance between the vanadium atoms (V1-O2-V2) in the **a-c** plane (see Table 5-III), the charge density around the oxygen atom accumulates close to the nucleus. As a consequence, a slightly higher positive spin density will result in at the oxygen site. This can be seen from the spin density plot in the (010) plane given in Fig. 5-8. As a result of this, the hybridization between vanadium and O2 atoms is comparatively weaker. This weaker hybridization can be further inferred from the low bond population of 0.027 |e| and 0.034 |e| for the V1-O1 and V2-O2 bonds respectively, as shown in Table 5-III. However, the spin density at the oxygen sites is smaller than the Bi site, indicating a weak super exchange interaction between the neighbouring V- atoms across oxygen. Strong super exchange interactions normally stabilize the AFM states and hence our finding on the relative stability of FM structure over the AFM structures is reinforced. The high value of spin density at the Bi site (0.036 μ_B) is attributed to the highly localized lone pair electrons giving rise to a strong negative bond population of Bi atoms (-0.069 |e|, -0.064 |e| and -0.089 |e|) with the oxygen-atoms.

Table 5-VII: Atomic spin density of all the irreducible atoms. The units are given in Bohr magnetons (μ_B)

Atom	Atomic spin (μ_B)
Bi	0.036
V1	1.980
V2	1.959
O1	-0.009
O2	0.013
O3	-0.010

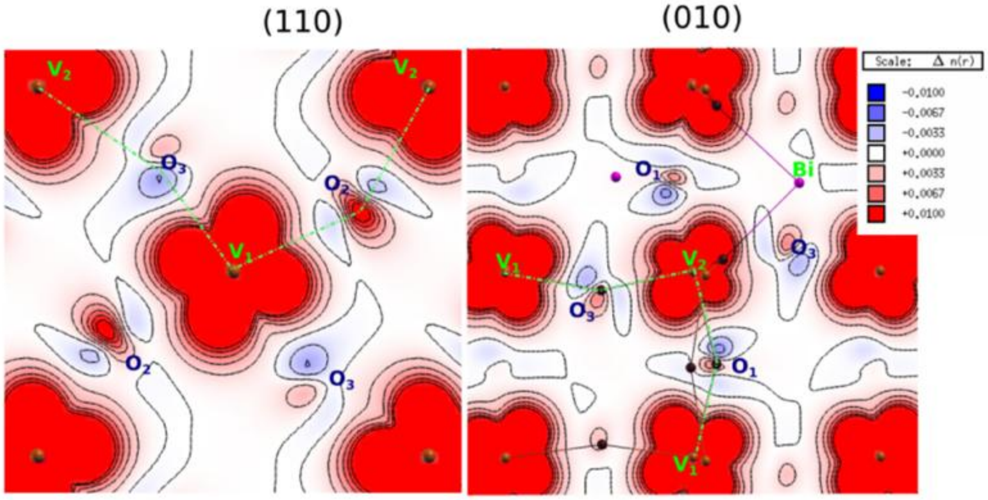

Figure 5-8: Atomic spin density map of ferromagnetic $BiVO_3$ in the (110) and (010) planes. Irreducible O, V and Bi atoms are notated. Bondings in the considered plane are marked via dashed green lines. Nine contours are drawn from -0.01 to +0.01 |e|/bohr^3. Red portion represents portion with higher spin density.

5.4 Summary

Spin polarized density functional calculations were used for calculating the total energy of the $BiVO_3$ crystal symmetry that was predicted by the *SPuDs* software. The orthorhombic *Pnma* structure in its ferromagnetic state is found to be far more stable than the cubic aristotype. Although the electronic transition is found to be indirect in nature with a gap of 1.75 eV, a direct band gap of 1.96 eV is calculated at the gamma point. Since this value lies in the visible region of the spectra the material is expected to be a good candidate for visible light driven photocatalytic applications. The valence and conduction bands are highly dispersed and thus one could anticipate that this material will have excellent charge transport properties. The phonon frequencies at the centre of the Brillouin zone are simulated. No unstable soft modes are identified and thus the dynamical stability of the material is confirmed. The simulated IR and Raman modes are provided and we believe that the simulated IR and Raman spectra could be a guideline for future experiments. The system keeps its centrosymmetry and, hence, no ferroelectricity is identified in the present crystal structure.

6 CONCLUSIONS

Green and sustainable energy production has become demanding due to the increase in the population growth and environmental requirements. An elegant pathway to achieve this goal is to convert solar energy into a storable form such as hydrogen (H_2). As a clean and efficient carrier of energy, hydrogen can be produced from water using a semiconductor photocatalyst in the presence of sunlight. A photocatalyst that would carry out the aforementioned conversion process, however, has to meet certain stringent requirements. To date, no single candidate has shown reasonable solar to hydrogen conversion efficiency.

The principle aim of the thesis was to tune the electronic band structure of few potentially applicable photocatalysts as well as to model a novel photocatalyst. The tuning of the electronic properties to optimize their solar to hydrogen conversion efficiency was carried out in two different ways namely by solid solution formation and by applying external electric field.

Solid solution formation:

A density functional study on the modulation of the electronic properties of hematite by making a solid solution with Cr_2O_3 and Al_2O_3 has been performed using the B3LYP hybrid functional. Twelve different compositions within the solubility limit are studied. All the compositions are found stable with corundum structure. The presence of Cr and Al in the Fe sublattice influences the electronic properties of hematite. With the increase in the Cr_2O_3 content, the nature of the valence band is altered. There is an increase in the valence band width together with a reduction in the band gap value. The principal reason for the reduction in the band gap values is an upshift in the valence band edge. Conversely, the downward shift in the conduction band edge is not very prominent. In addition, a widening of the valence band width should, in principle, enhance the charge transfer kinetics of holes by suppressing the recombination. Finally, as the percentage of Al_2O_3 in the system increases, the unit cell volume reduces linearly due to the strain induced. In addition, close packing, induced by the strain, reduces the Fe-Fe distance (0.05 Å on an average) in the (001) plane, allowing an extended mixing of Fe-3*d* orbitals. Such mixing of orbitals disperses the bands further and increases the hopping probability.

Overall, a solid solution of Fe_2O_3-Cr_2O_3-Al_2O_3 can be considered as a good photocatalyst with respect to pure hematite due to the following observations,

- An increased valence band width indicates higher charge carrier kinetics of holes. An improvement in the diffusion length for the holes and reduced recombination probability are expected.
- A reduction in the band gap value enhances the visible light absorption.
- Reduced Fe-Fe distances along (001) plane will promote the hopping probability of charge carriers. This might improve the conductivity in the (001) plane, especially for electrons.

By contrast, reducing the Fe_2O_3 percentage in the ternary system below 50% is not suggested as it facilitates the carrier recombination due to narrowing of the conduction bands as well as strong localization of the *d* bands at the top of valence band.

Applying external electric field:

The finite field sawtooth model has been employed within different levels of theory (LDA, GGA, and HYBRID) to model the effect of electric field. First we performed our calculation on a series of prototypical crystals from the alkali halide family, namely LiF, LiCl, NaF, NaCl, KF, and KCl. A dramatic change in the band gap value and the band width of these crystals is observed in the presence of the external electric field. The principle reason of the red shift in the band gap value is the delocalization of the states associated with a particular level to the levels in its neighboring layers. An internal structural relaxation of 0.07 Å is observed for 0.01 a.u. field. The effect of the relaxation on the electronic bang gap is rather negligible. We have also calculated the breakdown strength of these crystals using a general equation proposed by Callen.

Later, we extended the method to two typical UV photoactive materials with NaCl type crystal structure. We found that the effect of electric field on AgCl and AgBr are almost similar to NaCl. The reduction in the band gap value, with the increase in the electric field is much faster in the case of AgCl and AgBr. This is because the charge density in AgCl and AgBr extends up to two neighboring layers. We also found that, unlike the alkali halides the effective mass ratio plays a key role in determining the breakdown strength in the case of correlated systems like AgCl and AgBr.

The effect of external electric field on the structural and electronic properties of wide band gap materials can be summarized:

- In the presence of an electric field, there is a considerable red shift. In the case of AgCl, the shift is ~1 eV in the presence of 0.01 a.u. field. This is very beneficial to tune the band gap of wide band gap materials towards visible light.
- A band widening is a clear indication of enhanced carrier kinetics. This can be effectively utilized in the case of indirect band gap semiconductors as they need a much wider band to absorb the major portion of the incident light.
- The dielectric strength of wide band gap materials can be calculated effectively using a productive functional (accurate dielectric constants).
- For accurate calculation of breakdown strength, numerically calculated effective mass ratio has to be introduced.

Since external electric field can be used to tune the electronic properties, an experimental setup for the present purpose has to be modeled with particular attention. In addition, the validity of the present model beyond NaCl type crystal still has to be tested.

Modeling of a novel photocatalyst:

Inspired from the capability of Bi and V based materials as photocatalysts, we have modeled a novel semiconductor, $BiVO_3$, with perovskite structure. The material is found stable with ferromagnetic *Pnma* structure. No soft modes have been identified in the vibrational frequency spectrum. Thus the dynamical stability of the crystal is confirmed. A full characterization of the structural, electronic and magnetic properties is reported. A complete analysis of the IR and Raman modes are presented, which would guide the experimentalists to synthesize this material. A direct band gap of 1.96 eV is calculated and this, indeed, falls in the visible region of the spectra. From the band structure plots, it has been identified that the bands are well dispersed due to a strong covalent bonding between the vanadium and oxygen atoms. The width of the valence band is almost 8.2 eV. The Born effective charges are calculated at the Bi-site.

From the above observations, we could anticipate that $BiVO_3$ can be a very promising photocatalyst. Its main properties as a photocatalyst can be summarized as follows

- A low band gap value indicates a good visible light absorption.
- The band gap is direct; shows a large absorption coefficient.
- A large band width indicates reduced recombination rate and faster charge transfer kinetics.
- Highly dispersed bands indicate low effective mass for charge carriers and thus higher mobility.
- Highly anomalous Born effective charges brings large dielectric constant value and perhaps a spontaneous polarization in a low symmetry structure.

Future perspectives:

- Modeling of the effect of electric field on the electronic properties of non NaCl type crystals.
- Ferroelectric distortion in $BiVO_3$ and multiferroicity.

7 SCIENTIFIC CONTRIBUTIONS

- Results presented in Chapter 3 were published in Journal of Computational Materials Science.

1. C.S Praveen, V Timon, M. Valant; *Electronic band gaps of ternary corundum solid solutions from* Fe_2O_3-Cr_2O_3-Al_2O_3 *system for photocatalytic applications: a theoretical study*. Comp. Mater. Sci., **55**, 192-198 (2012).

- First part of Chapter 4 was published in Journal of Computational Materials Science.

2. C.S. Praveen, A. Kokalj, M. Valant: *B3LYP investigation of response properties of alkali halides on external static electric fields.* Comp. Mater. Sci., **50**, 2628-2635 (2011).

- The second part of Chapter 4 is summarized and submitted to Journal of Solid State Sciences.

3. C.S. Praveen, A. Kokalj, M. Rerat, M. Valant: *Response Properties of AgCl and AgBr under an External Static Electric Field: A Density Functional Study*. **Submitted** to J. Solid State Sci. (2012).

- The Results of Chapter 5 will be submitted as two papers.

4. C.S. Praveen, A.Kokalj, V. Timon, M.Valant: *Dynamical, magnetic and optoeletronic properties of a novel Bi-based perovskite structure,* $BiVO_3$*: A density functional characterization.* **Will be submitted** (2012).
5. M. Dragomir, C.S. Praveen, I. Arčon, M.Valant: *Structural stability of* $BiVO_3$*: An experimental and theoretical investigation*. **Will be submitted** (2012).

- Additional scientific contributions from external collaborations include:

6. V. Timon, C.S Praveen, M. Cobian, E. Escamilla-Roa, M.P. de Lara-Castells, M. Valant: *Hybrid Density Functional Based Study on the Band Structure of Trioctahedral Mica and its Dependence on the Variation of* Fe^{2+} *Content*. **Submitted** to J. Phys. Cond. Mater (2012).

8 APPENDIX

Basis set used for different atoms in the present study

Fe: (8-6411(41d)

```
0 0 8 2.0  1.0
 315379.0      0.000227
  45690.0      0.0019
   9677.3      0.0111
   2520.88     0.0501
    759.746    0.1705
    262.964    0.36924
    102.801    0.4033
     42.9733   0.1434
0 1 6 8.0 1.0
    798.262   -0.0052   0.00850
    191.162   -0.068    0.0608
     63.6885  -0.1314   0.2114
     25.3625   0.2517   0.3944
     10.7338   0.6433   0.398
      3.764    0.2825   0.2251
0 1 4 8.0 1.0
     48.1434   0.0122  -0.0215
     17.4579  -0.2278  -0.085
      6.9972  -0.8801   0.201
      3.0791   0.9755   1.3024
0 1 1 0.0 1.0
     1.3137   1.0      1.0
0 1 1 0.0 1.0
      0.5625   1.0      1.0
0 3 4 5.0 1.0
     30.4821   0.0583
      8.692    0.2591
      3.1008   0.5162
      1.1709   0.5656
0 3 1 0.0 1.0
      0.4298   1.0
```

Cr: 8-6411(41d)

```
24 7
0 0 8 2.0 1.0
  235200.0       0.00027
   35040.0       0.00211
    7806.0       0.01139
    2134.0       0.0486
     669.2       0.1591
     235.9       0.3555
      90.52      0.4231
      35.88      0.1482
0 1 6 8.0 1.0
     735.0      -0.00473  0.00843
     176.1      -0.0593   0.061
      57.65     -0.1353   0.2304
      21.84      0.2375   0.4743
       8.987     0.6731   0.4606
       3.460     0.2487   0.1696
0 1 4 8.0 1.0
      33.84      0.011   -0.0279
      11.72     -0.4207  -0.0812
       5.414    -0.8673   0.2211
       2.502     0.9675   1.033
0 1 1 0.0 1.0
      1.1590  1.0      1.0
0 1 1 0.0 1.0
       0.5035 1.0      1.0
0 3 4 3.0 1.0
      30.57      0.03077
       8.403     0.1604
       2.834     0.3907
       1.002     0.4788
0 3 1 0.0 1.0
       0.3538   1.0
```

Al: 8-511(1d)

```
0 0 8 2.0 1.0
 78327.6     0.000226
 11286.3     0.00191
  2395.35    0.01105
   622.594   0.05005
   187.553   0.16845
    64.705   0.3653
    25.1558  0.40221
    10.4417  0.14897
0 1 5 8.0 1.0
   155.2    -0.0073 0.0097
    36.7751 -0.0758 0.0648
    12.0363 -0.088  0.212
     4.6156  0.2976 0.3769
     1.9408  0.6067 0.3865
0 1 1 0.0 1.0
     0.781  1.0    1.0
0 1 1 0.0 1.0
     0.4171  1.0    1.0
0 3 1 0. 1.
     0.60357   1.        1.
```

O: 8-411(1d)

```
0 0 8 2.0 1.0
 8020.0       0.00108
 1338.0       0.00804
  255.4       0.05324
   69.22      0.1681
   23.90      0.3581
    9.264     0.3855
    3.851     0.1468
    1.212     0.0728
0 1 4 8.0 1.0
   49.43     -0.00883    0.00958
   10.47     -0.0915     0.0696
    3.235    -0.0402     0.2065
    1.217     0.379      0.347
0 1 1 0.0 1.0
   0.500 (0.479)*    1.0        1.0
0 1 1 0.0 1.0
   0.191 (0.221)*    1.0        1.0
0 3 1 0.0 1.0
   0.500 (0.371)*     1.0
```

*Used for Fe-Cr-Al ternary system

V: 8-6411(31d)

```
0 0 8 2.0 1.0
 246297.0     0.000228
  35328.3     0.001929
   7524.86    0.0111
   1969.96    0.0500
    594.016   0.1699
    205.385   0.3687
     80.1571  0.4038
     33.218   0.1440
0 1 6 8.0 1.0
    611.206  -0.0058  0.0086
    146.715  -0.0675  0.0607
     48.724  -0.1278  0.2123
     19.2296  0.2508  0.3966
      8.1086  0.6301  0.4076
      2.8353  0.2781  0.217
0 1 4 8.0 1.0
     31.5966  0.0175 -0.0274
     12.7943 -0.2515 -0.0928
      5.1332 -0.9153  0.2146
      2.2534  0.9818  1.5909
0 1 1 0.0 1.0
      0.9655  1.0     1.0
0 1 1 0.0 1.0
      0.4096  1.0     1.0
0 3 3 2.0 1.0
      16.79   0.05975
      4.372   0.26822
      1.326   0.51315
0 3 1 0.0 1.0
      0.36  0.45636
```

F: 7-311(1d)

```
0 0 7 2.0 1.0
 13770.0    0.000877
  1590.0    0.00915
   326.5    0.0486
    91.66   0.1691
    30.46   0.3708
    11.50   0.41649
     4.76   0.1306
0 1 3 8.0 1.0
    19.000 -0.1094 0.1244
     4.530 -0.1289 0.5323
     1.387  1.0    1.0
0 1 1 0.0 1.0
    0.409 1.0    1.0
0 1 1 0.0 1.0
    0.128 1.0    1.0
0 3 1 0.0 1.0
    0.478 1.0
```

Bi: HAYWLC

```
0 0 3 2.  1.
  0.574400  -1.360422
  0.385100   1.5862740
  0.105000    0.6266090
0 2 3 0. 1.
  0.910500  -0.1188660
  0.219400   0.6064640
  0.074550   0.5241060
0 0 1 0. 1
   0.09   1.0
0 2 1 0. 1
  0.15      1.0
0 3 1 0. 1
  0.30      1.0
```

Li: 5-11(1d)

```
3  4
0 0  5  2.  1.
840.0    0.00264
217.5    0.00850
 72.3    0.0335
 19.66   0.1824
  5.044  0.6379
0 1 1  0.  1.
  1.357  1.0    1.0
0 1 1  0.  1.
  0.367  1.0    1.0
0 3 1  0.  1.
   0.44  1.0
```

Na: 8-511(1d)

```
0 0 8 2.0 1.0
 56700.0   0.000225
  8060.0   0.00191
  1704.0   0.01105
   443.6   0.05006
   133.1   0.1691
    45.8   0.3658
    17.75  0.3998
     7.38  0.1494
0 1 5 8.0 1.0
   119.0  -0.00673 0.00803
    25.33 -0.0798  0.0639
     7.80 -0.0793  0.2074
     3.00  0.3056  0.3398
     1.289 0.5639  0.3726
0 1 1 0.0 1.0
     0.539 1.0     1.0
0 1 1 0.0 1.0
     0.376 1.0     1.0
0 3 1 0.0 1.0
     0.5    1.0
```

Ag: (9-766-311(41d)

```
0 0 9 2.0 1.2611
  2288090.0      0.0000488
   341566.0      0.000384
    73992.5      0.00225
    18814.5      0.0112
     5396.99     0.0466
     1713.64     0.1557
      605.653    0.3518
      239.056    0.4262
       99.5792   0.1824
0 1 7 8.0 1.305
     6189.44    -0.000297   0.00104
     1429.72    -0.00641    0.00958
      436.118   -0.0546     0.0568
      153.621   -0.1473     0.2186
       61.1694   0.1543     0.4557
       27.6797   0.6284     0.4277
       13.1763   0.3887     0.1678
0 1 6 8.0 1.3888
      117.917    0.0064    -0.0144
       45.6255  -0.0354    -0.0695
       19.2559  -0.3267     0.0428
        8.5052   0.0399     0.885
        3.9101   0.9503     1.2813
        1.8065   0.381      0.3893
0 3 6 10.0 1.0
      323.345    0.0117
       96.312    0.0825
       35.8605   0.2757
       14.7319   0.4603
        6.3294   0.3518
        2.5577   0.0712
0 1 3 8.0 1.0
        5.9759  -4.2389    -0.0662
        2.738    1.4818     0.5457
        1.2022   9.9774     0.9258
0 1 1 0.0 1.0
        0.45533  1.0        1.0
0 1 1 0.0 1.0
        0.10869    1.0       1.0
0 3 4 10.0 1.0
       11.2183   0.0146
        4.1818   0.1881
        1.7211   0.4839
        0.679    0.4861
0 3 1 0.0 1.0
        0.22670 1.0
```

Br: (9-76311(51d)

```
0 0 9 2.0 1.0
2275090.0    0.000038
 319959.0    0.0003344
  64974.1    0.0021238
  15718.0    0.011193
   4347.15  0.047900
   1367.7    0.157400
    483.334  0.352332
    187.066  0.423303
     75.1333 0.153645
0 1 7 8.0 1.0
5241.62      -0.000373    0.0009764
1192.97      -0.0072305   0.0092853
 354.263     -0.061887    0.056735
 121.56      -0.145788    0.218068
  46.765      0.246071    0.447931
  19.7469     0.712463    0.395229
   8.44148    0.239375   0.09678
0 1 6 8.0 1.0
103.375       0.0039064   -0.014826
 36.4438     -0.054067    -0.071387
 15.4097     -0.323251     0.116639
  6.326       0.264172     0.970063
  2.62943     0.954686     1.21262
  1.04921     0.236846     0.328426
0 1 3 8.0 1.0
 2.902 -0.5623      -2.8377
 3.0655      54.7218      3.6827
 1.2007      17.3864      0.4607
0 1 1 0.0 1.0
 0.54366     1.0    1.0
0 1 1 0.0 1.0
 0.16404     1.0    1.0
0 3 5 10.0 1.0
202.635           0.005270
 59.7021            0.04036
 21.5166            0.162038
  8.3345            0.368724
  3.15228           0.46438
0 3 1 0.0 1.0
   0.96344   1.0
```

Cl: 8-6311(1d)

```
0 0 8 2.0 1.0
135320.0    0.000225
 19440.0    0.00191
  4130.0    0.01110
  1074.0    0.04989
   323.4    0.1703
   111.1    0.3683
    43.4    0.4036
    18.18   0.1459
0 1 6 8.0 1.0
   324.8   -0.00763 0.00820
    73.00  -0.0829  0.0605
    23.71  -0.1046  0.2115
     9.138  0.2540  0.3765
     3.930  0.695   0.3967
     1.329  0.399   0.186
0 1 3 8.0 1.0
     4.755 -0.3740 -0.0340
     1.756 -0.4754  0.1617
     0.785  1.3400  0.9250
0 1 1 0.0 1.0
     0.313 1.0     1.0
0 1 1 0.0 1.0
     0.121  1.0     1.0
0 3 1 0.0 1.0
     0.193  1.0
```

K: 8-6511(31)

```
 0 0 8 2.0 1.0
 172500.0    0.000220
  24320.0    0.00192
   5140.0    0.01109
   1343.9    0.04992
    404.5    0.1702
    139.4    0.3679
     54.39   0.4036
     22.71   0.1459
0 1 6 8.0 1.0
    402.0   -0.00603 0.00841
     93.5   -0.0805  0.0602
     30.75  -0.1094  0.2117
     11.92   0.258   0.3726
      5.167  0.684   0.4022
      1.582  0.399   0.186
0 1 5 8.0 1.0
     17.35  -0.0074 -0.0321
      7.55  -0.129  -0.062
      2.939 -0.6834  0.1691
      1.19   1.08    1.500
      0.674  1.03    1.060
0 1 1 0.0 1.0
      0.373  1.0     1.0
0 1 1 0.0 1.0
      0.217 1.0     1.0
0 3 3 0.0 1.0
      3.94   0.160
      1.072  0.313
      0.394  0.406
0 3 1 0.0 1.0
      0.1  1.0
```

9 BIBLIOGRAPHY

1. Walter, M.G., E.L. Warren, J.R. McKone, S.W. Boettcher, *et al.*, *Solar Water Splitting Cells.* Chemical Reviews, 2010. **110**(11): p. 6446-6473.
2. Lewis, N.S., *Toward cost-effective solar energy use.* Science, 2007. **315**(5813): p. 798-801.
3. Hanjalic, K., R. van de Krol, and A. Lekić, *Sustainable energy technologies: options and prospects*, 2008: Springer Verlag, Dordrecht, The Netherlands.
4. Bolton, J.R., S.J. Strickler, and J.S. Connolly, *Limiting and realizable efficiencies of solar photolysis of water.* Nature, 1985. **316**(6028): p. 495-500.
5. James R, B., *Solar photoproduction of hydrogen: A review.* Solar Energy, 1996. **57**(1): p. 37-50.
6. Bard, A.J. and M.A. Fox, *Artificial Photosynthesis: Solar Splitting of Water to Hydrogen and Oxygen.* Accounts of Chemical Research, 1995. **28**(3): p. 141-145.
7. Grimes, C.A., O.K. Varghese, and S. Ranjan, *Light, Water, Hydrogen: The Solar Generation of Hydrogen by Water Photoelectrolysis.* 2008: Springer, New York, USA.
8. Fujishima, A. and K. Honda, *Electrochemical Photolysis of Water at a Semiconductor Electrode.* Nature, 1972. **238**(5358): p. 37-38.
9. Kiwi, J. and M. Gratzel, *Heterogeneous Photocatalysis - Enhanced H_2 Production in TiO_2 Dispersions under Irradiation - the Effect of Mg Promoter at the Semiconductor Interface.* Journal Of Physical Chemistry, 1986. **90**(4): p. 637-640.
10. Gratzel, M., *Photocatalysis with Colloidal Semiconductor Particles.* Journal Of The Electrochemical Society, 1983. **130**(3): p. C124-C125.
11. Maeda, K., *Photocatalytic water splitting using semiconductor particles: History and recent developments.* Journal of Photochemistry and Photobiology C: Photochemistry Reviews, 2011. **12**(4): p. 237-268.

12. Heller, A., *Hydrogen-Evolving Solar Cells.* Science, 1984. **223**(4641): p. 1141-1148.
13. Osterloh, F.E., *Inorganic Materials as Catalysts for Photochemical Splitting of Water.* Chemistry of Materials, 2007. **20**(1): p. 35-54.
14. Osterloh, F.E. and B.A. Parkinson, *Recent developments in solar water-splitting photocatalysis.* MRS Bulletin, 2011. **36**(01): p. 17-22.
15. Scaife, D.E., *Oxide semiconductors in photoelectrochemical conversion of solar energy*. Solar Energy, 1980. **25**(1): p. 41-54.
16. Lewis, N.S., *Chemical Control of Charge Transfer and Recombination at Semiconductor Photoelectrode Surfaces.* Inorganic Chemistry, 2005. **44**(20): p. 6900-6911.
17. Hoffmann, M.R., S.T. Martin, W. Choi, and D.W. Bahnemann, *Environmental Applications of Semiconductor Photocatalysis.* Chemical Reviews, 1995. **95**(1): p. 69-96.
18. Kazuhiko, M., *Photocatalytic water splitting using semiconductor particles: History and recent developments.* Journal of Photochemistry and Photobiology C: Photochemistry Reviews, 2011. **12**(4): p. 237-268.
19. Ryu, A., *Recent progress on photocatalytic and photoelectrochemical water splitting under visible light irradiation.* Journal of Photochemistry and Photobiology C: Photochemistry Reviews, 2010. **11**(4): p. 179-209.
20. Bolton, J.R. and D.O. Hall, *Photochemical Conversion and Storage of Solar Energy.* Annual Review of Energy, 1979. **4**(1): p. 353-401.
21. Rajeshwar, K., *Hydrogen generation at irradiated oxide semiconductor–solution interfaces.* Journal of Applied Electrochemistry, 2007. **37**(7): p. 765-787.
22. Van De Krol, R. and M. Grätzel, *Photoelectrochemical Hydrogen Production*. 2011: Springer Verlag, Heidelberg, London, UK.
23. Maeda, K. and K. Domen, *Photocatalytic Water Splitting: Recent Progress and Future Challenges.* The Journal of Physical Chemistry Letters, 2010. **1**(18): p. 2655-2661.
24. Beydoun, D., R. Amal, G. Low, and S. McEvoy, *Role of Nanoparticles in Photocatalysis.* Journal of Nanoparticle Research, 1999. **1**(4): p. 439-458.

25. Best, J.P. and D.E. Dunstan, *Nanotechnology for photolytic hydrogen production: Colloidal anodic oxidation.* International Journal of Hydrogen Energy, 2009. **34**(18): p. 7562-7578.

26. Martin, R.M., *Electronic structure: basic theory and practical methods*, 2004: Cambridge, UK.

27. Kudo, A. and Y. Miseki, *Heterogeneous photocatalyst materials for water splitting.* Chemical Society Reviews, 2009. **38**(1): p. 253-78.

28. Navarro Yerga, R.M., M.C. Álvarez Galván, F. del Valle, J.A. Villoria de la Mano*, et al.*, *Water Splitting on Semiconductor Catalysts under Visible-Light Irradiation.* ChemSusChem, 2009. **2**(6): p. 471-485.

29. Kudo, A., *Development of photocatalyst materials for water splitting.* International Journal of Hydrogen Energy, 2006. **31**(2): p. 197-202.

30. Navarro, R.M., M.C. Alvarez-Galvan, J.A. Villoria de la Mano, S.M. Al-Zahrani, *et al.*, *A framework for visible-light water splitting.* Energy & Environmental Science, 2010. **3**(12).

31. Ni, M., M.K.H. Leung, D.Y.C. Leung, and K. Sumathy, *A review and recent developments in photocatalytic water-splitting using for hydrogen production.* Renewable and Sustainable Energy Reviews, 2007. **11**(3): p. 401-425.

32. Hashimoto, K., H. Irie, and A. Fujishima, *TiO_2 Photocatalysis: A Historical Overview and Future Prospects.* Japanese Journal Of Applied Physics, 2005. **44**(12): p. 8269-8285.

33. Santato, C., M. Ulmann, and J. Augustynski, *Photoelectrochemical Properties of Nanostructured Tungsten Trioxide Films.* The Journal of Physical Chemistry B, 2001. **105**(5): p. 936-940.

34. Sivula, K., F. Le Formal, and M. Grätzel, *Solar Water Splitting: Progress Using Hematite (α-Fe_2O_3) Photoelectrodes.* ChemSusChem, 2011. **4**(4): p. 432-449.

35. Program, U.N.d., *World Energy Assesment Report : Energy and the challende of Sustainability*, 2003: United Nations, New York, USA

36. Kudo, A., K. Omori, and H. Kato, *A Novel Aqueous Process for Preparation of Crystal Form-Controlled and Highly Crystalline $BiVO_4$ Powder from Layered Vanadates at Room Temperature and Its Photocatalytic and*

Photophysical Properties. Journal of the American Chemical Society, 1999. **121**(49): p. 11459-11467.

37. Li, Y., J. Du, S. Peng, D. Xie, *et al.*, *Enhancement of photocatalytic activity of cadmium sulfide for hydrogen evolution by photoetching.* International Journal of Hydrogen Energy, 2008. **33**(8): p. 2007-2013.
38. Aldana, J., Y.A. Wang, and X. Peng, *Photochemical Instability of CdSe Nanocrystals Coated by Hydrophilic Thiols.* Journal of the American Chemical Society, 2001. **123**(36): p. 8844-8850.
39. Vučemilović, M.I., N. Vukelić, and T. Rajh, *Solubility and photocorrosion of small CdS particles.* Journal of Photochemistry and Photobiology A: Chemistry, 1988. **42**(1): p. 157-167.
40. Shaban, Y.A. and S.U.M. Khan, *Visible light active carbon modified n-TiO_2 for efficient hydrogen production by photoelectrochemical splitting of water.* International Journal of Hydrogen Energy, 2008. **33**(4): p. 1118-1126.
41. Mahajan, V.K., S.K. Mohapatra, and M. Misra, *Stability of TiO_2 nanotube arrays in photoelectrochemical studies.* International Journal of Hydrogen Energy, 2008. **33**(20): p. 5369-5374.
42. Wan, Q., Q.H. Li, Y.J. Chen, T.H. Wang, *et al.*, *Positive temperature coefficient resistance and humidity sensing properties of Cd-doped ZnO nanowires.* Applied Physics Letters, 2004. **84**(16): p. 3085-3087.
43. Valdes, A., J. Brillet, M. Gratzel, H. Gudmundsdottir, *et al.*, *Solar hydrogen production with semiconductor metal oxides: new directions in experiment and theory.* Physical Chemistry Chemical Physics, 2012. **14**(1): p. 49-70.
44. Liu, W., Y.H. Zhao, J. Nguyen, Y. Li, *et al.*, *Electric field induced reversible switch in hydrogen storage based on single-layer and bilayer graphenes.* Carbon, 2009. **47**(15): p. 3452-3460.
45. Sun, X., J.-Y. Hwang, and S. Shi, *Hydrogen Storage in Mesoporous Metal Oxides with Catalyst and External Electric Field.* Journal of Physical Chemistry C, 2010. **114**(15): p. 7178-7184.
46. Kato, H. and A. Kudo, *Water Splitting into H_2 and O_2 on Alkali Tantalate Photocatalysts ATaO3 (A = Li, Na, and K).* The Journal of Physical Chemistry B, 2001. **105**(19): p. 4285-4292.

47. Liu, H., J. Yuan, Z. Jiang, W. Shangguan, *et al.*, *Novel photocatalyst of V-based solid solutions for overall water splitting.* Journal of Materials Chemistry, 2011. **21**(41): p. 16535-16543.

48. Gross, E.K.U. and R.M. Dreizler, *Density functional theory*, 1995: Springer, New York, USA.

49. Hohenberg, P. and W. Kohn, *Inhomogeneous Electron Gas.* Physical Review, 1964. **136**(3B): p. B864.

50. Thomas, L.H., *The calculation of atomic fields.* Mathematical Proceedings of the Cambridge Philosophical Society, 1927. **23**(05): p. 542-548.

51. Fávaro, A.P., K. Capelle, and J.V. Batista Ferreira, *Construction of model dielectric functions for two- and three-dimensional electron liquids from density functionals.* Physical Review B, 2006. **73**(4): p. 045133.

52. Levy, M., *Electron densities in search of Hamiltonians.* Physical Review A, 1982. **26**(3): p. 1200-1208.

53. Kohn, W. and L.J. Sham, *Self-Consistent Equations Including Exchange and Correlation Effects.* Physical Review, 1965. **140**(4A): p. A1133.

54. Perdew, J.P. and Y. Wang, *Accurate and simple analytic representation of the electron-gas correlation energy.* Physical Review B, 1992. **45**(23): p. 13244-13249.

55. Carr, W.J., Jr. and A.A. Maradudin, *Ground-State Energy of a High-Density Electron Gas.* Physical Review, 1964. **133**(2A): p. A371-A374.

56. Ceperley, D.M. and B.J. Alder, *Ground State of the Electron Gas by a Stochastic Method.* Physical Review Letters, 1980. **45**(7): p. 566-569.

57. Becke, A.D., *Density-functional thermochemistry. II. The effect of the Perdew–Wang generalized-gradient correlation correction.* Journal of Chemical Physics, 1992. **97**(12): p. 9173.

58. Becke, A.D., *Density-functional thermochemistry. I. The effect of the exchange-only gradient correction.* Journal of Chemical Physics, 1992. **96**(3): p. 2155.

59. Jensen, F., *Introduction to Computational Chemistry*, 1999: John Wiley & Sons Ltd, Chichester, UK.

60. Perdew, J.P., M. Ernzerhof, and K. Burke, *Rationale for mixing exact exchange with density functional approximations.* Journal of Chemical Physics, 1996. **105**(22): p. 9982-9985.
61. Becke, A.D., *Density-functional exchange-energy approximation with correct asymptotic behavior.* Physical Review A, 1988. **38**(6): p. 3098-3100.
62. Lee, C., W. Yang, and R.G. Parr, *Development of the Colle-Salvetti correlation-energy formula into a functional of the electron density.* Physical Review B, 1988. **37**(2): p. 785-789.
63. Becke, A.D., *Density-functional thermochemistry. III. The role of exact exchange.* Journal of Chemical Physics, 1993. **98**(7): p. 5648-5652.
64. Becke, A.D., *Density-functional thermochemistry. IV. A new dynamical correlation functional and implications for exact-exchange mixing.* Journal of Chemical Physics, 1996. **104**(3): p. 1040.
65. Becke, A.D., *Density-functional thermochemistry. V. Systematic optimization of exchange-correlation functionals.* Journal of Chemical Physics, 1997. **107**(20): p. 8554.
66. Becke, A.D., *A new mixing of Hartree--Fock and local density-functional theories.* Journal of Chemical Physics, 1993. **98**(2): p. 1372-1377.
67. Bilc, D.I., R. Orlando, R. Shaltaf, G.M. Rignanese, *et al.*, *Hybrid exchange-correlation functional for accurate prediction of the electronic and structural properties of ferroelectric oxides.* Physical Review B, 2008. **77**(16): p. 165107.
68. Goffinet, M., P. Hermet, D.I. Bilc, and P. Ghosez, *Hybrid functional study of prototypical multiferroic bismuth ferrite.* Physical Review B, 2009. **79**(1): p. 014403.
69. Dovesi, R., V.R. Saunders, R. Roetti, R. Orlando, *et al.*, *CRYSTAL09* CRYSTAL09 User's Manual. University of Torino, Torino, 2009.
70. Dovesi, R., R. Orlando, B. Civalleri, R. Roetti, *et al.*, *Cystal09.* Z. Kristallogr, 2005. **220**(44): p. 571-574.
71. Towler, M.D., A. Zupan, and M. Causà, *Density functional theory in periodic systems using local Gaussian basis sets.* Computer Physics Communications, 1996. **98**(1–2): p. 181-205.
72. CRYSTAL09. Available from: http://www.crystal.unito.it/.

73. Pisani, C., *Quantum-Mechanical Ab-initio calculation of the Properties of Crystalline Materials*, in *Lecture Notes in Chemistry*. 1996: Spinger Verlag, Heidelberg, Germany.
74. Dovesi, R., B. Civalleri, R. Orlando, C. Roetti, *et al.*, *Ab Initio Quantum Simulation in Solid State Chemistry*. ChemInform, 2005. **36**(48): p. 1-121.
75. Lee, C., W. Yang, and R.G. Parr, *Development of the Colle-Salvetti correlation-energy formula into a functional of the electron density.* Physical Review B, 1988. **37**(2): p. 785.
76. Vosko, S.H., L. Wilk, and M. Nusair, *Accurate spin-dependent electron liquid correlation energies for local spin density calculations: a critical analysis.* Canadian Journal of Physics, 1980. **58**(8): p. 1200-1211.
77. Doll, K., R. Dovesi, and R. Orlando, *Analytical Hartree–Fock gradients with respect to the cell parameter: systems periodic in one and two dimensions.* Theoretical Chemistry Accounts: Theory, Computation, and Modeling (Theoretica Chimica Acta), 2006. **115**(5): p. 354-360.
78. Broyden, C.G., *The Convergence of a Class of Double-rank Minimization Algorithms 1. General Considerations.* IMA Journal of Applied Mathematics, 1970. **6**(1): p. 76-90.
79. Fletcher, R., *A new approach to variable metric algorithms.* The Computer Journal, 1970. **13**(3): p. 317-322.
80. Goldfarb, D., *A Family of Variable-Metric Methods Derived by Variational Means.* Mathematics of Computation, 1970. **24**(109): p. 23-26.
81. Shanno, D.F., *Conditioning of Quasi-Newton Methods for Function Minimization.* Mathematics of Computation, 1970. **24**(111): p. 647-656.
82. Ferrero, M., B. Civalleri, M. Rerat, R. Orlando, *et al.*, *The calculation of the static first and second susceptibilities of crystalline urea: A comparison of Hartree--Fock and density functional theory results obtained with the periodic coupled perturbed Hartree--Fock/Kohn--Sham scheme.* Journal of Chemical Physics, 2009. **131**(21): p. 214704-10.
83. Ferrero, M., M. Rerat, B. Kirtman, and R. Dovesi, *Calculation of first and second static hyperpolarizabilities of one- to three-dimensional periodic compounds. Implementation in the CRYSTAL code.* Journal of Chemical Physics, 2008. **129**(24): p. 244110-13.

84. Ferrero, M., M. Rerat, R. Orlando, and R. Dovesi, *Coupled perturbed Hartree-Fock for periodic systems: The role of symmetry and related computational aspects.* Journal of Chemical Physics, 2008. **128**(1): p. 014110-7.

85. Ferrero, M., M. Rérat, R. Orlando, and R. Dovesi, *The calculation of static polarizabilities of 1-3D periodic compounds. the implementation in the crystal code.* Journal Of Computational Chemistry, 2008. **29**(9): p. 1450-1459.

86. Resta, R., *Macroscopic polarization in crystalline dielectrics: the geometric phase approach.* Reviews of Modern Physics, 1994. **66**(3): p. 899-915.

87. King-Smith, R.D. and D. Vanderbilt, *Theory of polarization of crystalline solids.* Physical Review B, 1993. **47**(3): p. 1651-1654.

88. Berry, M.V., *Quantal Phase Factors Accompanying Adiabatic Changes.* Proceedings of the Royal Society of London. A. Mathematical and Physical Sciences, 1984. **392**(1802): p. 45-57.

89. Monkhorst, H.J. and J.D. Pack, *Special points for Brillouin-zone integrations.* Physical Review B, 1976. **13**(12): p. 5188-5192.

90. Kokalj, A., *XCrySDen—a new program for displaying crystalline structures and electron densities.* Journal of Molecular Graphics and Modelling, 1999. **17**(3–4): p. 176-179.

91. Momma, K. and F. Izumi, *VESTA: a three-dimensional visualization system for electronic and structural analysis.* Journal of Applied Crystallography, 2008. **41**(3): p. 653-658.

92. Inkscape. Available from: http://inkscape.org/

93. Gnuplot. Available from: http://www.gnuplot.info/.

94. Hashimoto, K., H. Irie, and A. Fujishima, *TiO_2 Photocatalysis:A Historical Overview and Future Prospects,*2005. **44**(12): p.8469-8485.

95. Zhang, H., G. Chen, and D.W. Bahnemann, *Photoelectrocatalytic materials for environmental applications.* Journal of Materials Chemistry, 2009. **19**(29): p. 5089-5121.

96. Sivula, K., R. Zboril, F. Le Formal, R. Robert, *et al.*, *Photoelectrochemical Water Splitting with Mesoporous Hematite Prepared by a Solution-Based*

Colloidal Approach. Journal of the American Chemical Society, 2010. **132**(21): p. 7436-7444.

97. Murphy, A.B., P.R.F. Barnes, L.K. Randeniya, I.C. Plumb, *et al.*, *Efficiency of solar water splitting using semiconductor electrodes.* International Journal of Hydrogen Energy, 2006. **31**(14): p. 1999-2017.

98. Ingler, W.B. and S.U.M. Khan, *A Self-Driven p/n-*Fe_2O_3 *Tandem Photoelectrochemical Cell for Water Splitting.* Electrochemical and Solid-State Letters, 2006. **9**(4): p. G144.

99. Brillet, J., M. Cornuz, F.L. Formal, J.-H. Yum, *et al.*, *Examining architectures of photoanode–photovoltaic tandem cells for solar water splitting.* Journal of Materials Research, 2011. **25**(01): p. 17-24.

100. Velev, J., A. Bandyopadhyay, W.H. Butler, and S. Sarker, *Electronic and magnetic structure of transition-metal-doped alpha -hematite.* Physical Review B, 2005. **71**(20): p. 205208.

101. Thimsen, E., S. Biswas, C.S. Lo, and P. Biswas, *Predicting the Band Structure of Mixed Transition Metal Oxides: Theory and Experiment.* The Journal of Physical Chemistry C, 2009. **113**(5): p. 2014-2021.

102. Kleiman-Shwarsctein, A., M.N. Huda, A. Walsh, Y. Yan, *et al.*, *Electrodeposited Aluminum-Doped* α-Fe_2O_3 *Photoelectrodes: Experiment and Theory*. Chemistry of Materials, 2009. **22**(2): p. 510-517.

103. Hahn, N.T. and C.B. Mullins, *Photoelectrochemical Performance of Nanostructured Ti- and Sn-Doped* α-Fe_2O_3 *Photoanodes.* Chemistry of Materials, 2010. **22**(23): p. 6474-6482.

104. Zhang, Y.J., Y.C. Wang, W. Yan, T. Li, *et al.*, *Synthesis of* Cr_2O_3*/TNTs nanocomposite and its photocatalytic hydrogen generation under visible light irradiation.* Applied Surface Science, 2009. **255**(23): p. 9508-9511.

105. Chandler, D., Z. Majumdar, G. Heiss, and R. Clegg, *Ruby Crystal for Demonstrating Time- and Frequency-Domain Methods of Fluorescence Lifetime Measurements.* Journal of Fluorescence, 2006. **16**(6): p. 793-807.

106. Wilson, N.C. and S.P. Russo, *Hybrid density functional theory study of the high-pressure polymorphs of alpha -*Fe_2O_3 *hematite.* Physical Review B, 2009. **79**(9): p. 094113.

107. Catti, M., G. Valerio, and R. Dovesi, *Theoretical study of electronic, magnetic, and structural properties of alpha -*Fe_2O_3 *(hematite).* Physical Review B, 1995. **51**(12): p. 7441.

108. Rollmann, G., A. Rohrbach, P. Entel, and J. Hafner, *First-principles calculation of the structure and magnetic phases of hematite.* Physical Review B, 2004. **69**(16): p. 165107.

109. Finger, L.W. and R.M. Hazen, *Crystal structure and isothermal compression of* Fe_2O_3, Cr_2O_3, *and* V_2O_3 *to 50 kbars.* Journal Of Applied Physics, 1980. **51**(10): p. 5362-5367.

110. Catti, M. and G. Sandrone, *Ab initio study of corundum-like* Me_2O_3*oxides (Me=Ti, V, Cr, Fe, Co, Ni).* Faraday Discussions, 1997. **106**: p. 189-203.

111. Shi, S., A.L. Wysocki, and K.D. Belashchenko, *Magnetism of chromia from first-principles calculations.* Physical Review B, 2009. **79**(10): p. 104404.

112. Causa, M., R. Dovesi, C. Roetti, and V.R. Saunders, *A Periodic Abinitio Hartree-Fock Calculation on Corundum.* Chemical Physics Letters, 1987. **140**(2): p. 120-123.

113. Dräger, G., and J.A. Leiro, *Electronic structure of alpha -*Al_2O_3 *studied by polarized x-ray-emission spectroscopy.* Physical Review B, 1990. **41**(18): p. 12919.

114. Liu, X.-L, W-H, Duan, and B-L, Gu, *Electronic Structure of High-Pressure Alumina Polymorphs.* Chinese Physics Letters, 2000. **17**(6): p. 441.

115. D'Amour, H., D. Schiferl, W. Denner, H. Schulz, *et al.*, *High-pressure single-crystal structure determinations for ruby up to 90 kbar using an automatic diffractometer.* Journal Of Applied Physics, 1978. **49**(8): p. 4411-4416.

116. Montanari, B., B. Civalleri, C.M. Zicovich-Wilson, and R. Dovesi, *Influence of the exchange-correlation functional in all-electron calculations of the vibrational frequencies of corundum* (α-Al_2O_3)*.* International Journal Of Quantum Chemistry, 2006. **106**(7): p. 1703-1714.

117. French, R.H., *Electronic Band Structure of Al2O3, with Comparison to Alon and AIN.* Journal of the American Ceramic Society, 1990. **73**(3): p. 477-489.

118. Benny, S., R. Grau-Crespo, and N.H. de Leeuw, *A theoretical investigation of α-Fe_2O_3-Cr_2O_3 solid solutions.* Physical Chemistry Chemical Physics, 2009. **11**(5): p. 808-815.

119. Moore, E.A., *First-principles study of the mixed oxide alpha -FeCr O3.* Physical Review B, 2007. **76**(19): p. 195107.

120. Busca, G., G. Ramis, M.d.C. Prieto, and V.S. Escribano, *Preparation and characterization of $Fe_{2-x}Cr_xO_3$ mixed oxide powders.* Journal of Materials Chemistry, 1993. **3**(6): p. 665-673.

121. Lei, Y., N.W. Cant, and D.L. Trimm, *Activity Patterns for the ''Water Gas Shift Reaction Over Supported Precious Metal Catalysts''.* Catalysis Letters, 2005. **103**(1): p. 133-136.

122. Aouissi, A., Z.A. Al-Othman, and H. Bayahia, *Ethyl benzene dehydrogenation in the presence of Carbon dioxide over Fe_2O_3-Cr_2O_3.* Asian Journal of Chemistry, 2010. **22**(6): p. 4873-4879.

123. Kung, H.H. and M.C. Kung, *Selective Oxidative Dehydrogenation of Butenes on Ferrite Catalysts*, in *Advances in Catalysis*, H.P. D.D. Eley and B.W. Paul, Editors. 1985, Academic Press. p. 159-198.

124. Bhushan, B., S. Mukherjee, A. Basumallick, S.K. Bandopadhyay, *et al.*, *Low temperature route to the multiferroic $FeAlO_3$: XRD and Mössbauer characterizations*, in *ICAME 2007*, N.S. Gajbhiye and S.K. Date, Editors. 2009, Springer Berlin Heidelberg. p. 1187-1193.

125. Bhushan, B., S. Mukherjee, A. Basumallick, S. Bandopadhyay, *et al.*, *Low temperature route to the multiferroic $FeAlO_3$: XRD and Mössbauer characterizations.* Hyperfine Interactions, 2008. **187**(1): p. 101-107.

126. Krén, E., B. Molnàr, E. Svàb, and É. Zsoldos, *Neutron diffraction study of the (1-x)[α]Fe_2O_3---xAl_2O_3 system.* Solid State Communications, 1974. **15**(10): p. 1707-1710.

127. Nagai, T., D. Hamane, P.S. Devi, N. Miyajima, *et al.*, *A New Polymorph of $FeAlO_3$ at High Pressure.* The Journal of Physical Chemistry B, 2005. **109**(39): p. 18226-18229.

128. Niihara, K., *New design concept of structural ceramics. Ceramic nanocomposites.* Nippon Seramikkusu Kyokai Gakujutsu Ronbunshi/Journal of the Ceramic Society of Japan, 1991. **99**(1154): p. 974-982.

129. Gallardo Amores, J.M., V. Sanchez Escribano, and G. Busca, *Characterisation of Fe-Cr-Al mixed oxides.* Materials Chemistry and Physics, 1999. **60**(2): p. 168-176.

130. Droubay, T., K.M. Rosso, S.M. Heald, D.E. McCready, *et al.*, *Structure, magnetism, and conductivity in epitaxial Ti -doped alpha - Fe_2 O_3 hematite: Experiment and density functional theory calculations.* Physical Review B, 2007. **75**(10): p. 104412.

131. Muscat, J., A. Wander, and N.M. Harrison, *On the prediction of band gaps from hybrid functional theory.* Chemical Physics Letters, 2001. **342**(3-4): p. 397-401.

132. Catti, M., G. Valerio, R. Dovesi, and M. Causà, *Quantum-mechanical calculation of the solid-state equilibrium MgO+ aAl_2O_3=$MgAl_2O_4$ (spinel) versus pressure.* Physical Review B, 1994. **49**(20): p. 14179.

133. Fotiev, A.A., L.L. Surat, G.A. Korablev, and A.I. Tret'yako, *Relations De Phases Dans Le SystemeV_2O_5-Fe_2O_3-Al_2O_3-Cr_2O_3.*Zhurnal Neorganicheskoi Khimii, 1981. **26**(1): p. 242-248.

134. Ma, Y., P.D. Johnson, N. Wassdahl, J. Guo, *et al.*, *Electronic structures of alpha -Fe_2O_3 and Fe_3O_4 from O K-edge absorption and emission spectroscopy.* Physical Review B, 1993. **48**(4): p. 2109.

135. Crawford, J.A. and R.W. Vest, *Electrical conductivity of single-crystal Cr_2O_3.* Journal Of Applied Physics, 1964. **35**(8): p. 2413-2418.

136. Bosman, A.J. and H.J. van Daal, *Small-polaron versus band conduction in some transition-metal oxides.* Advances in Physics, 1970. **19**(77): p. 1-117.

137. Liao, P., M.C. Toroker, and E.A. Carter, *Electron Transport in Pure and Doped Hematite.* Nano Letters, 2011. **11**(4): p. 1775-1781.

138. Maedal, K., K. Suzuki, Y. Yamashita, and Y. Mera, *Dislocation motion in semiconducting crystals under the influence of electronic perturbations.* Journal of Physics: Condensed Matter, 2000. **12**(49): p. 10079.

139. Dunmur, D.A., K. Szumilin, and T.F. Waterworth, *Field-Induced Biaxiality in Nematics.* Molecular Crystals and Liquid Crystals Incorporating Nonlinear Optics, 1987. **149**: p. 385 - 392.

140. Dunmur, D.A., T.F. Waterworth, and P. Palffy-Muhoray, *Electric Field Induced Birefringence in Nematic Liquid Crystal Films: Evidence for Wall*

Quenching of Director Fluctuations. Molecular Crystals And Liquid Crystals, 1985. **124**: p. 73 - 88.

141. Lee, A., *Effect of an external electric field on liquid crystalline polymers.* Physics Letters A, 1986. **113**(7): p. 391-394.
142. Binek, C., A. Hochstrat, X. Chen, P. Borisov, *et al.*, *Electrically controlled exchange bias for spintronic applications.* Journal Of Applied Physics, 2005. **97**(10): p. 10C514-3.
143. Borisov, P., A. Hochstrat, V.V. Shvartsman, W. Kleemann, *et al.*, *Magnetoelectric* Cr_2O_3 *for spintronic applications.* Integrated Ferroelectrics: An International Journal, 2008. **99**(1): p. 69-76.
144. Žutić, I., J. Fabian, and S. Das Sarma, *Spintronics: Fundamentals and applications.* Reviews Of Modern Physics, 2004. **76**(2): p. 323.
145. Harb, M., P. Labeguerie, I. Baraille, and M. Rerat, *Response of low quartz* SiO_2 *to the presence of an external static electric field: A density functional theory study.* Physical Review B, 2009. **80**(23): p. 235131.
146. Tomaszewska, A. and Z.M. Stepień, *The influenced of the external electric field on the hydrogen-palladium system.* Journal of Physics: Conference Series, 2007. **79**(1): p. 012028.
147. Zhou, J., Q. Wang, Q. Sun, P. Jena, *et al.*, *Electric field enhanced hydrogen storage on polarizable materials substrates.* Proceedings of the National Academy of Sciences, 2010. **107**(7): p. 2801-2806.
148. Kudo, A. and Y. Miseki, *Heterogeneous photocatalyst materials for water splitting.* Chemical Society Reviews, 2009. **38**(1): p. 253-278.
149. Martin, R.L. and F. Illas, *Antiferromagnetic Exchange Interactions from Hybrid Density Functional Theory.* Physical Review Letters, 1997. **79**(8): p. 1539.
150. www.crystal.unito.it/basis_sets/ptable.html.
151. Apra, E., M. Causa, M. Prencipe, R. Dovesi, *et al.*, *On the Structural-Properties of Nacl - an Abinitio Study of the B1-B2 Phase-Transition.* Journal Of Physics-Condensed Matter, 1993. **5**(18): p. 2969-2976.
152. Dovesi, R., C. Roetti, C. Freyriafava, M. Prencipe, *et al.*, *On the Elastic Properties of Lithium, Sodium and Potassium Oxide - an Abinitio Study.* Chemical Physics, 1991. **156**(1): p. 11-19.

153. Mérawa, M., P. Labeguerie, P. Ugliengo, K. Doll, *et al.*, *The structural, electronic and vibrational properties of LiOH and NaOH: an ab initio study.* Chemical Physics Letters, 2004. **387**(4-6): p. 453-459.

154. Nada, R., C.R.A. Catlow, C. Pisani, and R. Orlando., *An ab-initio Hartree-Fock perturbed-cluster study of neutral defects in LiF.* Modelling And Simulation In Materials Science And Engineering, 1993. **1**(2): p. 165.

155. Rathor, A., G. Arora, and B.L. Ahuja, *Band-structure calculations and electron momentum densities of AgCl and AgBr.* physica status solidi (b), 2008. **245**(8): p. 1563-1570.

156. Monkhorst, H.J. and J.D. Pack, *Special points for Brillouin-zone integrations.* Physical Review B, 1976. **13**(12): p. 5188.

157. Lacivita, V., M. Rerat, B. Kirtman, M. Ferrero, *et al.*, *Calculation of the dielectric constant epsilon and first nonlinear susceptibility chi((2)) of crystalline potassium dihydrogen phosphate by the coupled perturbed Hartree-Fock and coupled perturbed Kohn-Sham schemes as implemented in the CRYSTAL code.* Journal Of Chemical Physics, 2009. **131**(20): p. 204509.

158. Springborg, M. and B. Kirtman, *The response of extended systems to electrostatic fields(1).* Canadian Journal Of Chemistry-Revue Canadienne De Chimie, 2009. **87**(7): p. 984-993.

159. Orlando, R., V. Lacivita, R. Bast, and K. Ruud, *Calculation of the first static hyperpolarizability tensor of three-dimensional periodic compounds with a local basis set: A comparison of LDA, PBE, PBE0, B3LYP, and HF results.* Journal of Chemical Physics, 2010. **132**(24): p. 244106-9.

160. Pascale, F., C.M. Zicovich-Wilson, F.L. Gejo, B. Civalleri, *et al.*, *The calculation of the vibrational frequencies of crystalline compounds and its implementation in the CRYSTAL code.* Journal Of Computational Chemistry, 2004. **25**(6): p. 888-897.

161. Noel, Y., R. Demichelis, F. Pascale, P. Ugliengo, *et al.*, *Ab initio quantum mechanical study of gamma-AlOOH boehmite: structure and vibrational spectrum.* Physics And Chemistry Of Minerals, 2009. **36**(1): p. 47-59.

162. Valenzano, L., F. Pascale, M. Ferrero, and R. Dovesi, *Ab Initio Quantum-Mechanical Prediction of the IR and Raman Spectra of* $Ca_3Cr_2Si_3O_{12}$

Uvarovite Garnet. International Journal Of Quantum Chemistry, 2010. **110**(2): p. 416-421.

163. Darrigan, C., M. Rérat, G. Mallia, and R. Dovesi, *Implementation of the finite field perturbation method in the CRYSTAL program for calculating the dielectric constant of periodic systems.* Journal Of Computational Chemistry, 2003. **24**(11): p. 1305-1312.
164. Callen, H.B., *Electric Breakdown in Ionic Crystals.* Physical Review, 1949. **76**(9): p. 1394.
165. Sideshmukh, P.B., L. Siderhmukh, and K.G. Subhadra, Alkali Halides A Handbook of Physical Properties, Springer Series in Materials Science 2001.
166. Sandrone, G. and D.A. Dixon, *A periodic density functional theory and Hartree-Fock study of alkali halides with Gaussian orbitals.* Journal Of Physical Chemistry A, 1998. **102**(50): p. 10310-10317.
167. Prencipe, M., A. Zupan, R. Dovesi, E. Apra, *et al.*, *Ab-Initio Study of the Structural-Properties of Lif, Naf, Kf, Licl, Nacl, and Kcl.* Physical Review B, 1995. **51**(6): p. 3391-3396.
168. Mei, W.N., L.L. Boyer, M.J. Mehl, M.M. Ossowski, *et al.*, *Calculation of electronic, structural, and vibrational properties in alkali halides using a density-functional method with localized densities.* Physical Review B, 2000. **61**(17): p. 11425.
169. Page, L.J. and E.H. Hygh, *Calculation of Energy Bands in Alkali Halides.* Physical Review B, 1970. **1**(8): p. 3472-&.
170. Ching, W.Y., F. Gan, and M.-Z. Huang, *Band theory of linear and nonlinear susceptibilities of some binary ionic insulators.* Physical Review B, 1995. **52**(3): p. 1596.
171. Kunz, A.B., *Study of the electronic structure of twelve alkali halide crystals.* Physical Review B, 1982. **26**(4): p. 2056.
172. Born, M. and K. Huang, Dynamical Theory of Crystal Lattices. 2007:Clarendon, UK.
173. Von Hippel, A., *Electric Breakdown of Solid and Liquid Insulators.* Journal Of Applied Physics, 1937. **8**(12): p. 815-832.

174. Zener, C., *A Theory of the Electrical Breakdown of Solid Dielectrics.* Proceedings of the Royal Society of London. Series A, 1934. **145**(855): p. 523-529.
175. Kao, K.C., *Dielectric Phenomena in Solids.* first ed., Elsevier Academic Press, San Diego, London, 2004.
176. Von Hippel, A. and R.S. Alger, *Breakdown of Ionic Crystals by Electron Avalanches.* Physical Review, 1949. **76**(1): p. 127.
177. Von Hippel, A., Z. Physics , 1932. **75**: p. 145-170.
178. Greenwood, N.N. and A. Earnshaw, *Chemistry of the elements*. Second ed., Pergamon Press, Oxford, UK, 1984.
179. Tani, T., *Modified Electron Transfer Mechanism for Spectral Sensitization in Photography .3. Spectral Sensitization of Print-out Photodecomposition of Silver Halides.* Photographic Science and Engineering, 1970. **14**(1): p. 63.
180. Kakuta, N., N. Goto, H. Ohkita, and T. Mizushima, *Silver Bromide as a Photocatalyst for Hydrogen Generation from CH3OH/H_2O Solution.* The Journal of Physical Chemistry B, 1999. **103**(29): p. 5917-5919.
181. Huo, P., Y. Yan, S. Li, H. Li, *et al.*, *Floating photocatalysts of fly-ash cenospheres supported AgCl/TiO_2 films with enhanced Rhodamine B photodecomposition activity.* Desalination, 2010. **256**(1–3): p. 196-200.
182. Glaus, S. and G. Calzaferri, *Silver Chloride Clusters and Surface States.* The Journal of Physical Chemistry B, 1999. **103**(27): p. 5622-5630.
183. Dahne, S., *Spectral Sensitization of Silver-Halides - the Last 20 Years.* Journal of Photographic Science, 1990. **38**(3): p. 66-69.
184. Kanzaki, H., *Recent Developments in the Physics of Silver-Halides.* Photographic Science and Engineering, 1980. **24**(5): p. 219-226.
185. Kim, J.M., B.S. Choi, S. Kim, II, J.M. Kim, *et al.*, *Holographic Optical Elements Recorded in Silver Halide Sensitized Gelatin Emulsions. Part I. Transmission Holographic Optical Elements.* Applied Optics, 2001. **40**(5): p. 622-632.
186. Aprà, E., E. Stefanovich, R. Dovesi, and C. Roetti, *An ab initio Hartree--Fock study of silver chloride.* Chemical Physics Letters, 1991. **186**(4-5): p. 329-335.

187. Gu, S., B. Li, C. Zhao, Y. Xu, *et al.*, *Preparation and characterization of visible light-driven AgCl/PPy photocatalyst.* Journal of Alloys and Compounds, 2011. **509**(18): p. 5677-5682.

188. Li, Y. and Y. Ding, *Porous AgCl/Ag Nanocomposites with Enhanced Visible Light Photocatalytic Properties.* The Journal of Physical Chemistry C, 2010. **114**(7): p. 3175-3179.

189. Zhu, M., P. Chen, and M. Liu, *Graphene Oxide Enwrapped Ag/AgX (X = Br, Cl) Nanocomposite as a Highly Efficient Visible-Light Plasmonic Photocatalyst.* Acs Nano, 2011. **5**(6): p. 4529-4536.

190. Enderby, J.E. and A.C. Barnes, *Liquid semiconductors.* Reports on Progress in Physics, 1990. **53**(2): p. 85.

191. Tejeda, J., W. Braun, A. Goldmann, and M. Cardona, *Valence Bands of Silver-Halides Determined by X-Ray and Uv Photoemission.* Journal of Electron Spectroscopy and Related Phenomena, 1974. **5**(Nov-D): p. 583-592.

192. Mason, M.G., *Photoelectron spectroscopy studies of the band structures of silver halides.* Physical Review B, 1975. **11**(12): p. 5094.

193. Victora, R.H., *Calculated electronic structure of silver halide crystals.* Physical Review B, 1997. **56**(8): p. 4417.

194. Benmessabih, T., B. Amrani, F.E.H. Hassan, F. Hamdache, *et al.*, *Computational study of AgCl and AgBr semiconductors.* Physica B-Condensed Matter, 2007. **392**(1-2): p. 309-317.

195. Kunz, A.B., *Electronic structure of AgF, AgCl, and AgBr.* Physical Review B, 1982. **26**(4): p. 2070.

196. Ballaro, S., A. Balzarotti, and V. Grasso, *Electric field effects on indirect optical transitions in AgCl.* Journal of Physics C: Solid State Physics, 1970. **3**(10): p. 2200.

197. Praveen, C.S., A. Kokalj, and M. Valant, *B3LYP investigation of response properties of alkali halides on external static electric fields.* Computational Materials Science, 2011. **50**(9): p. 2628-2635.

198. Paier, J., M. Marsman, and G. Kresse, *Why does the B3LYP hybrid functional fail for metals?* The Journal of Chemical Physics, 2007. **127**(2): p. 024103-10.

199. Hull, S. and D.A. Keen, *Pressure-induced phase transitions in AgCl, AgBr, and AgI.* Physical Review B, 1999. **59**(2): p. 750.

200. Vogel, D., P. Krüger, and J. Pollmann, *Ab initio electronic structure of silver halides calculated with self-interaction and relaxation-corrected pseudopotentials.* Physical Review B, 1998. **58**(7): p. 3865.

201. Nunes, G.S., P.B. Allen, and J.L. Martins, *Pressure-induced phase transitions in silver halides.* Physical Review B, 1998. **57**(9): p. 5098.

202. Li, Y., L. Zhang, T. Cui, Y. Ma, *et al.*, *Phonon instabilities in rocksalt AgCl and AgBr under pressure studied within density functional theory.* Physical Review B, 2006. **74**(5): p. 054102.

203. Gava, P., A. Kokalj, S. de Gironcoli, and S. Baroni, *Adsorption of chlorine on Ag(111): No subsurface Cl at low coverage.* Physical Review B, 2008. **78**(16): p. 165419.

204. Lawaetz, P., *Stability of the Wurtzite Structure.* Physical Review B, 1972. **5**(10): p. 4039.

205. de Boer, P.K. and R.A. de Groot, *Conduction Band of the Photographic Compound AgCl.* The Journal of Physical Chemistry A, 1999. **103**(26): p. 5113-5115.

206. Hellwege, K.H. and O. Madelung, eds. *Semiconductor Physics of II-VI and I-VII Compounds. Semimagnetic Semiconductors*. New York Series Group III, ed. Landolt-Bornstein. 1987: Springer, Berlin, Germany.

207. Glaus, S. and G. Calzaferri, *The band structures of the silver halides AgF, AgCl, and AgBr: A comparative study.* Photochemical & Photobiological Sciences, 2003. **2**(4): p. 398-401.

208. Ayma, D., J.P. Campillo, M. Rérat, and M. Causà, *Ab initio calculation of dynamic polarizability and dielectric constant of carbon and silicon cubic crystals.* Journal Of Computational Chemistry, 1997. **18**(10): p. 1253-1263.

209. Brothers, A.D. and D.W. Lynch, *Optical Properties of AgCl, AgBr, TlCl, and TlBr under Hydrostatic Pressure.* Physical Review, 1969. **180**(3): p. 911-918.

210. Suita, T. and N. Itoh, *Dielectric Breakdown and Pulse Conduction of Silver Halide Crystals.* Journal of the Physical Society of Japan, 1956. **11**(5): p. 474.

211. Seabold, J.A. and K.S. Choi, *Efficient and stable photo-oxidation of water by a bismuth vanadate photoanode coupled with an iron oxyhydroxide oxygen evolution catalyst.* Jornal of American Chemical Society, 2012. **134**(4): p. 2186-92.

212. Kudo, A. and Y. Miseki, *Heterogeneous photocatalyst materials for water splitting.* Chemical Society Reviews, 2009. **38**(1).

213. Kudo, A., *Photocatalysis and solar hydrogen production.* Pure and Applied Chemistry, 2007. **79**(11): p. 1917-1927.

214. Domen, K., S. Naito, M. Soma, T. Onishi, *et al.*, *Photocatalytic decomposition of water vapour on an NiO-*$SrTiO_3$ *catalyst.* Journal of the Chemical Society, Chemical Communications, 1980(12): p. 543-544.

215. Kato, H. and A. Kudo, *New tantalate photocatalysts for water decomposition into H2 and O2.* Chemical Physics Letters, 1998. **295**(5–6): p. 487-492.

216. Kato, H., H. Kobayashi, and A. Kudo, *Role of Ag+ in the Band Structures and Photocatalytic Properties of* $AgMO_3$ *(M: Ta and Nb) with the Perovskite Structure*. The Journal of Physical Chemistry B, 2002. **106**(48): p. 12441-12447.

217. Li, C., H. Wang, B. Wang, and R. Wang, *First-principles study of the structure, electronic, and optical properties of orthorhombic BiInO[sub 3]*. Applied Physics Letters, 2007. **91**(7): p. 071902-3.

218. Li, C., B. Wang, R. Wang, H. Wang, *et al.*, *First-principles study of structural, elastic, electronic, and optical properties of orthorhombic* $BiGaO_3$. Computational Materials Science, 2008. **42**(4): p. 614-618.

219. McLeod, J.A., Z.V. Pchelkina, L.D. Finkelstein, E.Z. Kurmaev, *et al.*, *Electronic structure of* $BiMO_3$ *multiferroics and related oxides.* Physical Review B, 2010. **81**(14): p. 144103.

220. Lee, J.H., X. Ke, R. Misra, J.F. Ihlefeld, *et al.*, *Adsorption-controlled growth of* $BiMnO_3$ *films by molecular-beam epitaxy.* Applied Physics Letters, 2010. **96**(26): p. 262905-3.

221. Takahashi, K., N. Kida, and M. Tonouchi, *Terahertz Radiation by an Ultrafast Spontaneous Polarization Modulation of Multiferroic* $BiFeO_3$ *Thin Films.* Physical Review Letters, 2006. **96**(11): p. 117402.

222. Ravindran, P., R. Vidya, A. Kjekshus, H. Fjellvåg, *et al.*, *Theoretical investigation of magnetoelectric behavior in* $BiFeO_3$. Physical Review B, 2006. **74**(22): p. 224412.

223. Baettig, P., C. Ederer, and N. Spaldin, *First principles study of the multiferroics* $BiFeO_3$*,* Bi_2FeCrO_6*, and* $BiCrO_3$*: Structure, polarization, and magnetic ordering temperature.* Physical Review B, 2005. **72**(21).

224. Khomskii, D., *Classifying multiferroics: Mechanisms and effects.* Physics, 2009. **2**: p. 20.

225. Ederer, C. and N.A. Spaldin, *Effect of Epitaxial Strain on the Spontaneous Polarization of Thin Film Ferroelectrics.* Physical Review Letters, 2005. **95**(25): p. 257601.

226. Khomskii, D.I., *Multiferroics: Different ways to combine magnetism and ferroelectricity.* Journal of Magnetism and Magnetic Materials, 2006. **306**(1): p. 1-8.

227. Hill, N.A., *Why Are There so Few Magnetic Ferroelectrics?* The Journal of Physical Chemistry B, 2000. **104**(29): p. 6694-6709.

228. Picozzi, S. and C. Ederer, *First principles studies of multiferroic materials.* Journal of Physics: Condensed Matter, 2009. **21**(30): p. 303201.

229. Bi, L., A.R. Taussig, H.-S. Kim, L. Wang, *et al.*, *Structural, magnetic, and optical properties of* $BiFeO_3$ *and* Bi_2FeMnO_6 *epitaxial thin films: An experimental and first-principles study.* Physical Review B, 2008. **78**(10): p. 104106.

230. Belik, A.A., *Polar and nonpolar phases of BiMO3: A review.* Journal of Solid State Chemistry, 2012. *In Press.*

231. Wei, W., Y. Dai, and B. Huang, *First-Principles Characterization of Bi-based Photocatalysts:* $Bi_{12}TiO_{20}$*,* $Bi_2Ti_2O_7$*, and* Bi_4Ti3O_{12}*.* The Journal of Physical Chemistry C, 2009. **113**(14): p. 5658-5663.

232. Goffinet, M., P. Hermet, D. Bilc, and P. Ghosez, *Hybrid functional study of prototypical multiferroic bismuth ferrite.* Physical Review B, 2009. **79**(1).

233. Spaldin, N.A. and M. Fiebig, *Materials science. The renaissance of magnetoelectric multiferroics.* Science, 2005. **309**(5733): p. 391-2.

234. Shannon, R., *Revised effective ionic radii and systematic studies of interatomic distances in halides and chalcogenides.* Acta Crystallographica Section A, 1976. **32**(5): p. 751-767.

235. Lufaso, M.W. and P.M. Woodward, *Prediction of the crystal structures of perovskites using the software program SPuDS.* Acta Crystallographica Section B, 2001. **57**(6): p. 725-738.

236. Brown, I.D., *The chemical bond in inorganic chemistry: the bond valence model*, 2006: Oxford University Press, UK.

237. Stroppa, A. and S. Picozzi, *Hybrid functional study of proper and improper multiferroics.* Physical Chemistry Chemical Physics, 2010. **12**(20): p. 5405-5416.

238. De La Pierre, M., R. Orlando, L. Maschio, K. Doll, *et al.*, *Performance of six functionals (LDA, PBE, PBESOL, B3LYP, PBE0, and WC1LYP) in the simulation of vibrational and dielectric properties of crystalline compounds. The case of forsterite Mg_2SiO_4.* Journal Of Computational Chemistry, 2011. **32**(9): p. 1775-1784.

239. Vasylechko, L., A. Matkovskii, D. Savytskii, A. Suchocki, *et al.*, *Crystal structure of $GdFeO_3$-type rare earth gallates and aluminates.* Journal of Alloys and Compounds, 1999. **291**(1–2): p. 57-65.

240. Kim, H.G., D.W. Hwang, and J.S. Lee, *An Undoped, Single-Phase Oxide Photocatalyst Working under Visible Light.* Journal of American Chemical Society, 2004. **126**(29): p. 8912-8913.

241. Ferrero, M., M. Rérat, R. Orlando, R. Dovesi, *et al.*, *Coupled perturbed Kohn-Sham calculation of static polarizabilities of periodic compounds.* Journal of Physics: Conference Series, 2008. **117**(1): p. 012016.